Oscillating Dispersed-Phase Co-Flow Microfluidic Droplet Generation:
Effects on Jet Length and Droplet Size

Amin Shams Khorrami

A THESIS SUBMITTED TO

THE FACULTY OF GRADUATE STUDIES

IN PARTIAL FULFILLMENT OF THE REQUIREMENTS

FOR THE DEGREE OF

MASTER OF APPLIED SCIENCE

Graduate Program in

MECHANICAL ENGINEERING

York University

Toronto, Ontario

January 2018

Abstract

Droplet-based microfluidics have emerged as versatile platforms offering unique advantages with a wide span of applications in biology and chemistry. Modern applications demand size-optimized (dispersed- or d-phase) droplets with various dimensions for encapsulation of various analytes and reagents within a (continuous- or c-phase) fluid. Although there is adequate control on size and monodispersity, most conventional microfluidic techniques cannot generate more than one droplet size at a time in a continuous and high-throughput manner. Moreover, the widely used co-flow microfluidic droplet generation technique (with co-axial c- and d-phase flows) is bottlenecked with droplet polydispersity at high throughputs due to the transition from a more-stable dripping regime to an instable jetting regime at high d-phase flow rates.

There is a demand for generation of multi-size monodispersed droplets in co-flow devices. Taking advantage of the parabolic velocity profile of the c-phase flow inside a channel, an axial drag force gradient can be generated by positioning the co-axial d-phase nozzle at different lateral locations in the channel. Upon oscillatory motion of the nozzle, an additional transverse drag can also be introduced onto the droplets. We hypothesized that the combined effects of axial and transverse drags can be used for overcoming the aforementioned limitations of co-flow systems.

In this study, we first validated the effect of various flow parameters on the size of generated droplets in a conventional co-flow device with a stationary d-phase nozzle. After establishing the bases for our study, we applied a 0-15 Hz oscillatory motion to the nozzle at different d- and c-phase flow rates to examine both the dripping and jetting regimes. We benefited from the superimposed effects of axial and traverse drag forces to produce multi-size monodisperse droplets

in the dripping regime. A wide range (4 nL up to 4 µL) of repeatable patterns of monodispersed droplets with different diameters were generated at different oscillation frequencies. Size of generated droplets were directly proportional to the d-phase flow rate (*Weber* or *We* number) and inversely proportional to the c-phase flow rate (*Capillary* or *Ca* number) and oscillation frequency. An increasing trend in the number of generated droplet sizes was also observed upon increasing the aforementioned parameters.

Finally, we studied the effect of oscillatory transverse drag force on suppressing the jetting phenomena in our device. Jet length was directly proportional to the d-phase flow rate (*We*) and inversely proportional to the oscillation frequency. Oscillation-induced jet length reduction was more significant at high *We* numbers, but a smaller slope in jet length reduction was always observed at oscillation frequencies higher than 10 Hz. As an important parameter in inertial effects, the effect of d-phase viscosity was also studied in the jetting regime. Increasing the viscosity of the d-phase resulted in diminishing the effect of oscillation on jet length reduction. We also did some preliminary experiments to evaluate the efficiency of our method in ultra-low interfacial tension systems (e.g. water-in-water). Primary results revealed that our technique can effectively disintegrate stable jets into repeatable patterns of multi-size droplets in these systems.

Our technique has been shown to generate repeatable patterns of droplets with different sizes and reduce the jet length at different breakup regimes. Further investigations are required at more *We-Ca* combinations and preferably other oscillation frequencies to acquire a complete map for droplet generation at desired size ranges. Jet length reduction effect also seems to be promising for applications where due to inherently low interfacial tension, the d-phase flow forms a long stable jet which can be broken up into droplets using the additional oscillatory drag in our device.

Acknowledgement

After an intensive period of two and half years, today is the day: writing this note of thanks is the finishing touch on my dissertation. It has been a constructive learning period for me, not only in the scientific field, but also on a personal level. Pursuing my studies as a master student and conducting independent research with having an opportunity to meet brilliant people in the field has had a big impact on me. I would like to reflect on the people who have supported and helped me so much throughout this period.

I would like to express my sincere acknowledgement to my supervisor Dr. Pouya Rezai for his patience, motivation, enthusiasm, and immense knowledge while supporting my graduate study and research. His guidance helped me in all period of research and writing of this thesis.

Last but not least, I must express my very profound gratitude to my parents, my sister and my dear friends for providing me with unfailing support and continuous encouragement throughout my years of study and through the process of researching and writing this thesis. This accomplishment would not have been possible without them.

Thank you.

Table of Contents

List of Tables

List of Figures

Chapter 1

INTRODUCTION AND RESEARCH OPPORTUNITY

1.1 Droplets and Their Applications

Droplets can be confronted in nature and a broad range of scientific and engineering applications. Natural droplets can be witnessed in rain shower, fog, rainbow, cloud and dew [1, 2]. Droplets generated with different sizes in various media have also found applications in many industrial fields such as spray, aerosol, power generation, automotive, metallurgy, powder generation, pharmaceutical, food processing, inkjet printing and emulsions [3]. Polymer-dispersed nematic droplets of liquid crystals also hold great potential in optic display industries [4, 5]. The dispersed form of liquid droplets with small dimensions and large quantity in gas (usually air), which is called spray, can be utilized to clean [6], coat [7] and cool down [8, 9] different surfaces. Phase-change spray cooling holds a significant potential in high-flux heat removal applications by taking the advantage of relatively enhanced heat transfer characteristics in two phase systems [10]. As shown in Figure 1-1, by spraying coolants on hot surfaces, small droplets touch the surface and cool it down by absorbing required latent heat for evaporation. Fuel droplet vaporization and spray combustion are extensively used in internal combustion engines and power generation applications [11, 12]. Achieving high combustion efficiencies requires maximized oxygen to fuel ratios which is attainable by increased surface-area-to-volume ratio of droplets [13, 14]. By introducing new and heavier fuels, spray and atomization techniques will find extensive applications in fuel combustion industry [15].
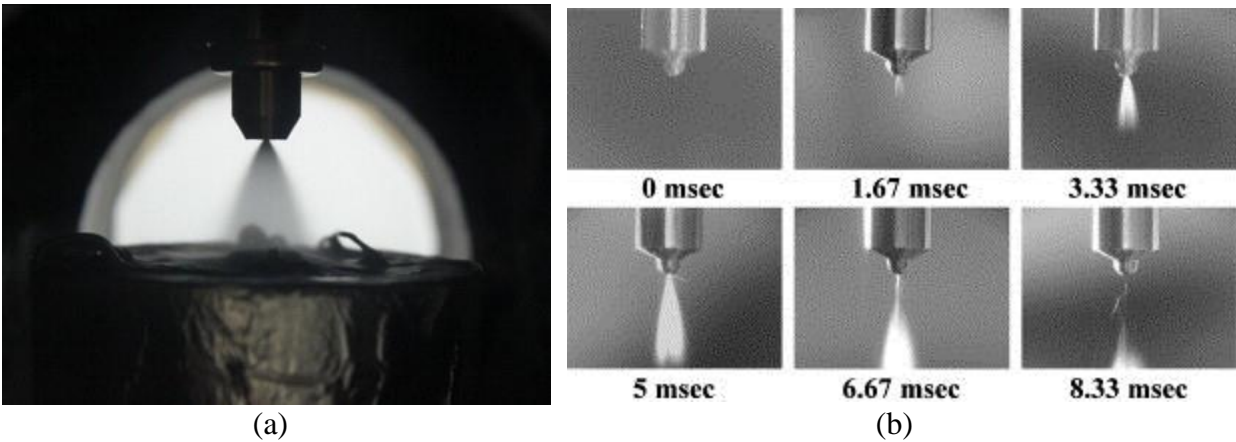
Figure 1-1. Application of droplets in (a) Spray cooling. Image reprinted by permission from ref. [16]*, Copyright 2013, Elsevier. (b) Consecutive optical images of the fuel sprays with one injection hole in nozzle at different time segments. Image reprinted by permission from ref.* [17]*, Copyright 2005, Elsevier.*

Alongside the industrial applications, droplets are also favorable in chemical and biological applications. Since 1965, by introducing artificial cells by T. M. S Chang [18], the encapsulation of biological targets has become a promising field of research for biomedical applications. Compartmentalization of biological samples with adsorbents, magnetic materials, drugs, cells, stem cells, enzymes, microorganisms, vaccines, genetically engineered cells, hormones, and many other materials inside microcapsules with various wall-properties finds a wide span of applications in different branches of biological research [19]. For example, Prakash and Chang [20] studied the *in-vivo* effects of genetically engineered *Escherichia coli DH5* bacteria encapsulated in a permeable artificial cell on urea and ammonia removal in case of kidney failure in rats.

The applications of discrete-volume compartments and droplets in biology and chemistry has advanced dramatically during the past few decades, but their review is beyond the scope of this thesis. However, various droplet fabrication methods that can be categorized into conventional and advanced (e.g. microfluidic-based) approaches are relevant to our work and reviewed in the following sections.

1.2 Conventional Droplet Generation Methods

Droplets can be created by (1) phase transition processes like condensation of vapors or solid particle/wire melting or (2) bulk fluid disintegration process which involves breakup of an interface between two immiscible fluid phases. Phase transition mechanisms require precise thermally-controllable systems to provide saturation conditions for droplet generation. For instance, homogeneous condensation of vapor requires highly supersaturated conditions, whereas inhomogeneous condensation occurs at lower supersaturation in the presence of very small particles serving as condensation nuclei. On the other hand, in bulk liquid disintegration processes two or more immiscible fluids are present and droplet formation is associated with an enormous increase in surface area. For instance, transforming one liter of bulk liquid into spherical droplets with diameter of 1 mm will produce $\sim 1.9 \times 10^6$ droplets leading to a drastic increase in the surface area ($\sim 100x$). Discharging an immiscible phase of fluid through a small nozzle into another fluid, like a shower head, can enhance phase disintegration [3]. Increase in surface area is inversely proportional to the diameter of generated droplets and therefore decreasing the droplet diameter leads to an increase in the total surface-area-to-volume-ratio. Downsizing the generated droplets and consequent increase in the surface area yields into unique characteristics, like enhanced affinity of cells and biomarkers encapsulated in the droplet, that are highly required in different fields of science and bioengineering [21].

Miniaturization of biological, chemical, medical and industrial systems have been proven to increase their efficiency and efficacy [12, 22–25]. The urge for miniaturization of systems have given birth to fabrication of macroscale tools such as pipettes, test tubes, and multi-well plates that can handle small discrete volumes of samples and reagents. Although handling small quantities of

liquids via macroscale devices seems to be simple, it becomes a labor intensive task while performing large scale assays [26]. For instance, pipetting hundreds of droplets with 5µL volume in biochemical assays can be a laborious process prone to operator fatigue and errors. Moreover, application-raised demand for handling even smaller quantities of reagents in the ranges of nano- to pico-liters with high precision limits the usage of macroscale devices. Advances in robotics has facilitated the fabrication of automatic arms that are capable of handling samples with desired pace and accuracy [27, 28]. However, excessive initial and maintenance costs, occupying large working spaces and immobility of the equipment are the main drawbacks of automated robotic arms in many point-of-care and point-of-need applications. Accordingly, the emergence of microfluidics technology that takes advantage of the advanced high-precision microfabrication techniques in microelectronics industry was a turn-over point in droplet miniaturization and subsequent applications.

1.3 Microfluidic Droplet Generation Methods

Microfluidics is the field of science and engineering that deals with small amounts of fluids in the range of micro- to femto-liters. It offers great capabilities to overcome the size and precision challenges in recent miniaturization applications such as the synthesis of micro- and nano-droplets. In microfluidic devices, operating fluids are processed inside channels at length scales ranging from few up to hundreds of micrometers [29]. Rapid and precise fabrication, small-scaled sample and reagent consumption rates, high resolution, low cost, short analysis times, high sensitivity and most importantly, capability of integrating different unit operations such as valving and pumping are the advantages that have attracted many researchers into the rapidly developing field of microfluidics technology.

Droplets have gained a great attention in microfluidics owing to their desirable characteristics. Micron-sized generated droplets retain high surface area to volume ratio, good encapsulation efficiency, facile manipulation, low contamination risk and low reagent consumption rate. Thus, same-size or monodispersed microdroplets generated at high throughputs via various microfluidic-based methods hold a great potential in a wide range of applications. Drug delivery vehicles for targeted transportation of compounds [30, 31], optical screening compartments for protein crystallization [32–34], nanoparticle synthesis [35, 36], and cultivation microenvironments for studying bacteria [37–39], cells [40, 41], and organisms [42, 43] are some of the current applications of droplet based microfluidics as shown in Figure 1-2.
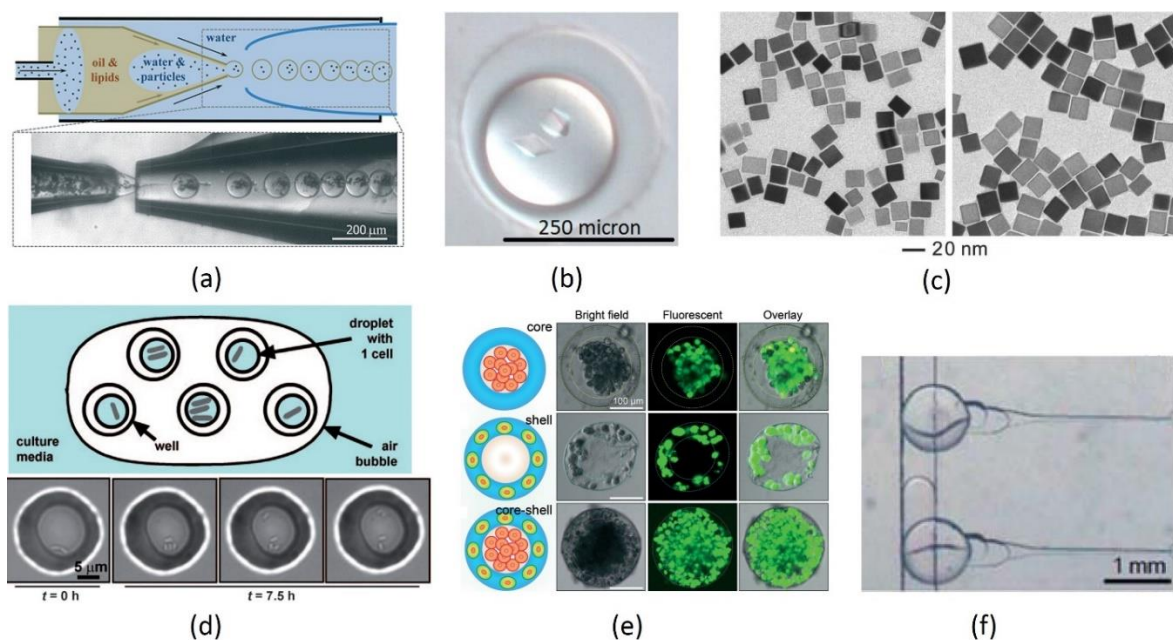
Figure 1-2. Different applications of droplet based microfluidics. (a) Analyte encapsulation and drug screening. Image reprinted by permission from ref. [31], Copyright 2014, Royal Society of Chemistry (RSC). (b) Microscopic images of droplets with protein crystals of thaumatin. Image reprinted by permission from ref. [34], Copyright 2014. (c) Transmission electron microscopy (TEM) images of Palladium (Pd) nanocrystals using seeded growth with well-controlled sizes and shapes. Image reprinted from ref. [36]. (d) Encapsulation and cultivation of bacteria inside a droplet. Image reprinted by permission from ref. [39], Copyright 2009, John Wiley & Sons. (e) Spatial assembly of different cells in the 3D core–shell scaffold forming an artificial liver in a droplet. Image reprinted by permission from ref. [40], Copyright 2016, Royal Society of Chemistry. (f) Performance of the tapered immobilization channel array for immobilizing and imaging of C. elegans in a droplet. Image reprinted by permission from ref. [42], Copyright 2010, Royal Society of Chemistry.

Liquid-liquid interface instability leads to droplet breakup in multiphase systems. Based on the mechanism of interface agitation and presence of external sources of energy, microfluidic droplet generation techniques are divided into two major categories of active and passive techniques (Figure 1-3). In active methods interfaces are ruptured with the assistance of external sources of energy such as electric field [44], magnetic field [45], mechanical vibration [46] and acoustic waves [47]. On the other hand, in the passive droplet generation methods, there is no external energy involved while channel geometry and fluid properties are specifically designed to intensify fluid instabilities and interface breakup into diminutive volumes of dispersed-phase (d-phase)

droplets inside a continuous-phase (c-phase) immiscible fluid. Major active and passive droplet generation methods are reviewed in the following two sub-sections.
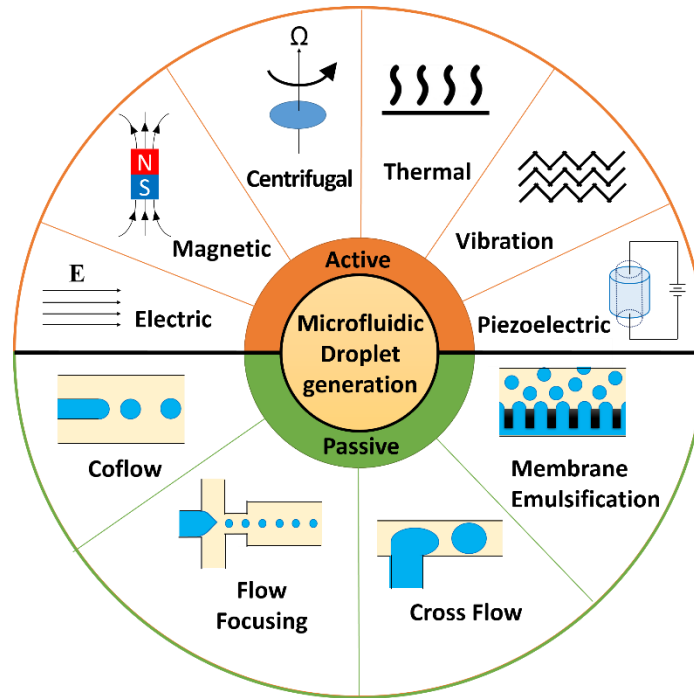
Figure 1-3. Graphical abstract of microfluidic droplet generation techniques. Upper half shows the active methods while lower half summarizes the passive methods.

1.3.1 Active Microfluidic Droplet Generation

In active methods, an external source of energy is introduced to manipulate the force balance in the system. Manipulation could be done either by adding an extra force or adjusting existing forces in the system. While electric [44], magnetic [45], and centrifugal [48, 49] actuations impose an additional force to the system, optical and thermal [50, 51] manipulations, mechanical vibration [46], acoustic waves [47] and piezoelectric actuators [52] intensify the instability of interfaces by modifying the physical properties of the fluids or adjusting the channel dimensions. Active droplet

generation with the aid of external actuators and sources of energy offers good control (CV[1] <5%)

and flexibility in terms of droplet size (from femtoliter-scale to nanoliter-scale) and throughput (

> kHz) [53]. On-demand droplet generation is another important characteristic of active methods.

In passive methods, droplet size and throughput are not independent while active methods enable

us to independently produce different sizes of droplets at desired throughputs. However, nature of

the dominant forces can restrict the type of materials that can be used in active methods. Wang et

al. [54] and Nugyen et al. [55] have recently published comprehensive reviews on active droplet

generation methods in microfluidics. Table 1-1, compares different active droplet generation

techniques in the literature.

---

[1] Coefficient of Variance, defined as ratio of standard deviation of droplets to the average diameter.

Table 1-1. Active droplet generation methods

Type of control	Mechanism	Implementation	Device Geometry	Type of droplet generation†	Ref
Electrical	Electric force	Constant DC	Flow-focusing	Tunable	[56–58]
		Low-frequency AC	Flow-focusing	Tunable	[59]
		High-frequency AC	Flow-focusing	Tunable	[60]
		DC pulse	T-junction	On-demand	[61]
		High-frequency AC	Flow-focusing	On-demand	[62]
Magnetic	Magnetic force	Uniform field	Flow-focusing	Tunable	[63, 64]
			T-junction	Tunable	[65]
		Non-uniform field	T-junction	Tunable	[66]
			Step-emulsification	On-demand	[67]
Centrifugal	Centrifugal/Coriolis/Euler forces	Rotation	Dispenser nozzle	Tunable	[48, 49]
			Cross-flow	Tunable	[68]
Optical	Modifying fluid pressure	Laser pulse	T-junction	On-demand	[50]
	Marangoni effect	Laser heating	T-junction	Tunable	[69]
			Cross-flow	Tunable	[70]
	Photosensitive surfactant	UV/blue light	Flow-focusing	Tunable	[71]
Thermal	Temperature dependence of viscosity	Heating	T-junction	Tunable	[51]
	Interfacial tension		Flow-focusing	Tunable	[72]
	Marangoni effect		T-junction	Tunable	[73]
Mechanical	Modifying fluid pressure	Mechanical vibration	Cross-flow	Tunable	[46, 74, 75]
			T-junction	On-demand	[76]
	Channel deformation/blocking	Piezoelectric actuator	Flow-focusing	Tunable	[52]
			T-junction	Tunable	[77]
	Interface instability	Acoustic wave	T-junction	Tunable	[78]
			Flow-focusing	Tunable	[79]

† **Tunable:** droplet generation with tunable size and production rate; **on-demand:** on-demand droplet generation

1.3.2 Passive Microfluidic Droplet Generation

In passive methods, a dispersed phase (d-phase) fluid is introduced through different arrangements of channels into a continuous-phase (c-phase) fluid while various passive mechanisms are used to generate droplets of d-phase inside the c-phase fluid. Typical passive microfluidic droplet generation devices mainly operate in two distinct modes. In some of them, shear forces are used to break off the droplets. Examples include the co-flow [80, 81], flow focusing [82–84] and cross flow (T & Y junctions) [85, 86] techniques. Some others employ variations of channel confinement to facilitate or drive droplet generation. Step emulsification [87] and membrane emulsification [88, 89] devices are examples of this technique. These major passive droplet generation methods are reviewed below.

Co-flow Droplet Generation (Focus in this Research)

Microfluidic co-flow droplet generation was first introduced by Umbanhowar et al. [80] and is one of the most commonly used techniques in microfluidic droplet generation due to its simplicity and relatively low cost. Figure 1-4 illustrates a schematic of a co-flow device where c-phase and d-phase fluids are flown through parallel channels into a main channel with flow rates of Q_c and Q_d, respectively. Owing to the design of the channels, the growing interface of d-phase flow is exposed to shear forces imposed by the c-phase flow, resulting in controllable and stable generation of droplets. Flow conditions play an important role in size, throughput and monodispersity of droplets.
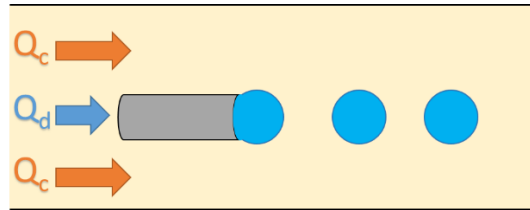
Figure 1-4. Schematic of co-flow droplet generation device.

Usually, the diameter of generated droplets in this technique are highly monodispersed with small coefficient of variation (CV<3%) [80] and sizes that are larger than the d-phase channel dimensions [90]. However, exceptions are observed at very high speed c-phase flows [90–92].

Flow Focusing Droplet Generation

In 2003, Anna et al. [93] introduced the first liquid–liquid flow focusing microfluidic systems. Flow focusing devices (as shown in Figure 1-5) are geometrically similar to co-flow devices, except that there is a contraction in c-phase channel where droplet breakup takes place. Due to the reduction in cross-sectional area of the contraction region, c- and d-phase flow velocities increase and the d-phase fluid elongates into the c-phase fluid at the contraction region. This results in enhancement of the shear forces applied to the droplet and extensively reduces the size of generated droplets. It has been shown that 3D-axisymmetric flow-focusing devices are advantageous over planar devices, shown in Figure 1-5a and Figure 1-5b respectively, mainly because the d-phase flow is not in direct contact with the channel walls avoiding potential problems raised by wall wetting. Therefore, produced droplets with 3D-axisymmetric flow-focusing devices are sufficiently monodisperse (CV<5%) [83]. Planar devices are mostly fabricated by soft lithography methods [94] while 3D-axisymmetric devices are composed of several micro-

11

capillaries with different shapes (usually a pulled capillary coaxially embedded in a larger capillary).

(a)   (b)
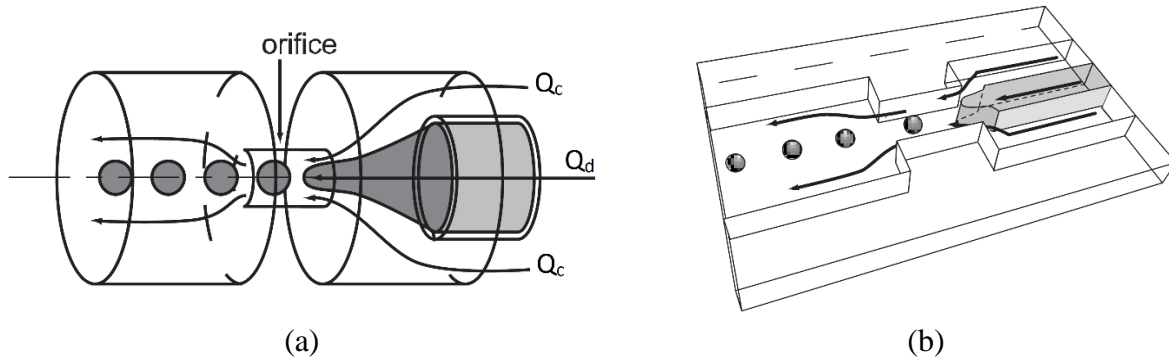
Figure 1-5. Schematic of (a) 3d axisymmetric flow focusing device with circular cross section and (b) 2d flow focusing device with rectangular cross section [83].

Cross-Flow Droplet Generation

In cross-flow devices (Figure 1-6), c-phase and d-phase fluid carrier channels meet at an angle θ $(0° < \theta \leq 180°)$[95]. T-junction cross-flow devices (Figure 1-6a) where $\theta = 90°$ are the most conventional and were first introduced by Thorsen et al. [85] for water-in-oil droplet generation. Y-junctions are other examples of cross flow devices as illustrated in Figure 1-6. Two immiscible liquids are introduced at the junction and as the flow continues, the d-phase fluid penetrates into the c-phase channel. Pressure gradient and drag forces imposed by the c-phase stream shear off the growing d-phase droplet or plug. The size of generated droplets and plugs are easily controllable by channel dimensions, d-phase and c-phase flow rates and viscosity ratio of the immiscible phases. T-junction devices have simple geometry and are easy to fabricate while yielding droplets with adequate monodispersity (usually CV< 2%)[96].

12

(a)   *(b)*
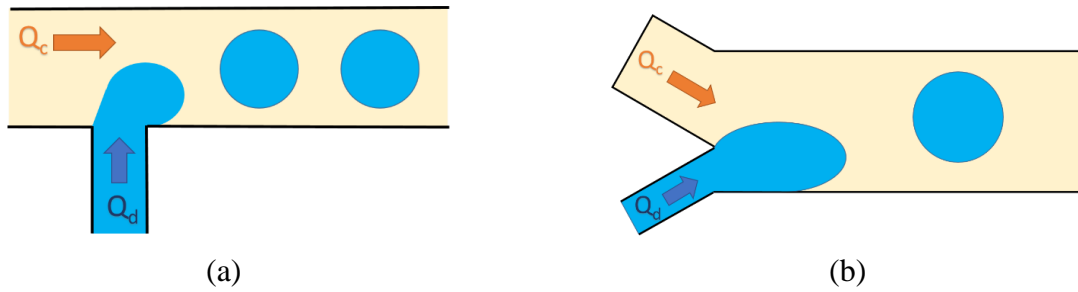
Figure 1-6. Schematic of cross-junction device with (a) T-junction and (b) Y-junction configurations. In both devices pressure gradient and drag force are imposed by the c-phase stream on the growing droplet/plug resulting into breakup.

Step- and Membrane-emulsification Devices

All the aforementioned microfluidic devices employ shear forces to destabilize the interface and accomplish droplet breakup. Conversely, in step and membrane emulsification devices, respectively shown in Figure 1-7a and Figure 1-7b, variations in channel confinements generate abrupt changes in capillary pressure leading to interfacial tension driven droplet breakup. Thus, droplet generation in step-emulsification is less sensitive to flow variations or pressure fluctuations, which results in highly monodispersed droplets (CV<1.5%)[54]. However, membrane emulsification, widely used in industry due to its higher throughput, is not as accurate as step emulsification and generates droplets of quasi-monodisperse nature (CV~20%)[88].

(a)   *(b)*
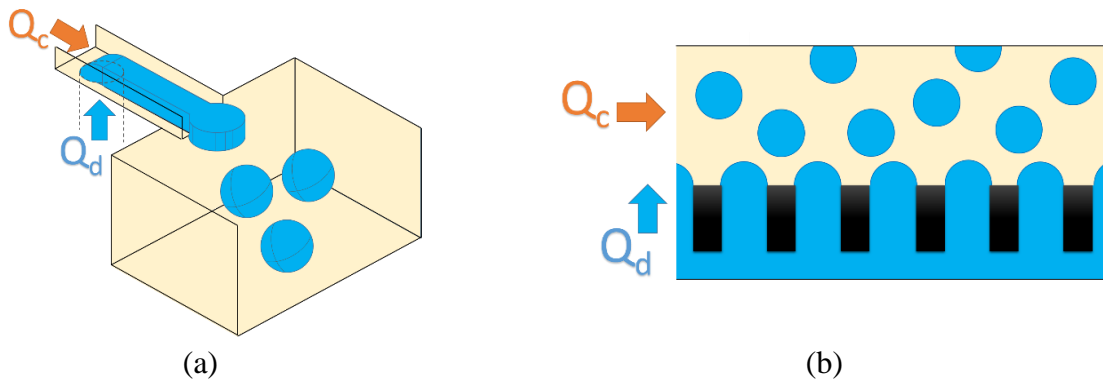
Figure 1-7. Capillary driven emulsification microfluidic devices. (a) Step and (b) membrane emulsification methods are shown schematically.

13

A summary of passive droplet generation methods and their performance characteristics is presented in Table 1-2.

Table 1-2. Passive droplet generation methods

Droplet generator	Droplet generation rate	Minimum Droplet size	Monodispersity	Ref.
Co-flow	Several hundred Hz to tens of kHz	Several hundred nanometers	CV <3%	[80, 81]
Flow-focusing	Up to tens of kHz	Several hundred nanometers	CV <5%	[83, 84]
Cross-flow	Up to 7.4 kHz in air-bubble-triggered droplet formation	Limited by channel dimension, usually larger than 10 μm	CV <2%	[85, 86, 96]
Step emulsification	Up to 15 kHz	Several hundred nanometers	CV <1%	[87]
Membrane emulsification	Several tons of dispersed phase per hour	~0.1 μm	CV ~20%	[88, 89]

1.3.3 Multi-Size Microfluidic Droplet Generation Methods

Modern chemical and biological applications require size-optimized droplets for effective encapsulation of analytes and reagents. In order to perform size optimization, different-size droplets must be generated from identical sources of samples to prevent potential cross-sample variations or other sources of error. For instance, Polymerase Chain Reaction (PCR) is a widely used technique in gene amplification and analysis which requires the usage of costly reagents. This method has become more cost-efficient by reducing the reagent consumption rate offered by droplet-based microfluidics [97]. Moreover, some of the potential problems of benchtop PCR technique such as evaporation loss and non-specific surface adsorption can be prevented in droplet based PCR [98]. In this method different analytes and reagents are encapsulated in droplets with different sizes [99] undergoing a series of thermally-activated chemical reactions. However, a potential challenge that can be faced in droplet-based PCR is the non-uniform encapsulation of template molecules and reagents in small droplets especially while dealing with very low concentrations of reagents. This may lead to non-uniform amplification of the desired template if the droplets are single-sized [98]. In order to account for this effect, preferably a variety of desired-size droplets are needed to be concurrently generated from identical reagents for size optimization processes. Multi-sized monodispersed droplets are also highly demanded in colloidal bead assembly fabrication that are extensively used in multiplex bioassay applications [100, 101].

Many researchers have developed integrated microfluidic chips for multi-size droplet generation, which consist of several simple components with different channel dimensions as reviewed before (e.g. flow focusing or T-junction). Integrated multi-component devices are fabricated to achieve either of the two main functionalities of (1) generating monodisperse droplets with increased throughput or (2) generating multiple-size droplets on a single chip [102, 103]. For example, Li et

al. [104] fabricated an integrated quadra-droplet generator (QDG) comprised of four parallel flow focusing devices (FFD) with various channel dimensions as shown in Figure 1-8.
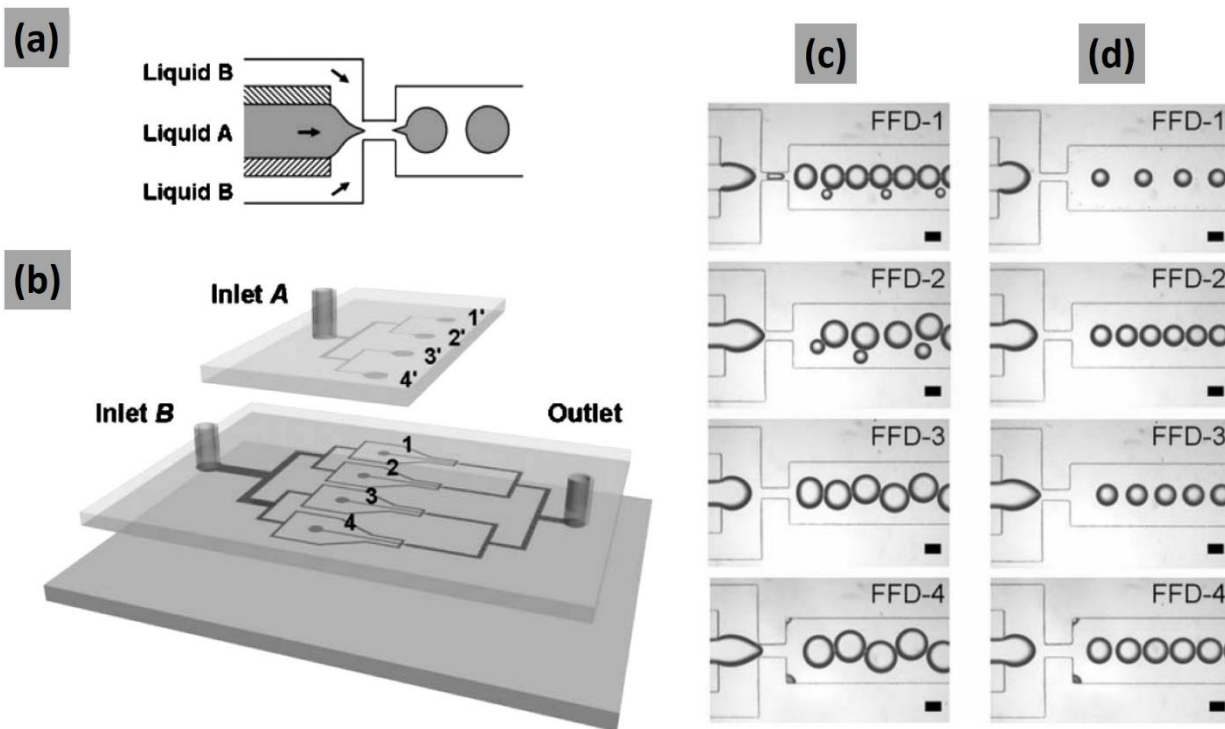
Figure 1-8. Design of a microfluidic quadruple-droplet generator (QDG) comprised of four parallel flow focusing devices (FFD). (a) Schematic of an individual flow-focusing droplet generator. (b) Three-dimensional illustration of the QDG. The mean orifice widths of FFD-1 to FFD-4 were 50.7 ± 1.0 μm, 50.8 ± 1.0 μm, 48 ± 1.0 μm and 48.8 ± 1.0 μm. The height of QDG is 150 ± 2.0 μm. (c-d) Optical microscopy images of droplets generated in the QDG comprising four FFDs with different widths of the orifices. (c) Q_A = 0.2 mL/h, Q_B = 1.0 mL/h. (d) Q_A = 0.2 mL/h, Q_B = 2.0 mL/h. Scale bar = 100 μm. Images reprinted by permission from ref. [105] , Copyright 2008, Royal Society of Chemistry.

The results showed that in QDG devices with four identical channel dimensions, generation of one droplet in a particular FFD affected the droplet generation in the other units. It was concluded that the polydispersity of droplets in this geometry were broader compared to the QDG with four distinct channel geometries.

Hashimoto et al. [106] studied parallel bubble and droplet formation in integrated FFD composed of single, double, and quadruple flow focusing units as illustrated in Figure 1-9.

16
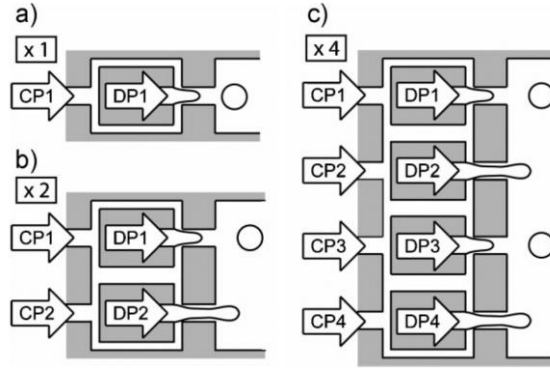
Figure 1-9. Schematic illustration of the systems of flow-focusing generators. (a) Single, (b) double, and (c) quadruple flow-focusing generator. Water/nitrogen gas and hexadecane/water were used as c-phase/d-phase fluids for bubble and droplet generation, respectively. All generators in a system shared a common outlet channel. Images reprinted by permission from ref. [106], Copyright 2008, John Wiley and Sons.

As shown in Figure 1-10, the generated bubbles were affected by the adjacent flow streams and bubble formation dynamics were complex. With gas at low pressures, each generator produced monodisperse or bi-disperse bubbles, and the sizes of bubbles that formed in different generators varied. At high pressures, all equivalent generators of a system produced monodisperse bubbles. For a wide range of pressures, the timing of breakup of bubbles in neighboring generators alternated.
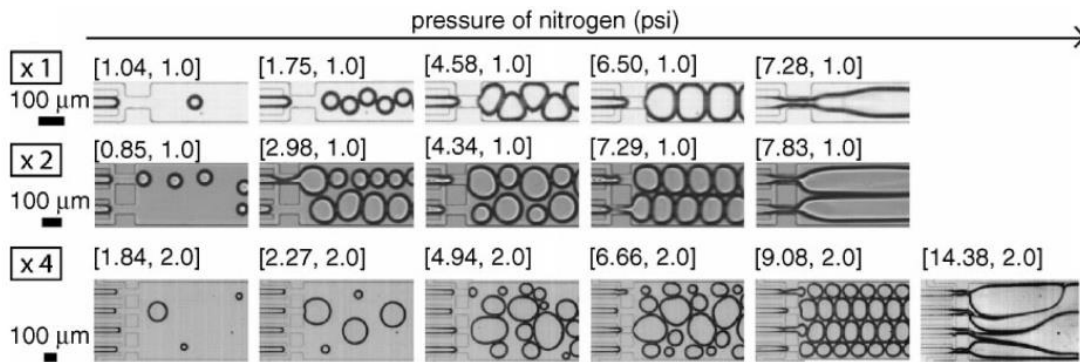
Figure 1-10. Optical micrographs of nitrogen bubbles in water showing representative behaviors of one-, two-, and four-orifice systems. The micrographs show the transition of the pattern of break-up upon a stepwise increase in the pressure of nitrogen, with the rate of flow of water held constant (the direction of flow is from left to right). The one-orifice system displayed only simple dynamics by generating monodisperse bubbles for a wide range of flow parameters (both p and Q), while two- and four-orifice systems displayed complex dynamic responses. Images reprinted by permission from ref. [106], Copyright 2008, John Wiley and Sons.

Unlike bubbles, droplet formation, shown in Figure 1-11, was more stable and each unit was able to operate independently, producing monodisperse droplets. Single orifice droplet generation unit was able to generate monodisperse droplets with a diameter range of 50μm up to couple of hundred microns. Double orifice device approximately generated similar sizes of droplets as single orifice unit at identical operating conditions. They observed simultaneous and alternative droplet generation in double and quadruple coupled devices which was the signature of weak hydrodynamic coupling between units. Their observations suggested that the compressibility of the d-phase (e.g., the gas or liquid), and variations in pressure at the flow-focusing orifices are controlling the interface interactions and breakup mechanism.
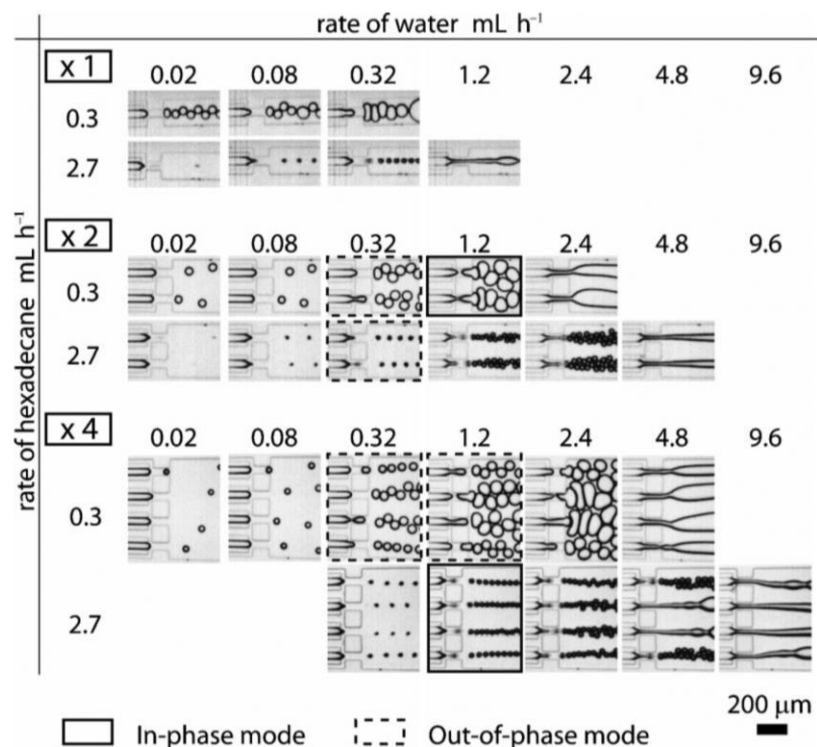
Figure 1-11. Optical micrographs showing the formation of droplets of water in hexadecane (with Span 80,3%w/w) in coupled flow-focusing generators. Size of generated droplets were directly proportional to d-phase flow rate (from left to right). Micrographs marked with solid rectangles represent the in-phase and those marked with dashed rectangles represent the out-of-phase mode of operation of the generators. Images reprinted by permission from ref. [106], Copyright 2008, John Wiley and Sons.

Zhou et al. [107] used 16 Y-junctions in parallel (shown in Figure 1-12a and Figure 1-12b) to increase the droplet generation throughput of water-in-oil. They investigated the effect of parallelization, flow rate ratio and physical properties of different c-phase liquids on high-throughput, monodisperse emulsification with low energy consumption.
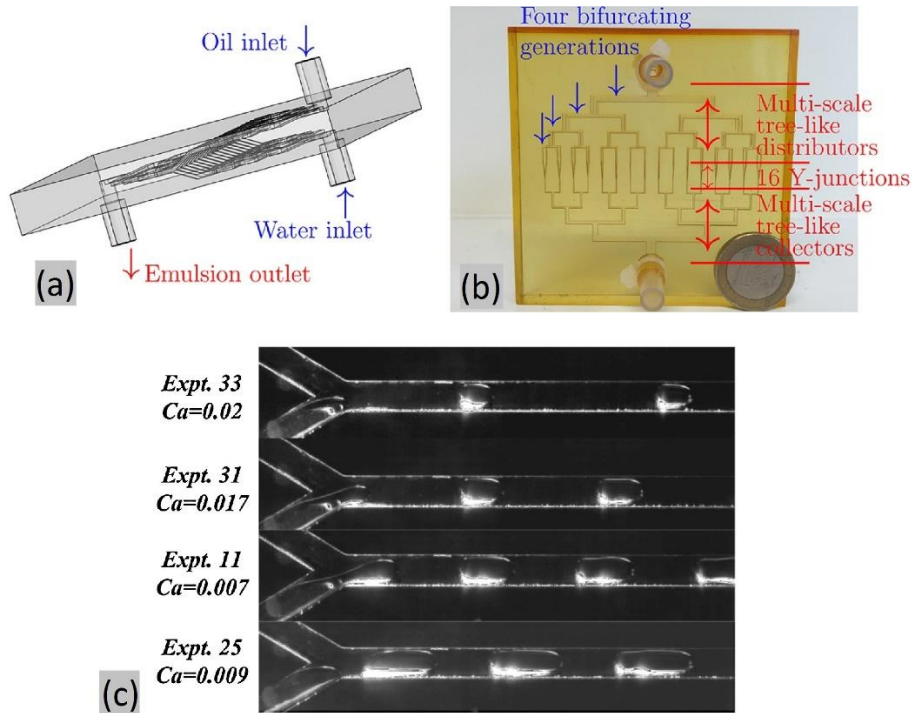
Figure 1-12. Parallel minichannel contactor for water-in-oil emulsification. (a) Side view schematic and (b) photograph (front view - oil and water inlets are at the top) of the device next to a 1€ coin. (c) Photographs of the oil-water two-phase flow in a single Y-junction minichannel replica. Images reprinted by permission from ref. [107], Copyright 2017, Elsevier.

Zhou et al.[107] investigated the flow regimes and the influences of the two-phase flow physical properties on the polydispersity of emulsion. For water-in-oil flows through the single Y-junction replica, shown in Figure 1-12c, an apparent droplet flow and a characterized plug flow were observed. The length of droplets and plugs could be predicted by the correlations in the literature. Single Y-junction replica and the parallel minichannel contactor both showed capability to generate monodisperse droplets for water-pure oil system.

1.4 Working Principles of Co-Flow Microfluidic Droplet Generation

The co-flow technique reviewed in the previous section is one of the most commonly used methods for droplet generation. Many researchers have attempted to understand the interfacial breakup dynamics of co-flow and other droplet generation methods [108–110]. As shown in Figure 1-13, by injecting a d-phase fluid via a nozzle into a flowing c-phase fluid coaxially, interfacial forces (F_γ in Eq. 1) assist the penetrated d-phase to form a growing droplet at the tip of the nozzle while the viscous drag force (F_D in Eq. 2) imposed by the c-phase flow seeks to detach the growing droplet. The drag force increases by droplet growth up to the point that breakup-assisting forces overcome the breakup-resisting forces. At this point, while the diameter of d-phase column decreases to zero, the radial curvature (inversed radius of the column) increases to infinity. This leads to occurrence of finite time singularities in droplet breakup. Right after this point, surface tension (not a breakup resisting force anymore) encloses the interface to minimize the surface energy and form a droplet [111, 112]. Under constant c- and d-phase flow rate conditions, the axial shear and interfacial capillary remain constant and force balance occurs at a specific volume leading to generation of single-size monodisperse droplets.
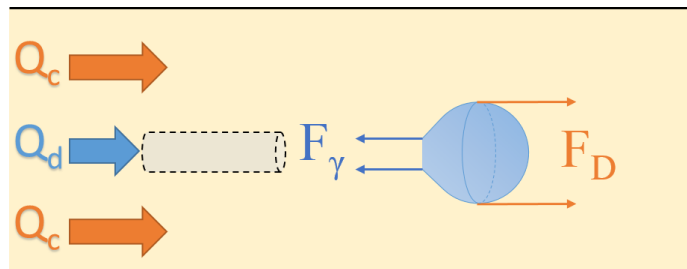
Figure 1-13. Force balance on a growing droplet in a co-flow geometry showing the drag (F_D) and interfacial capillary (F_γ) forces on a droplet right before separation from the dispensing nozzle.

$$F_\gamma = \gamma \pi D_n \qquad\qquad (1)$$

$$F_D = \frac{1}{2}\rho A C_D V^2 \qquad\qquad (2)$$

where γ [N/m] is interfacial tension, D_n [m] is characteristic length (nozzle diameter), ρ [kg/m^3] is density, A [m^2] is cross-sectional area of the droplet, C_D is drag coefficient and V [m/s] is flow velocity.

Depending on the c- and d-phase fluid velocities and the dominance of aforementioned forces, generation of droplets can occur in different regimes in a co-flow device (Figure 1-14). When the d-phase fluid is pumped at low flow rates into the surrounding flowing c-phase, capillary forces become dominant and droplets start to form at the tip of the nozzle. In this regime that is known as dripping (Figure 1-14a), instabilities grow at fixed locations in space and are not affected by external noises [113]. As a result, droplets generated due to absolute instability in the dripping regime are highly monodispersed [80]. However, at high d-phase flow rates used to enhance the throughput, the inertial and viscous forces become comparable to the interfacial force and the d-phase liquid starts to elongate like a thread inside the c-phase fluid. Accordingly, the droplet dripping (breakup) location is pushed to the end-tail of the elongated thread. This is known as the jetting regime (Figure 1-14b) in which the convective instabilities dominate the breakup mechanism and perturbations moving across the interface of the jet can amplify a random noise leading to generation of polydisperse droplets [70, 90, 114].
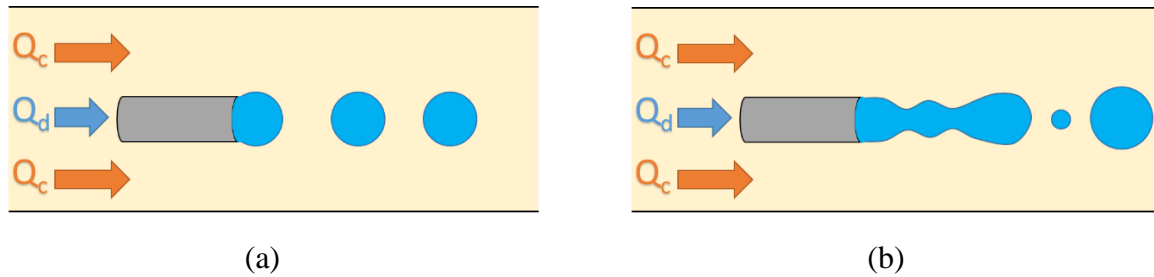
Figure 1-14. Droplet generation regimes in co-flow devices. (a) Dripping regime with monodispersed droplet generation. (b) Jetting regime with polydisperse droplet generation.

The preliminary steps to study instability waves motion on interface and liquid column disintegration into droplets were taken by Plateau [115] and Lord Rayleigh [116, 117]. Tomotika [118] extended Rayleigh's linear instability analysis of a free surface liquid jet breakup to the submerged jet analysis. The approach is applicable to jet length and droplet size prediction in the axisymmetric jetting regime and is more accurate when the jet speed is the same as the c-phase velocity [119]. Meister and colleagues [120, 121] developed their theory of droplet formation for both dripping and jetting regimes. Many researchers carried out numerical simulations for jet breakup mechanism and droplet size distribution [122–124].

After understanding the basic physics of breakup in co-flow droplet generation devices, important dimensionless numbers that represent the competition between the abovementioned forces must be introduced. The dimensionless numbers identify the dominant phenomena in each case by comparing the magnitude of competing forces. In the next section, we will introduce the important dimensionless numbers in microfluidics and use them to elaborate more on the breakup regimes in different conditions.

1.4.1 Dimensionless Numbers in Droplet Generation

Different phenomena occur in microfluidic devices and in order to have control on their operation, their dominant and governing physical principles must be determined and well-understood. As stated above and summarized analytically in reference [53], there are four main types of forces governing droplet generation in microfluidic devices, i.e. inertial, viscous, capillary (interfacial) and gravity (buoyancy) forces. Dimensional analysis can be used to gain understanding of the dominance of these forces and the physics governing the fluids in all microfluidic droplet generation systems. These analyses result in dimensionless numbers that indicate the relative ratio and predominance of different competing forces or their equivalent stresses in droplet microfluidics. Some of the important dimensionless numbers are summarized in Table 1-3. Important dimensionless and further discussed in the rest of this section.

Table 1-3. Important dimensionless numbers in droplet microfluidics

Symbol	Name	Formula	Force or Property Ratio
Re	Reynolds number	$Re = \dfrac{\rho V L}{\mu}$	Inertial to viscous forces
Ca	Capillary number	$Ca = \dfrac{\mu V}{\gamma}$	Viscous to interfacial forces
We	Weber number	$We = \dfrac{\rho L V^2}{\gamma}$	Inertial to interfacial forces
Bo	Bond number	$Bo = \dfrac{\Delta \rho \, g L^2}{\gamma}$	Buoyancy to interfacial forces
λ	Viscosity ratio	$\lambda = \mu_d / \mu_c$	d-phase to c-phase viscosity ratio
φ	Flow rate ratio	$\varphi = Q_d / Q_c$	d-phase to c-phase flow rate ratio
α	Density ratio	$\alpha = \rho_d / \rho_c$	d-phase to c-phase density ratio

The dimensionless numbers that scale with a characteristic system length such as channel size are affected by miniaturization of the system. Accordingly, droplet generation physics in microsystems deviate from macroscale devices due to their smaller length scales. In other cases where the dimensionless numbers are independent from length-scale, they still have important implications on the flow and droplet generation behavior.

Reynolds Number

Starting with inertial and viscous stresses, the relative importance of these stresses yield to Reynolds number defined in Eq. 3.

$$Re = \frac{\rho V L}{\mu}$$
(3)

where, ρ [kg/m^3] is density, V [m/s] is velocity, L [m] is the characteristic length and μ [Pa.s] is viscosity.

Due to inherently small dimensions and low velocity of fluids in microfluidic devices, Re usually ranges from 10^{-6} to 10 [53]. Therefore, viscous forces are either considerable or dominant over inertial forces in microfluidic systems. Re number is used less frequently in droplet generation systems since inertial forces do not play a significant role in droplet breakup.

Capillary Number

Droplet breakup occurs in three stages. First d-phase and c-phase meet at the dispersion point forming an immiscible interface. Then, this interface deforms and forms a growing droplet and

24

finally becomes unstable and disintegrates into a discrete droplet. Thus, interfacial forces and stresses play an important role in droplet microfluidics and a comparison of other stresses with interfacial stress could be beneficial. Comparing viscous to interfacial (or capillary pressure) stresses reveals a dimensionless number known as the Capillary number shown in Eq. 4.

$$Ca = \frac{\mu V}{\gamma} \qquad (4)$$

where, μ [Pa.s] is viscosity, V [m/s] is velocity and γ is interfacial tension [N/m].

If the characteristic length is sufficiently small in a channel, viscous and interfacial effects would become dominant over inertial and gravity forces. Ca number is one of the most frequently used dimensionless number in droplet generation and ranges from 10^{-3} to 10 [53].

Weber Number

The competition between inertial and interfacial (capillary) stresses is captured by the Weber number shown in Eq. 5.

$$We = \frac{\rho L V^2}{\gamma} \qquad (5)$$

where, ρ [kg/m^3] is density, L [m] is the characteristic length, V [m/s] is velocity and γ [N/m] is interfacial tension.

In most of the microfluidic applications and due to the limited velocity of flow, fluid inertia is negligible. However, in some cases like jetting [90][125] and nonlinear bubble formation [126] where high flow velocities are used, inertia con no longer be neglected.

Bond Number

A comparison of relative strengths of gravitational to interfacial stresses can be represented by the Bond number shown in Eq. 6.
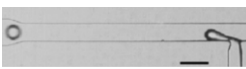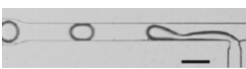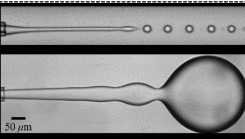
$$Bo = \frac{\Delta\rho \, gL^2}{\gamma} \tag{6}$$

where, $\Delta\rho$ [kg/m^3] is density difference, g [m/s^2] is gravitational acceleration, L [m] is the characteristic length and γ [N/m] is interfacial tension. The buoyancy force arises by the difference in density of the d-phase and c-phase fluids in a gravitational field. Generally, density difference and characteristic length scale are small in liquid-liquid droplet generation applications and thereby $Bo \ll 1$.

1.4.2 Breakup Modes in Droplet Microfluidics

Droplet formation is a result of interaction between competing forces. In shear-based droplet generators while surface tension assists droplet growth, viscous shear force resists swelling, and this competition leads to different breakup regimes. Breakup regimes observed in these devices have been categorized into five major modes of squeezing, dripping, jetting, tip-streaming and tip-multi-breaking [53]. Not all of these breakup modes are encountered in a device, for instance tip-streaming and tip-multi-breaking modes have not been reported in cross-flow devices [54]. A summary of breakup regimes and required flow conditions for each mode is provided in Table 1-4.

Table 1-4. Breakup regimes in shear based droplet generation microfluidic devices.

Regime	Flow Conditions	Cross-flow[2]	Co-flow[3,4,5]	Flow-focusing[6]
Squeezing	$Ca < Ca_{cr}$ $Ca_{cr} \approx O(10^{-2})$			
Dripping	$O(10^{-2}) < Ca < O(1)$ $We < O(1)$			
Jetting	$We + Ca \geq O(1)$			
Tip-streaming	$Re_c \ll 1 ; Ca > Ca_{cr}$ $Re_d \ll 1 ; \varphi \ll 1$	Not Reported.		
Tip-multi-breaking	$\varphi < \varphi_{min} \ll 1$ $Ca > Ca_{cr}$	Not Reported.		

[2] All images for different regimes in cross-flow devices are reprinted by permission from ref. [160], Copyright 2010, American Physical Society.

[3] Image for squeezing regime in co-flow devices are reprinted with permission from ref [161]. Copyright 2007, American physical society.

[4] Images for dripping and jetting regimes in co-flow devices are reprinted with permission from ref ref [90]. Copyright 2007, American physical society.

[5] Images for tip-streaming and tip-multi-breaking regimes in co-flow devices are reprinted with permission from ref. [91]. Copyright 2013, Cambridge University Press

[6] Various regimes observed in flow focusing devices are also reprinted from ref [127].

Squeezing

At low capillary numbers, where d-phase liquid obstructs a main portion of the channel, a pressure gradient is generated around the growing interface. By increasing the size of d-phase interface, this gradient increases and when it is sufficiently large to overcome the internal pressure in the droplet, the interface "squeezes" and a neck emerges leading to disintegration of the d-phase. The detached phase is considerably large compared to the channel and due to the confinement of channel walls usually forms a plug rather than a spherical droplet. Thus, squeezing regime is usually referred to as "geometry-controlled" mode in the literature [127, 128].

Dripping

As the Capillary number increases, the viscous forces become more dominant and the role of pressure gradient is substituted by viscous forces imposed by the c-phase flow counteracting the interfacial force. In the dripping regime, droplet breakup occurs at the tip of the d-phase channel, nozzle or focusing region in shear-based passive droplet generation devices. Due to increased levels of drag forces, breakup occurs in smaller droplet sizes where the droplets retain their spherical shape and no more plug is observed in this regime. The generated droplets are highly monodispersed due to the absolute instability in the dripping regime [80].

Jetting

At increased levels of either d-phase or c-phase flow rates, a transition from dripping to jetting is encountered [114]. In the jetting regime, d-phase liquid starts to elongate like a thread inside the c-phase fluid. Accordingly, the droplet breakup location is pushed to the end-tail of the elongated

thread. Convective instabilities dominate the breakup mechanism in this regime and perturbations moving across the interface of the jet can amplify a random noise leading to generation of polydisperse droplets [70, 90, 114]. For co-flow devices, jetting takes place when the sum of viscous forces imposed by c-phase flow and d-phase inertial forces overwhelm interfacial forces. Eq. 7 shows the jetting criteria in co-flow devices [114].

$$Ca + We \geq \sim 1 \tag{7}$$

According to Eq. 7, jetting regime in co-flow devices can take place under two conditions. First, when $Ca \geq \sim 1$, viscous forces are dominant and a thin thread of d-phase flow is stretched inside the c-phase channel due to high viscous shear rate, known as narrowing jetting regime. Second, when $We \geq \sim 1$, inertial force of d-phase is dominant and a wide jet emerges. Velocity of d-phase is higher compared to c-phase stream and due to the viscous shear force at the interface, d-phase flow slows down as it advances downstream. The deceleration of d-phase velocity yields into expanded jet diameters toward the end of the jet, which is known as widening jet [54, 114].

Tip-streaming

Under certain flow conditions for immiscible fluids with viscosity ratio much less than unity, conical-shaped jets are observed. Droplet generation takes place at pointed tip of the jet which is also known as tip streaming [129]. Based on the results of Prosperetti et al. [130], tip-streaming is achievable when local streamlines converge near the interface and no flow separation is allowed between c-phase flow and droplet interface. To achieve conical form of jet, viscous forces imposed by c-phase flow must overcome the capillary pressure at the dispensing nozzle [81]. Thus, tip-

streaming has only been observed in co-flow and flow-focusing devices and is not plausible in cross-junction geometries. Size of the thin jet is smaller than the nozzle diameter, hence diameter of generated droplets can reach to submicron orders [131, 132].

Tip-multi-breaking

All formerly introduced droplet breakup modes generate continuous streams of droplets, while in tip-multi-breaking regime droplets are generated in sequential time intervals [127]. In tip-multi-breaking regime a conical jet shape similar to tip-streaming emerges, but the cone-structure is unstable. Oscillation of conical interface ceases continuous generation of droplets and in each time interval a batch of droplets with a size distribution is generated. The normalized droplet diameter d_{drop}/d_{tip} in tip-multi-breaking mode can be scaled with reversed Ca number [133]. The size of generated droplet trains can be predicted by correlations reported by ref. [127].

1.5 Research Opportunity

Co-flow technique is comprised of a d-phase dispersion nozzle concentrically embedded inside a channel that carries the c-phase fluid. It is one of the earliest, simplest and most frequently used techniques for droplet generation in both macro- and micro-scale. Microfluidic droplet generation techniques are assessed by their throughput and monodispersity of droplet generation. All conventional droplet generation methods can controllably produce monodisperse droplets at high throughputs [53, 55]. Although there is adequate control on size and monodispersity in the dripping regime, these conventional devices cannot generate more than one droplet size at a time in a continuous, high-throughput and monodispersed manner, unless flow rates or fluid properties are manipulated. Moreover, polydispersity of generated droplets in the jetting regime still remains as a challenge in co-flow droplet generation devices. Below, we discuss two unique technological gaps that our research has attempted to address.

1.5.1 Multi-size Monodisperse Droplet Generation

To the best of our knowledge, few researchers have addressed the continuous generation of multi-size, monodisperse droplets in microfluidic devices. These devices that were reviewed above suffer from the constraints of fixed channel geometry. In these devices, droplet diameter can be adjusted only by two methods: (1) modifying physical properties of liquids which is not desired or even applicable in some conditions and (2) tuning the c- and d-phase flow rates which is limited with the pressure durability of microfluidic devices. Moreover, the diameter of generated droplets are generally larger than the nozzle dimensions which limits the size-range of generated droplets in conventional methods. Thus, an important area in the field of droplet microfluidics is the

fabrication of dynamically tunable devices capable of spontaneous generation of multi-size monodisperse droplets in a wide range of diameters (especially with sizes smaller than nozzle dimensions).

1.5.2 Jet Length Reduction

Droplet monodispersity and throughput of co-flow geometry is limited by the d- and c-phase flow rates. Achieving high throughputs requires high d-phase flow rates resulting in a transition from the dripping to the jetting regime, as described before. By increasing the d-phase flow rate beyond a critical value, convective instabilities in the jet emerge and generated droplets become polydispersed [70, 90, 114] which is not desirable. Accordingly, studying the jetting regime and developing novel techniques to ideally inhibit jetting or to reduce the jet length remains a challenge in co-flow droplet generation systems.

Considering the abovementioned discussions, we have found that spontaneous generation of multi-size monodisperse droplets at high throughput that involves jetting regime inhibition has not been investigated in the literature thus far. Accordingly, there are several unaddressed challenges in microfluidic co-flow droplet generation technique, some of which are listed below:

- Generating droplets with dimensions smaller than the nominal size of the dispensing d-phase nozzle.

- Spontaneous generation of multi-size, monodisperse droplets from identical reagents and with a wide range of dimensions.

- Ideally inhibiting the jetting regime or reducing the jet length to maintain monodispersity of droplets generated at increased d-phase flow rates.

32

1.6 Research Goal and Objectives

The main goal of this research project is multi-sized monodispersed droplet generation in a co-flow microfluidic device. To achieve this goal, the research project was broken down into several objectives as follows:

1. Introduce an axial shear force gradient to simultaneously generate multi-size droplets.

2. Introduce an additional transverse shear force to reduce the jet length and size of generated droplets.

3. Develop a characterization technique for clustering droplets generated in various sizes.

4. Perform parametric studies on the effect of axial shear, transverse shear, flow rates, and fluid properties on the number and size of generated droplets.

5. Perform parametric studies on the effect of axial shear, transverse shear, flow rates, and fluid properties on co-flow jet length.

1.7 Thesis Structure

This thesis has been categorized into six chapters, starting with an introduction to the importance of droplet based microfluidics and potential advantages of miniaturization. In the present chapter, working principles, dominant forces and important dimensionless numbers in droplet based microfluidics were introduced and microfluidic methods for droplet generation were reviewed to identify a research opportunity. The second chapter reports on the working principles of our proposed technique involving a secondary transverse shear in a co-flow device as well as methodologies and materials utilized to fabricate the device and achieve our goal and objectives. The third chapter summarizes the effect of different parameters on droplet generation in our co-flow device operated in the conventional axial shear mode (no transverse shear). In the fourth chapter, multi-size monodisperse droplet generation via oscillating the d-phase nozzle (to generated transverse shear) in our co-flow device is investigated. Effects of different parameters on the number and size distribution of generated droplets are studied. Chapter five elaborates on the application of our method on jet length reduction under different flow and transverse shear conditions. We also examine the effect of viscosity on jet length reduction. In chapter six, we provide a summary of the thesis and propose the future directions of our research. In the appendix section, we report the statistical method used in clustering our droplet size data followed by some supplementary graphs related to chapters four and five.

1.8 Author Contributions

Pouya Rezai conceived the idea of oscillatory needle for multi-size droplet generation assays and helped with device design, results interpretation, and revising manuscripts and the thesis. Amin Shams Khorrami designed and fabricated the experimental setup and microfluidic devices, performed all experiments and data analyses, and wrote the first drafts of the manuscripts and the thesis. He also received reviewer comments and applied them to these documents. Amin Shams Khorrami's scientific contributions to the field are listed below.

1.8.1 Journal Papers

- S. Khorrami, P. Rezai, "Oscillating Dispersed-Phase Nozzle in Co-Flow Microfluidic Droplet Generation Device: Jet Length Reduction Effect" Under preparation for submission to journal of Microfluidics and Nanofluidics.

- S. Khorrami, P. Rezai, "Oscillating Dispersed-Phase Co-Flow Microfluidic Droplet Generation: Multi Droplet Size Effect" Under preparation for submission to journal of Microfluidics and Nanofluidics.

1.8.2 Conference Papers

- A. S. Khorrami, P. Rezai, "A Novel Active Method For Jet Length Reduction In Microfluidic Co-Flow Droplet Generation Devices", MicroTAS 2017, Savannah, Georgia, USA, p. 750-751.

1.8.3 Honors and Awards

- Best Presenter Award (MASc), Mechanical Engineering Department Graduate Seminar Series 2017, York University.

Chapter 2

OSCILATORY CO-FLOW DROPLET GENERATION: WORKING PRINCIPLES AND METHODS

2.1 Proposed Oscillating Dispersed-Phase Co-Flow Droplet Generation Technique

Earlier discussions in Chapter 1 elaborated on the importance of simultaneous generation of multi-size monodisperse droplets from identical solution samples. Then important dimensionless parameters and dominant forces in droplet generation were discussed. After understanding the droplet mechanism, we aimed to design and fabricate a device that is capable of simultaneous generation of droplets with different sizes.

As stated in Chapter 1, in a conventional co-flow device, the d-phase nozzle is placed at the center of the c-phase channel with a parabolic velocity distribution to maximize the drag force on the growing droplet. This constant drag force, under constant c- and d-phase flow rate conditions, leads to generation of single-size monodisperse droplets. Clearly, a varying drag force is required to generate multi-size monodisperse droplets in a co-flow geometry. As shown schematically in Figure 2-1, we hypothesized that by positioning the co-flow dispensing nozzle across the channel width, the growing droplet will be exposed to various levels of axial drag owing to the parabolic distribution of c-phase velocity in the main channel. This may facilitate generation of multi-size, monodisperse droplets. Larger droplets are expected to be generated symmetrically at low velocity

regions close to the side walls and as the nozzle moves towards the center, axial velocity and drag increases while droplet size decreases.
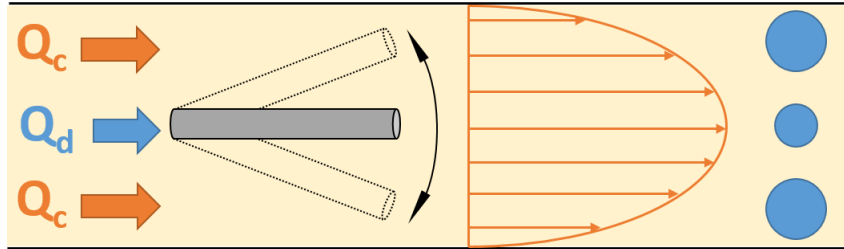
Figure 2-1. Hypothesized effect of parabolic c-phase velocity distribution and variable axial shear on the size of generated droplets at various lateral positions of the d-phase nozzle in a co-flow droplet generation device.

By continuous repositioning or oscillating the d-phase nozzle of a co-flow device, not only an axial drag force ($F_{D,A}$) gradient will be generated, but also a secondary transverse drag ($F_{D,T}$) will be induced due to the relative motion of the nozzle in the lateral direction. Figure 2-2 illustrates the force balance on the droplet growing on the tip of an oscillating nozzle when the effect of transverse drag is considerable. This additional drag force can play a crucial role in affecting the jet length and the droplet size depending on the magnitude of the axial drag.
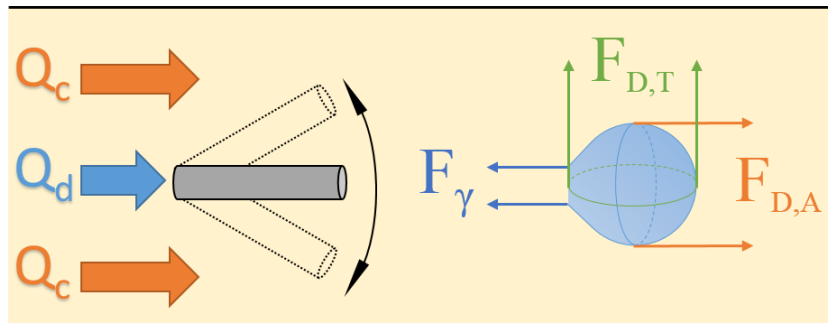
Figure 2-2. Force balance on a growing droplet in an oscillating dispersed-phase co-flow droplet generation technique. Upon needle oscillation the growing droplet, held by interfacial force (F_γ), experiences an axial drag gradient ($F_{D,A}$) while an additional drag force ($F_{D,T}$) is induced due to the relative motion of the nozzle in the lateral direction.

The oscillating dispersed-phase co-flow droplet generation device proposed in this section was fabricated and tested in our research, following the experimental procedures presented in the sections below.

2.2 Experimental Procedures

2.2.1 Materials

Polydimethylsiloxane or PDMS (Sylgard 184 kit, Dow Corning, USA) with 10:1 ratio of base monomer to curing agent was mixed thoroughly and degasified for casting onto a master mold for fabrication of co-flow droplet generation mini-channels. PDMS chips were bonded to microscope glass slides (Fisherbrand, Fisher Scientific, USA) for device enclosure. Short pieces of flexible silicon tubing (Masterflex, Cole-Parmer Instruments CO, USA) were used as external fluidic interconnects. Stainless steel needles (Gauge 27, ID=0.008", OD=0.016", McMaster-Carr, USA) with luer-lock connection were utilized as the dispensing nozzle in the mini-channels. The dispensing needles were embedded inside borosilicate capillaries (OD: 1.0mm, 1B100-4, World Precision Instruments, USA) to be centered inside the channel.

Corn oil (Mazola, ACH Food Companies Inc., USA) was used as c-phase liquid while different-ratio mixtures of Glycerol (Caledon Laboratory Chemicals, Canada) in deionized (DI) water (Milli-Q, Millipore Ltd, Canada) were used to create d-phase fluids with different viscosities [134]. Methylene blue dye in d-phase fluid was utilized to improve the image contrast and the edge detection quality in image processing. The solutions were blended thoroughly for 10 minutes with a magnetic stirrer before each set of experiments. Physical properties of liquids used in our studies are shown in Table 2-1. Corn oil-DI water interfacial tension is estimated to be $\gamma = 26.3 \times$

10^{-3} N/m [135]. Interfacial tension between all concentrations of glycerol/DI-water mixture and corn oil are assumed to be constant [136].

Table 2-1. Physical properties of corn oil [137, 138]*, DI water glycerol/DI-water* [134] *and Ethanol/DI water* [139] *mixtures used in the experiments.*

Liquid Type	Phase	Viscosity [mPa.s]	Surface tension [mN/m]
Corn oil	Continuous	86.4	33.80
DI-Water	Dispersed	1.0	71.68
20% (wt.) Glycerol/DI-Water	Dispersed	1.76	70.9
30% (wt.) Glycerol/DI-Water	Dispersed	2.5	70.32
50% (wt.) Glycerol/DI-Water	Dispersed	6.0	68.71
70% (wt.) Glycerol/DI-Water	Dispersed	22.5	66.8
10% (wt.) Ethanol/DI-Water	Dispersed	1.28	53.43
50% (wt.) Ethanol/DI-Water	Dispersed	3.08	31.36
100% (wt.) Ethanol/DI-Water	Dispersed	1.18	22.85

To generate aqueous two phase solutions (ATPS), Polyethylene Glycol (PEG, Mw 35K, Sigma Aldrich) and Dextran (DEX, Mw 500K, PHARMACOSMOS) were dissolved in DI-water. Aqueous stock solutions of PEG and DEX with concentrations of 6% (wt.) and 12.5% (wt.) were prepared and thoroughly mixed using magnetic stirrers for 10 minutes to form a turbid solution. Then the turbid solution was transferred into a valved-funnel and kept at 20˚C for one day to form two clear polymer-rich segregated phases. First DEX-rich phase (bottom phase) was extracted using the valve mounted at funnel's small end, then interface of two phases was collected in a separate container to avoid any cross-contamination between phases, and finally PEG-rich phase (top phase) was extracted into a separate container. The interfacial tension of ATPS is estimated to be $\gamma = 3.7 \times 10^{-5}$ N/m [140], which is 100 folds smaller compared to the conventional water-oil two phase systems.

2.2.2 Experimental setup

The experimental setup shown in Figure 2-3a consisted of a co-flow droplet generation device (see next section), high speed camera (Phantom V1611, Vision Research, USA), data acquisition system, two syringe pumps (LEGATO 110 & LEGATO 210, KD Scientific, USA), collecting container, oscillation mechanism, light source, reflection mirror, and custom-made fixtures. The light was reflected onto the device via a 45˚ angled mirror to lower the thermal effects on the device due to direct heat transfer from the light source. A 3D-printed barrel-cam/follower mechanism, shown in Figure 2-3b, was used to convert the rotational motion of a stepper motor, controlled by Arduino UNO chip, to linear transverse oscillatory motion of a needle inside the fluidic device (Figure 2-3c) with a 1:1 ratio. A linear slut, as shown in **Error! Reference source not found.**, was grooved on the barrel cam to ensure the linear motion of follower. A direct current power source (Keithley 2410, Tektronix, USA) was used to supply a 150~550 mA current to the stepper motor through a motor driver board (Rugged motor driver, Rugged Circuits, USA). The mechanism was designed in a way that the needle tip swiped 60% of the channel width in each oscillation to prevent contact with the side walls.

2.2.3 Device Design and Fabrication

The co-flow jet length reduction and droplet generation fluidic device shown in Figure 2-3c consisted of a needle embedded inside a capillary glass and positioned coaxially inside a PDMS mini-channel with one inlet and one outlet. The channel was 65 mm long, 5 mm wide, and 1.1 mm thick. The channel and needle inlets were used for infusion of c-phase and d-phase fluids, respectively, into the channel at desirable flow rates.
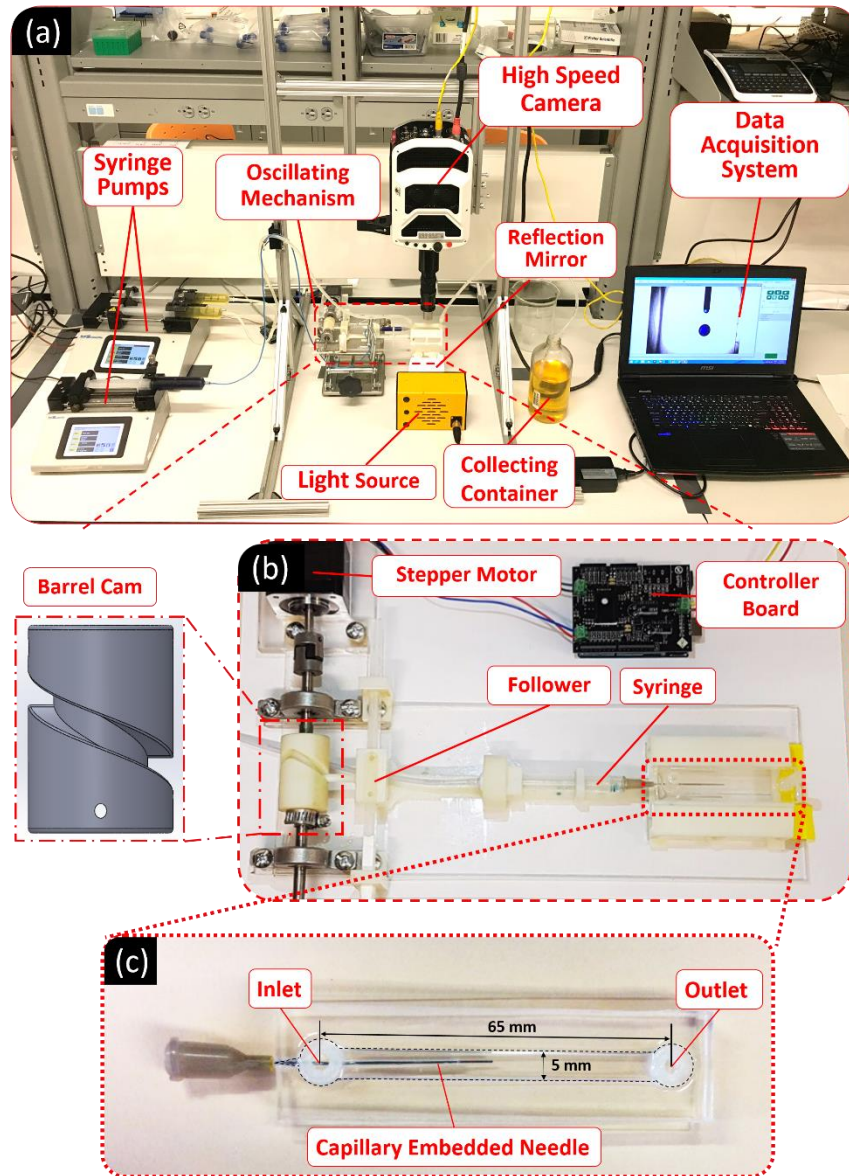
Figure 2-3. Co-flow jet length reduction and droplet generation system. (a) Experimental setup consisting of a fluidic device with a channel and an embedded coaxial droplet dispersion needle, high speed (HS) camera, two syringe pumps, power supplier, data acquisition system, collecting container, oscillation mechanism, light source and reflection mirror. (b) The barrel-cam-follower oscillation mechanism was custom-built to convert the rotational motion of the stepper motor into a linear transverse oscillatory motion of the needle inside the channel with 1:1 ratio. (c) The fluidic device with the needle inserted through a v-shaped groove into the channel with 1.1 mm height. The width and length of the channel were 5 mm and 65 mm, respectively. The edges are highlighted by dashed lines for better graphical display and visualization of the channel.

41

The width of the channel was selected large enough to allow a peak-to-peak oscillation range of 3 mm for the needle tip (and hence the d-phase flow) perpendicular to the direction of the c-phase flow to avoid any wall contact and unwanted tip-blockage. The needle was inserted through a V-shaped inlet groove into the channel to allow sealing the gap in the contact point and preventing leakage while the needle motion was not inhibited inside the channel. The needle was selected long enough compared to the oscillation amplitude (50 mm to 3 mm) to ensure vertical motion of the nozzle tip during oscillation.

The device was fabricated using the standard soft lithography method [94]. The master replication mold of the mini-channel was designed in SolidWorks 2015 (SolidWorks Co., USA)) and fabricated by a 3D-printer (Connex 3 Objet 260, Stratasys Ltd., USA) with 30 µm resolution. After positioning two tubes on the inlet and outlet reservoirs of the mold, degasified PDMS pre-polymer was poured into the replication mold and heated at 70℃ for 3 hours. The cured PDMS layer was carefully peeled off the mold. To enclose the channel, the PDMS layer was bonded to a microscope glass slide using an oxygen plasma bonding machine (Harrick Plasma, PDC-001, USA) at 45W for 30s. Post-bonding heat treatment at 70℃ for 10 minutes was performed to enhance the bonding quality. To keep the needle at the center of the channel, it was fixed inside a larger glass capillary and inserted through the V-shaped groove into the channel, from the backside of the inlet reservoir as shown in Figure 2-3c. The device was then assembled onto the experimental setup shown in Figure 2-3a, to conduct the oscillation-based jet length reduction and drop generation studies. The accuracy of needle oscillation was examined before each experiment by comparing the software input oscillation frequency with the needle tip transverse motion rate, obtained by video analysis, to make sure the needle oscillated at the desired frequency. (see Appendix A).

2.2.4 Experimental Procedure

Size and Monodispersity Studies

Experiments were executed at three d-phase (Q_d =0.05, 0.10 and 0.50 ml/min) and three c-phase (Q_c = 2, 5 and 10 ml/min) flow rates at five oscillation frequencies (f = 0, 1, 3, 7 and 15 Hz). *Ca* and *We* numbers were calculated based on Eq. 4 and Eq. 5 as summarized in Table 2-2 for different d- and c-phase flow rates.

Table 2-2. Dimensionless We and Ca numbers at different d- and c-phase flow rates.

Dispersed phase		Continuous Phase	
Q_d [ml/min]	*We*	Q_c [ml/min]	*Ca*
0.05	$10.2{\times}10^{-3}$	2	$20.4{\times}10^{-3}$
0.10	$40.8{\times}10^{-3}$	5	$51.0{\times}10^{-3}$
0.50	$1021{\times}10^{-3}$	10	$102{\times}10^{-3}$

In each set of experiments, d- and c-phase flow rates were set on the syringe pumps. At each *We-Ca* combination, first the needle was precisely located at the center of the channel and droplet generation in a stationary co-flow mode was recorded. Then, the oscillation frequency was gradually increased using the Arduino controller program and the oscillatory-mode droplet generation was studied. A high-speed video (150-400 frames per second) of the droplet generation process was recorded for further quantitative studies. The accuracy of needle oscillation was examined before each experiment by comparing the input oscillation frequency with the needle tip transverse motion rate, obtained by video analysis, to ensure the needle oscillated at the desired frequency (Appendix A).

Jet Length Reduction Studies

Experiments were executed for five oscillation frequencies (f = 0, 1, 5, 10 and 15 Hz), three d-phase (Q_d =1.8, 2.4 and 3.0 ml/min), and three c-phase (Q_c = 6, 12 and 18 ml/min) flow rates. Dimensionless *We* and *Ca* numbers calculated based on these flow rates are summarized in Table 2-3. In each set of experiments, c-phase and d-phase flow rates were set on the syringe pumps and oscillation frequency was gradually increased using the Arduino controller chip program. A high-speed video (100-350 frames per second) of the jet disintegration process was recorded to capture the whole jet and the generated droplets. The accuracy of needle oscillation was examined before each experiment by comparing the input oscillation frequency with the needle tip transverse motion rate, obtained by video analysis, to make sure the needle oscillated at the desired frequency.

Table 2-3. Summary of dimensionless We and Ca numbers at different d- and c-phase flow rates.

Dispersed phase		Continuous Phase	
Q_d [ml/min]	We	Q_c [ml/min]	Ca
1.8	13.24	6	61.1×10^{-3}
2.4	23.53	12	122×10^{-3}
3.0	36.77	18	183×10^{-3}

2.2.5 Data Analysis and Statistics

Images with the maximum jet length and repeatable patterns of multiple size droplet were extracted from the recorded videos at minimum six different time segments and analyzed by open-source image processing software, ImageJ [141]. For jet length reduction investigation, after length scale calibration, the segmented line tool was used to manually measure the length of the curved d-phase jets. The points on the segmented line were selected on the centerline of the jet from the nozzle tip up to the endpoint of the jet. For multiple droplet size assessment, after length scale calibration,

the automatic particle counting and measurement technique was used to determine the generated droplet sizes. After subtracting the background values and converting the image into grayscale (8-bit), an empirical threshold value was adopted by comparing the results of automatic edge detection technique to manually measured sizes. Droplet diameters were calculated based on the projected area assuming a spherical droplet shape. If the calculated value was determined to be larger than the channel height (H), then droplets were assumed to be cylindrical plugs rather than spherical droplets, and apparent average diameter was calculated based on volume (V) of plug as shown in Eq. 8.

$$d = \begin{cases} d_{av} & (d_{av} < H) \\ (6V/\pi)^{1/3} & (d_{av} > H) \end{cases} \tag{8}$$

Then, droplet diameters were categorized into different size groups (clusters) using the k-means clustering method in MATLAB (R2011a, The Mathworks Inc., USA). In k-means algorithm (more thoroughly discussed in Appendix B), the number of clusters and data points are the required input. The algorithm places random data points as centroids or the centers of clusters. Then it finds the nearest centroid by comparing the distances between each centroid and the data points and assigns them to that cluster. It then calculates the centroid by averaging the new cluster members and compares it with the previous value. If the error between the new and the old centroids is less than a certain value (defined by the user), the clustering is completed. However, in our case the number of clusters were not determined and in order to seek the optimal number of clusters, an intuitively heuristic approach [142] was applied. The algorithm was embedded into a loop to run the clustering process for a predefined range of k-values (number of clusters). Then, statistical variance that gives a measure of how the data distributes itself about the mean (as clustering validity index) was calculated and plotted as a function of k-value. The optimum number of clusters can be identified when the k-

value does not change upon increasing the number of clusters. After clustering, the size of droplets in each *We-Ca* condition were converted to dimensionless diameters (d/d_0) which showed the ratio of generated droplet diameter at oscillating mode to stationary mode (i.e. f=0 Hz).

All statistical analyses were performed by using Microsoft Excel (Microsoft Corp., WA, USA). Droplet sizes were reported as average of relative diameter ± SD (Standard Deviation). One-tailed unpaired Student's t-test with assumption of unequal variances was selected as the statistical method to identify any significant differences between two groups of data. Power analysis was performed to estimate the required sample sizes by maintaining the upper threshold of the significance level at 0.05 and the power at 90%.

Chapter 3

PRELIMINARY STUDIES: STATIONARY MODE CO-FLOW DROPLET GENERATION

A comprehensive study was done with the introduced device in Chapter 2, first in the stationary needle mode, to fully understand the breakup phenomena and effective parameters in standard co-flow conditions. As stated in Chapter 1, dominant forces in breakup are interfacial and drag forces which are controlled by the d- and c-phase stream flow rates (Q_d and Q_c), viscosity ratio (μ_d/μ_c), and interfacial tension of both liquids (γ_{dc}).

3.1 Effect of Flow Rates on Stationary Co-Flow Droplet Generation

The first parameter to study in droplet generation is the effect of d- and c-phase flow rates. In this set of experiments, DI water droplets dyed with methylene blue were generated in corn oil as c-phase fluid. Figure 3-1 demonstrates the results for average diameter of generated droplets at various c- and d-phase flow rates. By increasing Q_d, larger droplets were generated in constant c-phase flow rates. Conversely, by increasing Q_c, size of generated droplets decreased at constant d-phase flow rates.
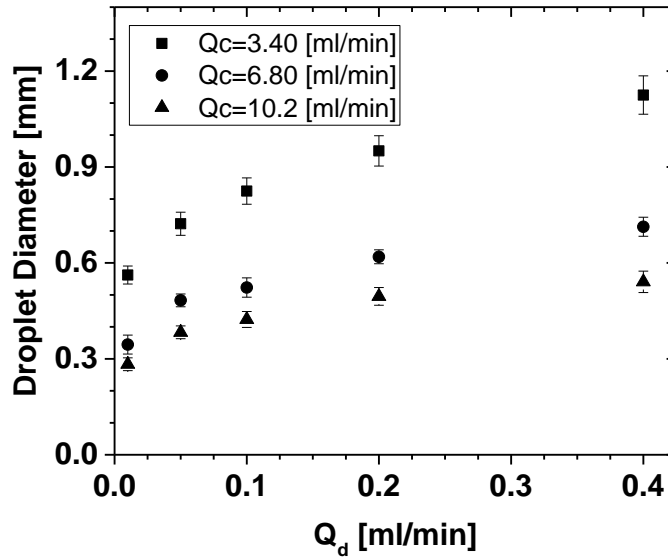
Figure 3-1. Effect of various d-phase (abscissa) and c-phase (legend) flow rates on diameter of generated droplets in the co-flow droplet generation device.

The increase in size of generated droplets upon increasing Q_d, can be attributed to the increased effect of inertia which causes more flow injection into the growing droplet. On the other hand, generation of smaller droplets at higher c-phase flow rates can be descried by the rate of drag force growth. Drag force, as previously introduced in Eq. 2, is a function of stream velocity and cross sectional area of the droplet. Therefore, at elevated c-phase velocities, a smaller cross-sectional area is sufficient to generate enough drag to overcome the interfacial force and establish breakup.

3.2 Effect of d-Phase Viscosity on Stationary Co-Flow Droplet Generation

In d-phase viscosity studies, Glycerol/Water (G/W) mixtures with different concentrations of 20% to 70% (wt/wt) were used to obtain different viscosities. Since breakup is a competition between drag and interfacial forces, it is important to keep the other parameters constant. Table 2-1,

48

summarizes the physical properties of different G/W mixtures. Reported values for surface tension of G/W mixtures at 20℃ for 20%-70% is 70.9-66.8 [mN/m], so it can be safely assumed that d-phase viscosity is the only variable parameter in this experiment. Figure 3-2 shows the effect of d-phase viscosity on droplet diameter at different G/W concentrations. Results revealed that the diameter of generated droplets increase by increasing the d-phase viscosity.
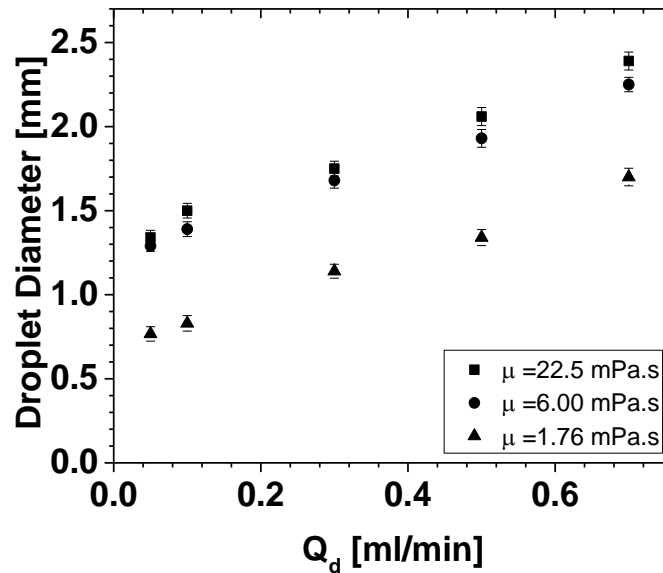
Figure 3-2. Effect of d-phase fluid viscosity on the diameter of generated droplets at Q_c=7 [ml/min] and various d-phase flow rates.

The increase in droplet diameter at elevated d-phase viscosities can be attributed to the capillary pressure which is the pressure difference between c- and d-phases. By increasing the viscosity of d-phase, the pressure drop in d-phase flow increased, therefore the d-phase exit pressure was closer to the c-phase pressure and capillary pressure was smaller. Hence, according to the inverse relation between capillary pressure and radius of curvature (Young-Laplace law), larger droplets were obtained at increased d-phase viscosities.

3.3 Effect of Nozzle Diameter on Stationary Co-Flow Droplet Generation

After studying the effect of different parameters on droplet generation from the perspective of viscous forces, we examined the effect of other parameters that play an important role on interfacial forces. In order to examine the effect of nozzle diameter, stainless steel blunt needles with different diameters (G27: ID=0.203mm, OD=0.406mm and G23: ID=0.432mm, OD=0.635mm) were used as dispensing nozzle in our experiments. Experiments were performed at different d-phase flow rates and results are shown in Figure 3-3a and Figure 3-3b for Q_c = 1 [ml/min] and Q_c = 2 [ml/min], respectively.
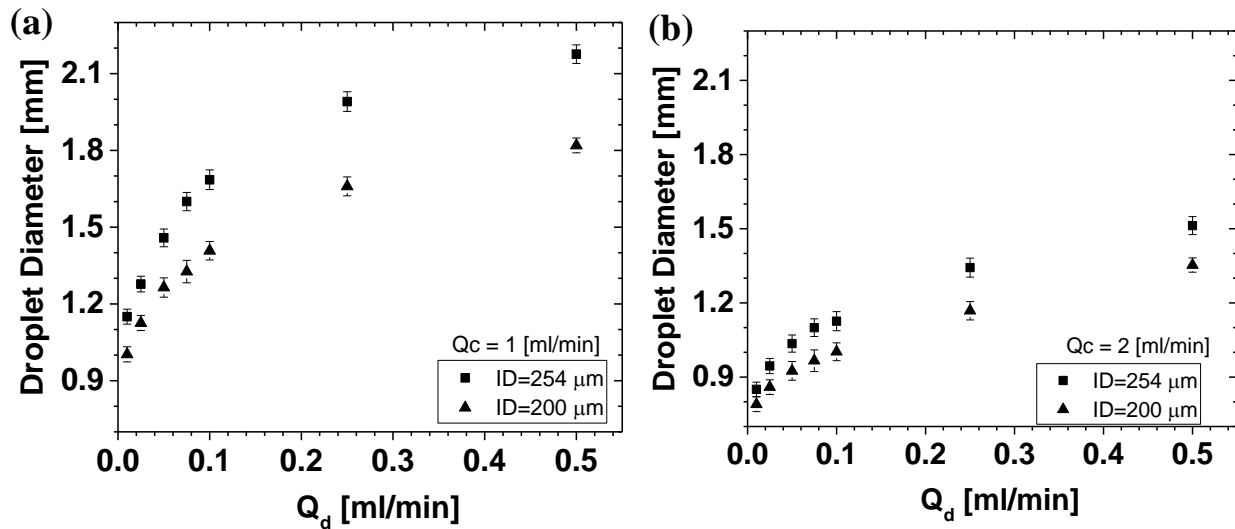
Figure 3-3. Effect of nozzle diameter (legend) on the size of generated droplets at various d-phase flow rates at two different c-phase flow rates of (a) Q_c=1 [ml/min] and (b) Q_c=2 [ml/min].

As expected, a decrease in the size of generated droplets was observed upon increasing the c-phase flow rate. However, in both conditions generated droplets with the larger nozzle were larger than the small nozzle. This observation can be attributed to the fact that interfacial force (introduced in

50

Eq. 1) is a function of nozzle diameter and upon increasing the nozzle size, interfacial force holding onto the growing interface increased and a larger drag force was required to establish the force balance and detach the droplet. Since flow rates are constant, in order to achieve larger drag forces, droplets must grow larger to attain higher cross-sectional areas.

3.4 Effect of Surface Tension on Stationary Co-Flow Droplet Generation

Ethanol/Water (E/W) mixtures with different weight ratios were prepared to obtain different surface tensions. As stated in Eq. 1, surface tension is an effective parameter on interfacial force. Experiments were performed with various concentrations of E/W at different d-phase flow rates and results are shown in Figure 3-4a and Figure 3-4b for $Q_c = 1$ [ml/min] and $Q_c = 2$ [ml/min], respectively.
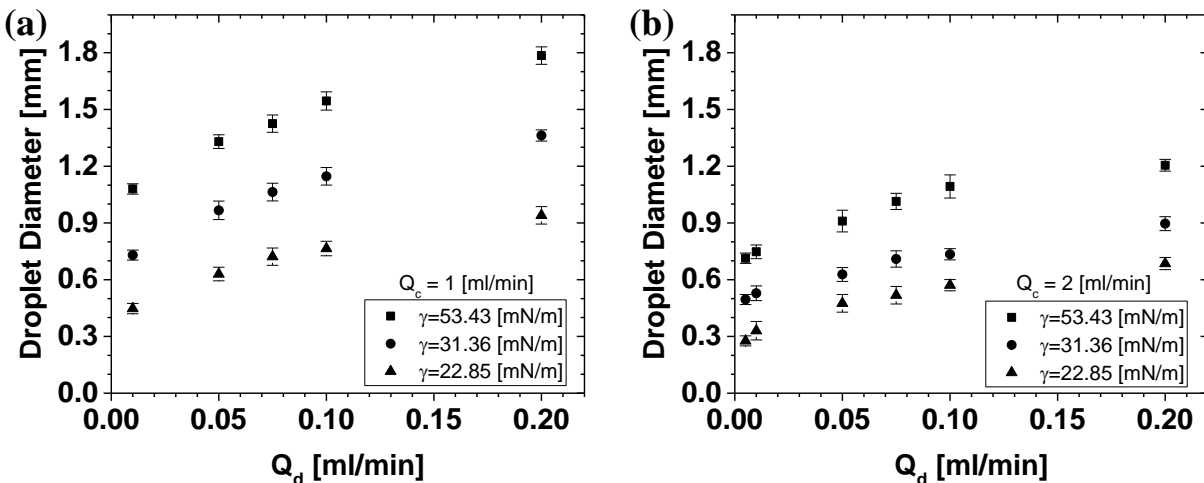
Figure 3-4. Effect of interfacial tension (legend) on the size of generated droplets at various d-phase flow rates at two different c-phase flow rates of (a) $Q_c=1$ [ml/min] and (b) $Q_c=2$ [ml/min].

51

As expected, results revealed a decrease in the size of generated droplets at increased c-phase flow rates. However, in both conditions by increasing the ethanol concentration, the size of generated droplets decreased. This observation can be explained by the interfacial force introduced in Eq. 1 which is a function of interfacial tension. At constant flow rate conditions, by increasing the concentration of ethanol, interfacial force which resisted droplet breakup decreased and droplets became smaller.

3.5 Conclusion

We tested our oscillating d-phase droplet generation device in the stationary mode to verify the proper performance of our system. The experimental results in this section demonstrated that the device operated similar to what has been reported in the literature parametrically. As reported in the literature [54, 81, 92] diameter of generated droplets were directly proportional to interfacial tension, nozzle diameter, d-phase flow rate and d-phase viscosity and inversely proportional to c-phase flow rate. This provided the basis for our oscillation-based experiments in the next two chapters.

Chapter 4

SIZE AND MONODISPERSITY IN OSCILATING DISPERSED-PHASE CO-FLOW DROPLET GENERATION

This chapter presents the application of oscillatory nozzle technique for multi-size, monodisperse droplet generation in a conventional co-flow geometry. As stated in Chapter 2, the dispersion nozzle is oscillated inside the c-phase fluid channel to generate a drag force gradient in this method. Upon oscillation, the nozzle repositions across the width of the channel with different streamlines experiencing different drag rates at each lateral position. In addition to this axial drag gradient, nozzle oscillation in the transverse direction to the c-phase flow creates a transverse drag induced by the relative velocity of flow and needle's tip. The combined effects of the axial and transverse drag forces counter-reacting the interfacial forces lead to generation of multi-sized droplets with a wide range of sizes. The effect of c- and d-phase fluid flow rates and needle oscillation frequency on the size and number of generated droplets is investigated in this chapter. We believe this novel technique will assist researchers in applications requiring multi-size monodispersed droplets such as target encapsulation in low-concentration samples, which requires size optimization as discussed in Chapter 1.

4.1 Effect of Frequency on Oscillating Co-Flow Droplet Generation

It is well understood that c- and d-phase flow rates, respectively represented by *Ca* and *We* numbers, are two important parameters in co-flow droplet generation systems. We first verified the correct performance of our system (Figure 4-1) in the stationary d-phase nozzle mode (i.e. f=0

Hz). The c- and d-phase flow rates in the ranges of 2-10 ml/min and 0.05-0.50 ml/min were used, respectively, and real-time images of the generated droplets were acquired under the lens-equipped high speed camera (Figure 4-1a). The average droplet diameters in the stationary mode were then calculated at various *Ca-We* conditions (Table 2-2), as shown in Figure 4-1b. As expected, upon increasing the *We* number and due to the increased level of inertial forces, more d-phase liquid was injected into the growing droplet before the interfacial instabilities managed to disintegrate the interface. Therefore, droplets grew larger as the *We* number was increased. On the contrary, increasing the *Ca* number elevated the axial viscous drag force that counteracted the droplet growth and subsequently yielded a reduction in the size of droplets. Coefficients of variance were calculated to be CV<0.4% for all flow rates at the stationary mode.
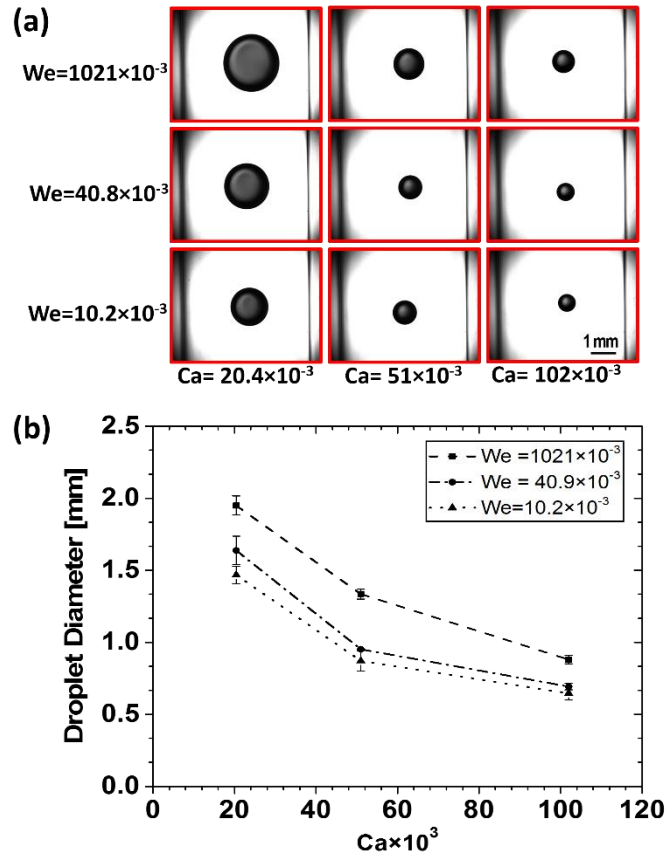
Figure 4-1.Stationary mode (f=0 Hz) co-flow droplet generation. (a) Images of droplets generated at various We-Ca conditions. (b) Effect of We and Ca numbers on the droplet size in the stationary mode. Droplet size was directly proportional to the d-phase flow rate (We) and inversely proportional to the c-phase flow rate (Ca).

After establishing the stationary-mode framework for our system, the effects of nozzle oscillation and its frequency on water-in-oil droplet generation at different c- and d-phase flow rates were examined. Representing experimental images of droplets and their dimensionless diameters at different oscillation frequencies, when the lowest *We= 10.2×10⁻³* and *Ca=20.4×10⁻³* were used, are shown in Figure 4-2a and Figure 4-2b, respectively. The effects of nozzle oscillation on the number of generated droplets and their sizes are clearly observed in this figure.
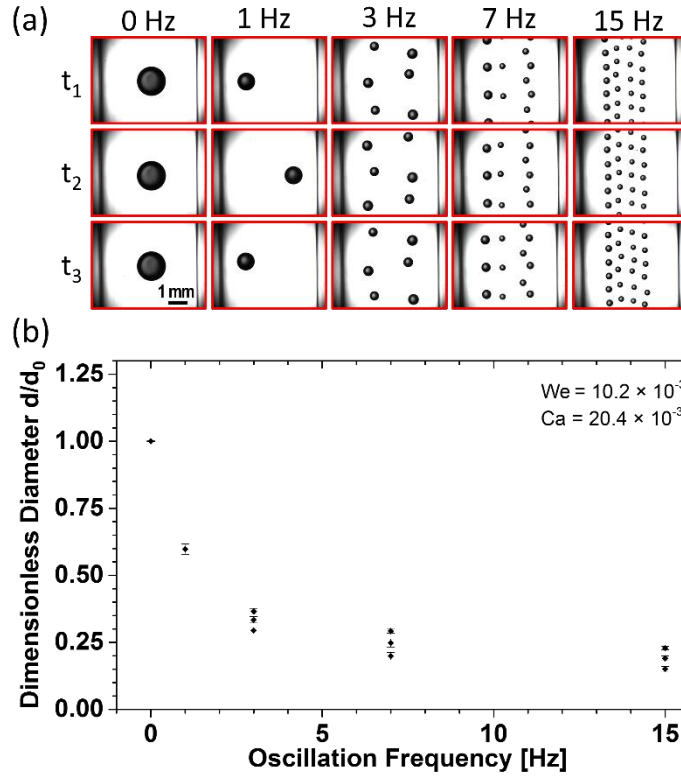
Figure 4-2. Oscillatory mode (f=0-15 Hz) co-flow droplet generation at the lowest flow rate levels with We=10.2×10^{-3} and Ca=20.4×10^{-3}. (a) Droplet images at different oscillation frequencies with repeatable patterns. (b) Effect of oscillation frequency on the number of generated droplets and their dimensionless diameter (d/do). Upon increasing the oscillation frequency, transverse drag increased and subsequently led to an overall droplet size reduction. Meanwhile, the lateral motion of the nozzle exposed the growing droplet to a variable axial drag and droplet breakup occurred at different sizes at different locations.

We used our clustering method, described in Appendix B, to identify the number of independent droplet sizes in the experiments above. As shown in Figure 4-2a and Figure 4-2b, by increasing the oscillation frequency, the number of generated droplets increased from one set at 0 and 1 Hz to three statistically independent sizes (one-tailed unequal variance t-test, p-values < 0.001) at the frequencies of 3, 7 and 15 Hz. Moreover, the average droplet size decreased by 84.9% of the stationary droplet size as the oscillation frequency was increased to 15 Hz. The coefficients of variance were calculated to be 0.22% < CV < 2.34% for all oscillation frequencies at these flow rates.

The overall effect of oscillation frequency on the number and dimensionless diameter of generated droplets at different *We-Ca* conditions of Table 2-2 can be found in Appendix C. The general trends were similar in all conditions, but generation of some droplet clusters that were slightly larger than the stationary mode droplets were observed at the high *We-Ca* levels. In these conditions, at the initial stages of oscillation and regardless of the additional transverse drag effect, the dimensionless size of generated droplets increased with frequency. However, by further increase in the oscillation frequency, the dimensionless size dropped below unity for all *We-Ca* conditions.

4.2 Effect of d-phase Flow Rate on Oscillating Co-Flow Droplet Generation

To study the effect of d-phase flow rate on the number of generated droplets and their corresponding dimensionless diameters in our system, we conducted a series of experiments similar to previous the section. Dimensionless droplet sizes obtained at various *We* numbers of 10.2×10^{-3}, 40.8×10^{-3} and 1021×10^{-3} and a constant *Ca* number of 20.4×10^{-3} for different oscillation frequencies are shown in Figure 4-3.
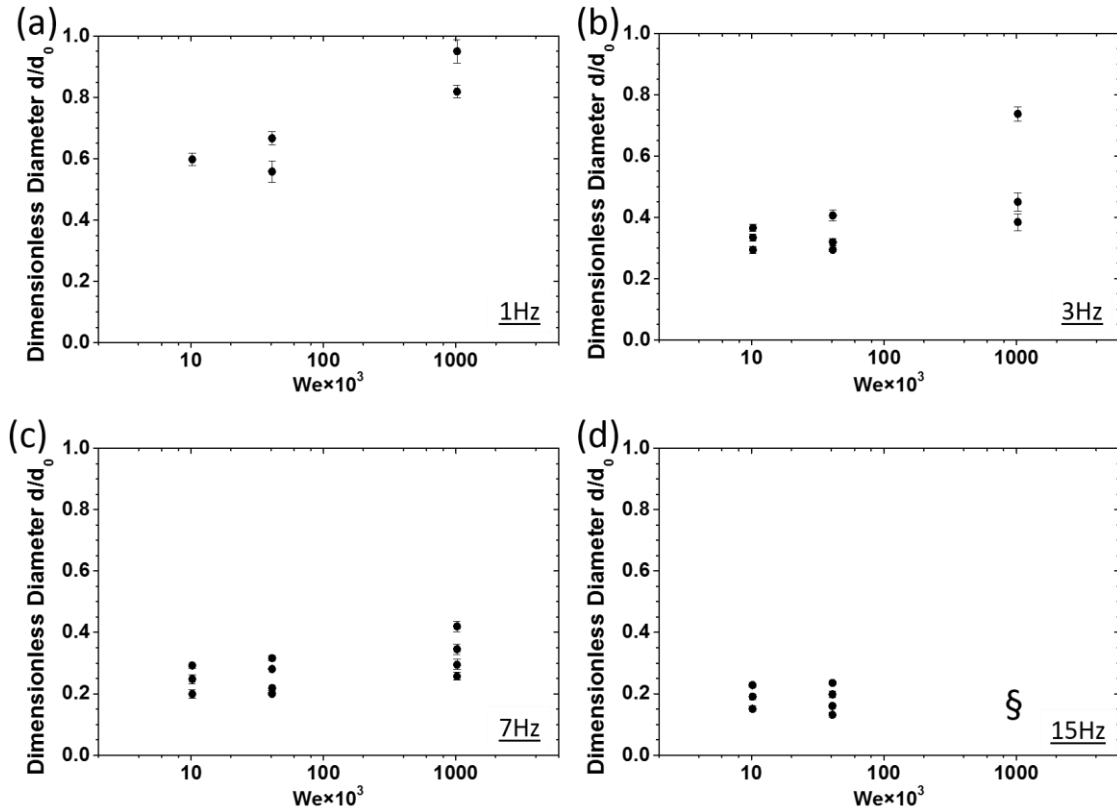
Figure 4-3. Effect of d-phase flow rate (We number) on dimensionless size and number of generated droplets at a constant c-phase flow rate (Ca=20.4×10⁻³) and at various oscillation frequencies of (a) 1 Hz, (b) 3 Hz, (c) 7 Hz, and (d) 15 Hz. The symbol § in (d) indicates a condition under which the generated droplets overlapped due to increased throughput and image processing-based edge detection and size assessment were not feasible.

As shown in Figure 4-3, by increasing the oscillation frequency droplet sizes decreased as discussed earlier in the previous section. Moreover, at each oscillation frequency, increasing the *We* number led to elevated number of generated droplets with an overall increase in their sizes. At f=1Hz, the size of generated droplets were closer to the sizes obtained in the stationary mode. By increasing the oscillation frequency, a reduction trend in dimensionless droplet size was observed and at the highest oscillation frequency of f=15Hz, the size of generated droplets were almost independent of the *We* number. The coefficients of variance were calculated to be $0.22\% < \text{CV} < 4.6\%$ for all oscillation frequencies at various *We* numbers.

4.3 Effect of c-phase Flow Rate on Oscillating Co-Flow Droplet Generation

As stated earlier, *Ca* number which shows the ratio of viscous to interfacial forces is a representative for the c-phase flow rate. Dimensionless diameters of water-in-oil droplets at various *Ca* numbers of 20.48×10^{-3}, 51.0×10^{-3} and 102×10^{-3} and a constant *We* number of 10.2×10^{-3} for different oscillation frequencies are shown in Figure 4-4.
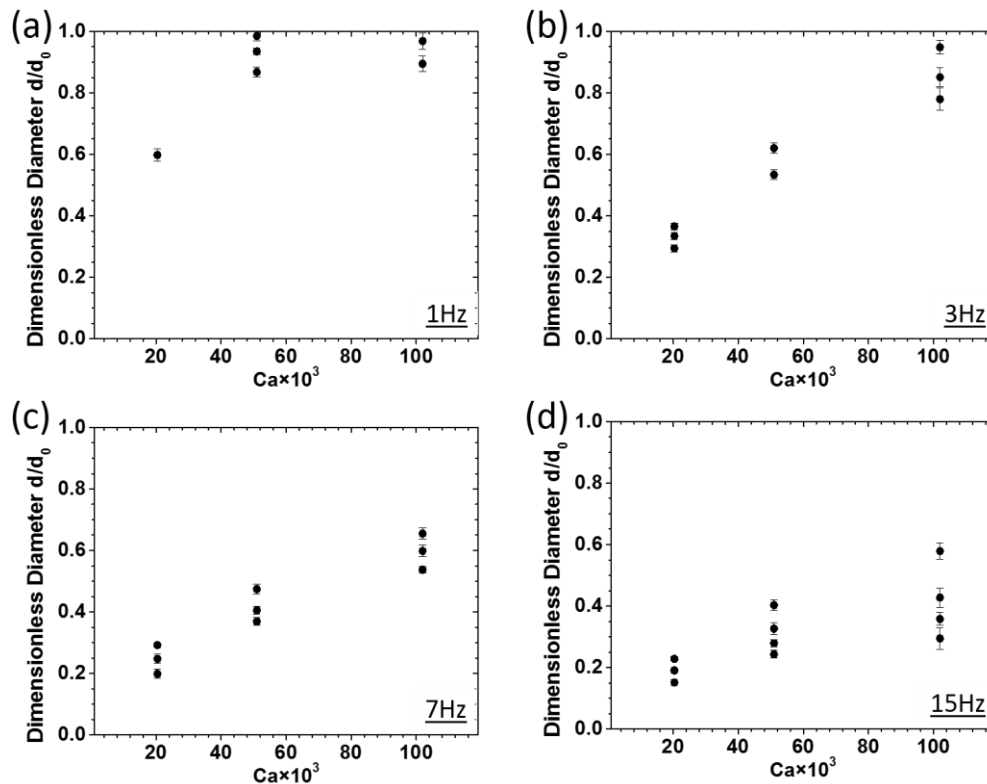
Figure 4-4. Effect of c-phase flow rate (Ca number) on dimensionless size and number of generated droplets at a constant d-phase flow rate (We=10.2×10^{-3}) and at various oscillation frequencies of (a) 1 Hz, (b) 3 Hz, (c) 7 Hz, and (d) 15 Hz.

Our results revealed increasing trends in the number of generated droplets and their dimensionless diameters upon increasing the *Ca* number at fixed oscillation frequencies. Moreover, increasing

the oscillation frequency yielded an overall decrease in droplet sizes as mentioned earlier in previous sections. At f=1Hz where transverse drag is not significant, the generated droplets at high c-phase flow rates become similar in size and almost equal to the stationary droplets. By increasing the oscillation frequency to f=3Hz and beyond, transverse drag also became significant and dimensionless diameter of droplets decreased with frequency and increased with *Ca* number consistently. The coefficients of variance were calculated to be 0.19% < CV < 3.27% for all oscillation frequencies at various *Ca* numbers.

4.4 Discussions

As shown in Figure 4-2, the transverse oscillation of the d-phase needle inside the channel, perpendicular to the c-phase stream, had two important effects on the droplets. Most importantly, an extra lateral drag was added to the existing axial drag, assisting the breakup to happen at smaller droplet diameters. Accordingly, by increasing the oscillation frequency, the lateral drag force was intensified and the overall sizes of generated droplets decreased. Moreover, the transverse motion also exposed the growing droplets to a varying axial drag due to the parabolic profile of the c-phase flow velocity and the varying rate of deformation across the width of the channel. Altogether, we observed that the oscillatory motion of the d-phase fluid leads to droplet breakup at different lateral locations in the channel and a frequency-dependent generation of multiple droplets with general decrease in diameter (see Appendix C for more supporting data).

The increase in the number of generated droplets at higher *We* numbers in Figure 4-2 can be attributed to the situation where the total drag force (i.e. axial and transverse drag) equates the interfacial force during oscillation. The axial drag force varies with lateral displacement of the d-

phase nozzle and also the size of the growing droplet. The transverse drag force is relatively constant at a constant oscillation frequency and only increases upon droplet growth. When the *We* number is increased, droplet growth happens faster at a constant frequency and *Ca* number. Therefore, droplets reach their breakup diameters faster and droplet generation happens more often at higher *We* levels, leading to generation of more clusters of droplets.

The overall droplet size increase at higher *We* levels in Figure 4-3 can be described by the increased inertial effects that were also discussed for the stationary droplets. As shown in Figure 4-3 (a-c), at lower oscillation frequencies where inertial effect was dominant, increase in the *We* number resulted in a dominant increase in the dimensionless droplet sizes. However, by increasing the frequency, the effect of total drag force became dominant over the inertial effects and as shown in Figure 4-3d, the generated droplets were approximately the same size at various *We* numbers.

An increase in the axial drag force at the same lateral positions in the channel was predicted upon increasing the *Ca* number. Therefore, droplet breakup was expected to occur at smaller sizes. As shown in Figure 4-4, the dimensionless diameter of droplets increased by increasing the *Ca* number, which may seem controversial. However, by referring to the actual droplet diameters, we observed that the droplets generated at higher *Ca* numbers were indeed smaller. Due to the dominance of axial drag forces at high *Ca* numbers, the transverse drag effect was not significant and the size of generated droplets were closer to the stationary mode, which led to larger dimensionless droplet diameters at higher *Ca* numbers. Increasing trends in the dimensionless droplet size at higher *We* number levels were also observed upon increasing the *Ca* number as shown in Appendix C.

In the stationary mode, where needle is centered in the channel, axial and transverse drags are at their maximum and minimum (zero) levels, respectively. In the low *We-Ca* oscillating modes, due

to the dominant impact of the transverse drag, the size of generated droplets were always equal to or smaller than the droplets in the pure axial drag mode (i.e. stationary mode). Interestingly, at elevated *We-Ca* conditions, upon increasing the oscillation frequency, an atypical behavior was observed. Generation of oscillatory-mode droplets larger than their stationary-mode counterparts at higher *We-Ca* conditions can be attributed to the counteraction of the total drag force components (axial and transverse drag), in the presence of increased levels of inertia. At lower oscillation frequencies where transverse drag was insignificant, due to higher injection rates, dimensionless sizes of generated droplets were larger than unity at increased *Ca* levels. However, by increasing the oscillation frequency, transverse drag became significant and consequently, dimensionless diameters at higher injection rates dropped below unity in all flow conditions.

4.5 Conclusion

The effects of oscillating d-phase nozzle on the number of droplets and their sizes were investigated in a co-flow device at different flow rates and oscillation frequencies. First, performance of the system in the stationary d-phase nozzle mode (i.e. f=0 Hz) was investigated to establish the framework for nozzle oscillation studies. Then, effect of oscillation-induced drag force gradient on the size of generated droplets was studied at different frequencies (f=1-15 Hz). Unlike other conventional passive methods, the oscillating d-phase nozzle technique was able to simultaneously produce a wide range of monodispersed droplets (4 nL up to 4 μL) at constant c- and d-phase flow rates with no modification in the physical properties of liquids. Droplet sizes were directly proportional to the *We* number and inversely proportional to the *Ca* number and oscillation frequency. Increasing any of the parameters yielded a general increase in the number of breakup points. Increasing oscillation frequencies, lead into a general decrease in sizes of

generated droplet due to dominant effect of the transverse drag compared to the stationary mode. Upon increasing *We* number, due to the higher injection rate of d-phase fluid, a general increase in the size of droplets and number of breakup points was observed. By increasing the *Ca* number, the effect of axial drag became dominant over transverse drag. Thus, droplets were generated in smaller sizes but not very distant from stationery mode (pure axial drag) therefore an increase in dimensionless size of droplets was observed upon increasing *Ca* number. For increased *Ca* numbers, axial drag variation was significant and at lower oscillation frequencies where transverse drag was not sufficiently large to compensate for axial drag reduction and the generated droplets became even larger than the stationary droplets. However, upon increasing the oscillation frequency, the transverse drag intensified and the size of generated droplets dropped below the reference stationary sizes. This yielded to a decrease in the size of generated droplets however they were not distant from each other. This method can generate repeatable patterns of droplets with different sizes that can be used in target encapsulation applications in low-concentration samples, where size optimization processes are required. Furthermore, additional oscillation-induced drag forces can facilitate droplet breakup in applications that require higher shear rates.

Chapter 5

JET LENGTH REDUCTION IN OSCILATING DISPERSED-PHASE CO-FLOW DROPLET GENERATION

As stated in Chapter 1, microdroplet generation methods are assessed by two important criteria: droplet throughput and size dispersity. The widely used co-flow droplet generation technique is bottlenecked with droplet polydispersity at high throughputs due to transition to the instable jetting regime at high d-phase flow rates. In this chapter, by oscillating a water-based d-phase fluid perpendicular to the direction of an oil-based c-phase fluid flowing in a channel, an additional transverse drag is introduced into a co-flow droplet generation system. The axial and transverse drag forces resist droplet growth and affect the jet length and the generated droplets. The effect of d-phase viscosity and oscillation frequency on jet length reduction was studied at different d- and c-phase flow rates. The transverse motion of dispersion nozzle effectively decreased the jet length followed by increasing the throughput of droplet generation. We also showed the application of our technique in jet disintegration and droplet generation for ultra-low interfacial tension systems in which stable jets form and droplet generation is not an easy task.

5.1 Water-in-Oil Jetting under Oscillating Needle Condition

Co-flow water-in-oil droplet generation, in a static d-phase mode, is a result of competition among the c-phase oil axial shear and the d-phase water surface tension forces. Due to the wall effects on

the velocity profile of the c-phase fluid, oscillation of the d-phase nozzle in our device exposes the jet to a variable axial drag gradient along the width of the channel. In addition, a lateral shear force will also emerge due to the transverse oscillatory movement of the needle which adds up to the axial shear. We were interested in investigating whether the oscillatory motion of the d-phase flow can result in changing the jet length in our co-flow device. Figure 5-1a and Figure 5-1b respectively show sequential images of dyed water jet in oil and corresponding jet length data at different oscillation frequencies, when $We=13.24$ and $Ca=183\times10^{-3}$.
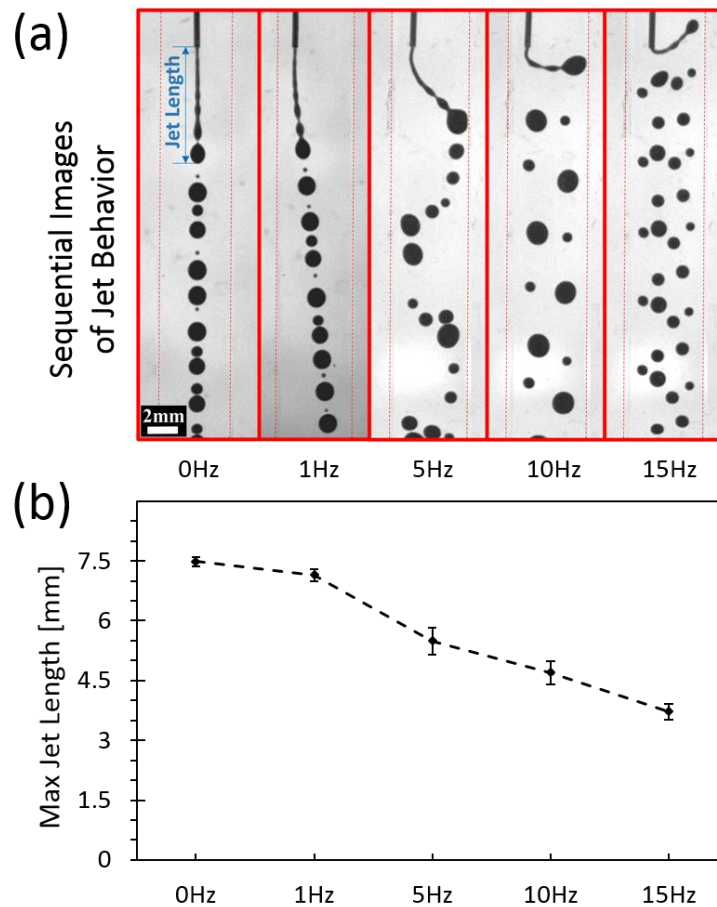
Figure 5-1. Effect of nozzle oscillation on jet disintegration and length reduction as well as co-flow droplet generation at $We=13.24$ and $Ca=183\times10^{-3}$. (a) Sequential images of jet behavior and generated droplets at different oscillation frequencies. Increasing the frequency from 1 Hz to 15 Hz resulted in shortening the jet and production of more droplets with various diameters. (b) Maximum jet length at different oscillation frequencies showing a reducing trend as the frequency was increased.

65

By oscillating the nozzle, the jet experienced a shear gradient in the transverse direction and disintegrated faster into droplets. As shown in Figure 5-1a and Figure 5-1b, increasing the oscillation frequency from 1 Hz to 15 Hz resulted in shortening the jet length from 7.48±0.11 mm to 3.71±0.19 mm. The effect of oscillation on jet length reduction is further investigated in the next section.

5.2 Effect of Oscillation on Jet Length at Different d- and c-Phase Flow Rates

The effect of nozzle oscillation on water-in-oil jets with different *We* and *Ca* numbers was examined. Due to the transverse motion at various frequencies, a modulated extra shear force was imposed on the jet and a jet length reduction was observed by oscillating the d-phase discharging nozzle. Figure 5-2 shows the experimental results for the measured jet lengths at different c- and d-phase flow conditions. As a representative example, the results for pure water in oil at Q_c=6 ml/min and Q_d=1.8 ml/min (*We*=13.24 and *Ca*=61.2×10^{-3}) at different oscillation frequencies are shown in Figure 5-2a by a dashed line. At the stationary mode, the jet length was measured to be 9.39±0.21 mm and by increasing the oscillation frequency up to 5Hz, the jet length rapidly shrank down to 4.81±0.30 mm. The effect of oscillation frequency became less dominant beyond this point and the final jet length obtained was 3.74±0.3 mm at the highest frequency (15 Hz). By increasing the d-phase flow rate at each frequency, we observed a general increase in the jet length. The above trends were repeated similarly in experiments with other d-phase and c-phase flow rates as shown in Figure 5-2b and Figure 5-2c.

66
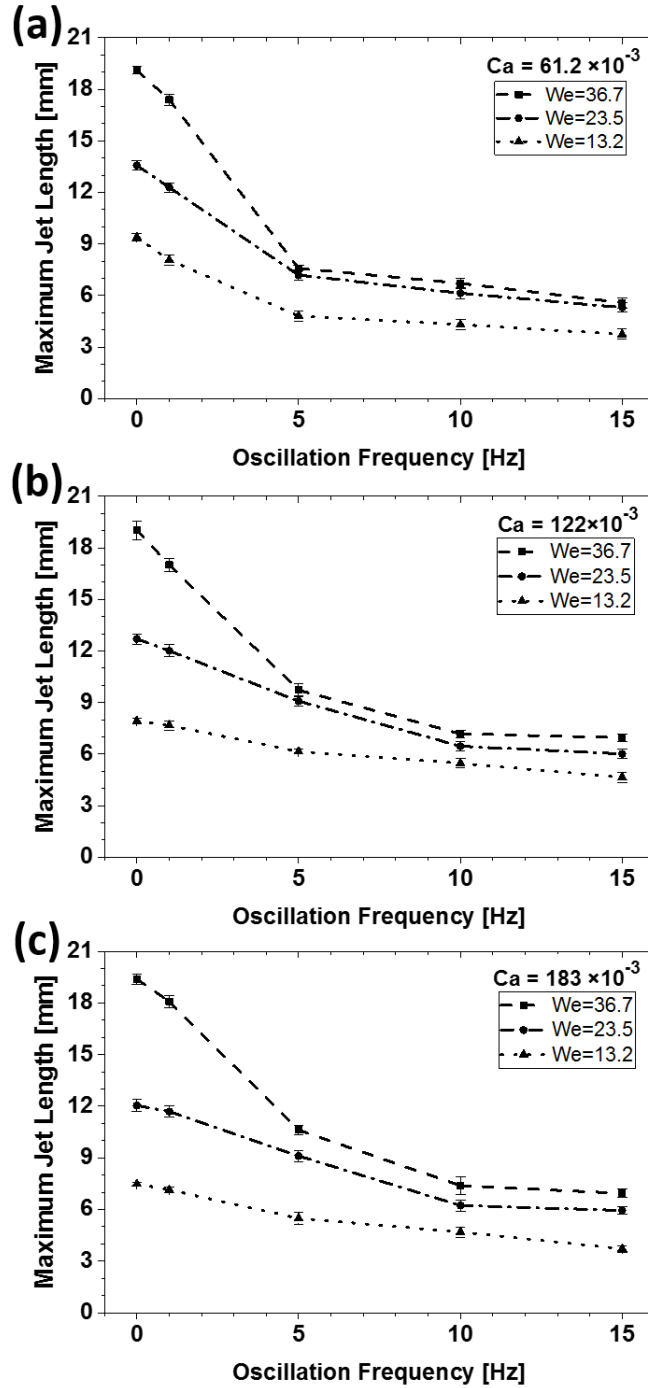
Figure 5-2. Effect of d-phase needle oscillation frequency on the maximum jet length of water-in-oil at various We (legend) and Ca (a-c) numbers. Stationary jet length was directly proportional to the d-phase flow rate (We) and inversely affected by the c-phase flow rate (Ca). At constant c- and d-phase flow rates, more rapid oscillation of the needle resulted in reduction of the jet length due to enhanced transverse shear. The frequency-dependent jet length reduction effect was more dominant at higher d-phase flow rates. Jet length reduction occurred with higher slopes at initial oscillation frequencies and gradually diminished at elevated oscillation rates.

The stationary jets were expected to have different lengths at various d- and c-phase flow rates. When no oscillation was introduced into the system as shown in Appendix D, resulted in elevation of inertial injection of water into the jet and a consequent increasing effect on the jet length. Increasing the *Ca* number adversely affected the jet length at lower We numbers while having no effect on the jet length at the highest *We* numbers (unpaired t-test, p-value<0.005 was considered significant). Our results in the stationary mode matched with the literature confirming that our system could be used for d-phase oscillation investigations below.

By exposing the jet to the transverse motion, the most common behavior observed in all pure water in oil studies was the jet length reduction upon increasing the oscillation frequency. At each constant *We-Ca* condition, as transverse shear increased with frequency, the jet length subsequently became shorter. However, this frequency-dependent jet length reduction behavior occurred with different slopes at different flow conditions.

At low-to-medium *We* and middle-to-high *Ca* numbers, increasing the oscillation frequency resulted in a consistent reduction of the jet length with an almost constant rate. However, as the *We* number was increased, the effect of frequency became more dominant at slower oscillation rates. For instance, at high *We* numbers, at 1-5 Hz frequencies at low and middle *Ca* and 1-10 Hz frequencies at the high *Ca*, the effect of frequency on jet length reduction was strong while at higher frequencies, the rate of jet length reduction became relatively smaller (Appendix D). This change of rate of reduction in jet length can be attributed to the length of the jet at previous stages (lower frequency) in each case. At high oscillation frequencies, jets are normally smaller and hence more stable, so a significantly higher shear is required for jet perturbation. Further studies with more flow rate and oscillation frequency levels are needed to better understand the frequency-dependent behavior of oscillating jets.

Overall, a maximum jet length reduction of 70.8% with respect to the stationary mode was obtained at We=36.78 and Ca=61.2×10^{-3} when the needle was oscillated at 15 Hz frequency. At this flow rate condition, the jet length at stationary mode was measured to be 19.11±0.21 mm which dropped down to 5.58±0.29 mm at the oscillation frequency of 15 Hz.

5.3 Effect of Oscillation on Jet Length at Different d-phase Fluid Viscosities

Glycerol in water (G/W) mixtures with different concentrations were used to examine the effect of oscillation frequency on jet length reduction with different d-phase viscosities. The jet length results for We=13.24 and Ca=183×10^{-3} with three different jet viscosities of μ=1 mPa.s (0% wt. G/W), μ=2.5 mPa.s (30% wt. G/W) and μ=6 mPa.s (50% wt. G/W) are shown in Figure 5-3(a-c). The jet length in the stationary mode was inversely proportional to the viscosity of the d-phase fluid and this result was in good agreement with the literature[143]. By elevating the oscillation frequency in the low viscous fluid (μ=1 mPa.s), the jet length reduced continuously to 50.4% of the initial length. The results for jet with mid-viscous fluid (μ=2.5 mPa.s) represented a multi-stage behavior. By increasing the oscillation frequency, the jet length slightly increased and plateaued (0-5Hz) and then started to decrease at higher frequencies (beyond 5Hz). For the high viscous jet (μ=6 mPa.s), the jet length slightly increased at initial stages of oscillation and then became independent of the oscillation frequency (unpaired t-test, a p-value<0.005 was considered significant). Viscosity is a measure of fluid resistance against gradual deformation by shear stress, and during oscillation, the jet with higher viscosity shows more resistance against deformation.

Therefore, at lower oscillation rates where the transverse shear is small, the jet stretches due to viscous effects. Instabilities are not intense enough to rupture the jet interface and consequently the average length increases slightly for highly viscous fluids. At higher oscillation rates, the transverse shear increases and jet stretching provoked by high viscosity is counteracted by length reduction associated with oscillation. If the viscosity effect is dominant, the stretch and contraction cancel each other, and the jet length becomes unimpeded by the transverse motion. If the transverse shear overcomes the viscosity effect, the jet starts to shrink down. Thus, for mid-viscous jet at lower oscillation rates, where viscosity effects were dominant, the jet length slightly increased and by increasing the frequency, the transverse motion became more effective and the jet length commenced to reduce beyond 5Hz. But in high-viscous fluid, where viscous stretch was comparable to transverse-motion-induced reduction, the jet length was independent of the oscillation frequency at the higher rates.
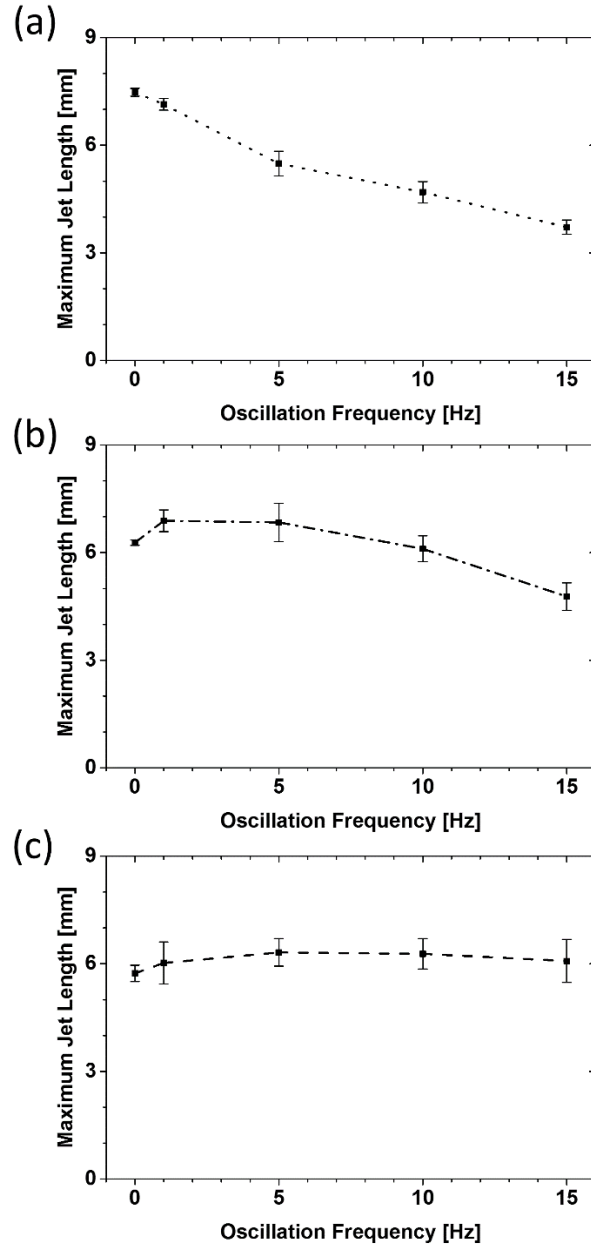
Figure 5-3. Effect of d-phase needle oscillation frequency on the maximum jet length with different d-phase fluid viscosities while We=13.24 and Ca=183×10⁻³. (a) The jet length decreased by increasing the oscillation rate for low viscous (μ=1 mPa.s) d-phase fluid. (b) Mid-viscous jet (μ=2.5 mPa.s) showed an intermediary behavior, i.e. by increasing the oscillation frequency (1 Hz) the jet length increased then remains constant (1-5 Hz) and then (beyond 5 Hz) reduced like a low-viscous jet (c) High-viscous (μ=6 mPa.s) jet length increased slightly and reached a plateau at high frequencies. (These effects were statistically confirmed).

71

5.4 Effect of Oscillation on Jet Disintegration in Aqueous Two Phase Solutions (ATPS)

We also examined the effect of oscillation on jet breakup and droplet generation in Aqueous Two Phase Solutions (ATPS) as introduced in Chapter 2. ATPS, a bio-friendly and ecofriendly aqueous biphasic system, have been drawing a significant attention in the microfluidics droplet community lately[144], mainly due to the enormous protein separation and extraction [145, 146], cell partitioning [147, 148], bacterial and cell micro-patterning [149, 150] and DNA extraction [151, 152]. Aqueous media is a crucial requirement in most of the culturing and pattering applications of biological targets. Generating aqueous compartments of bio-samples inside another immiscible aqueous media is beneficiary in generating artificial cells studies. In ATPS systems, the interfacial tension between the d- and c-phase fluids is drastically low, which results in increased Capillary numbers and transition to jetting regime. Interfacial instabilities (the key point in interface breakup) are damped in ultra-low interfacial systems leading to formation of stable jets rather than droplets in conventional droplet generation techniques. Thus, we believe our technique t will facilitate the droplet generation in these systems by taking advantage of the additional transverse drag force.

The ATPS biphasic system used in our experiments consisted of Polyethylene Glycol (PEG)-rich solution as c-phase and Dextran (DEX)-rich solution as d-phase liquid. A borosilicate glass capillary with inner diameter of ID = 135μm was glued to the steel needle to reduce the nozzle diameter because preliminary experiments with larger-diameter nozzles resulted in stable jets that could not be affected with the oscillation motion. Figure 5-4 demonstrates the observed proof-of-principle results of jet disintegration into droplets upon nozzle oscillation in an ATPS biphasic

system. DEX as d-phase was injected at $Q_d = 0.03$ml/hr into PEG as c-phase fluid flowing at $Q_c = 2$ml/min.
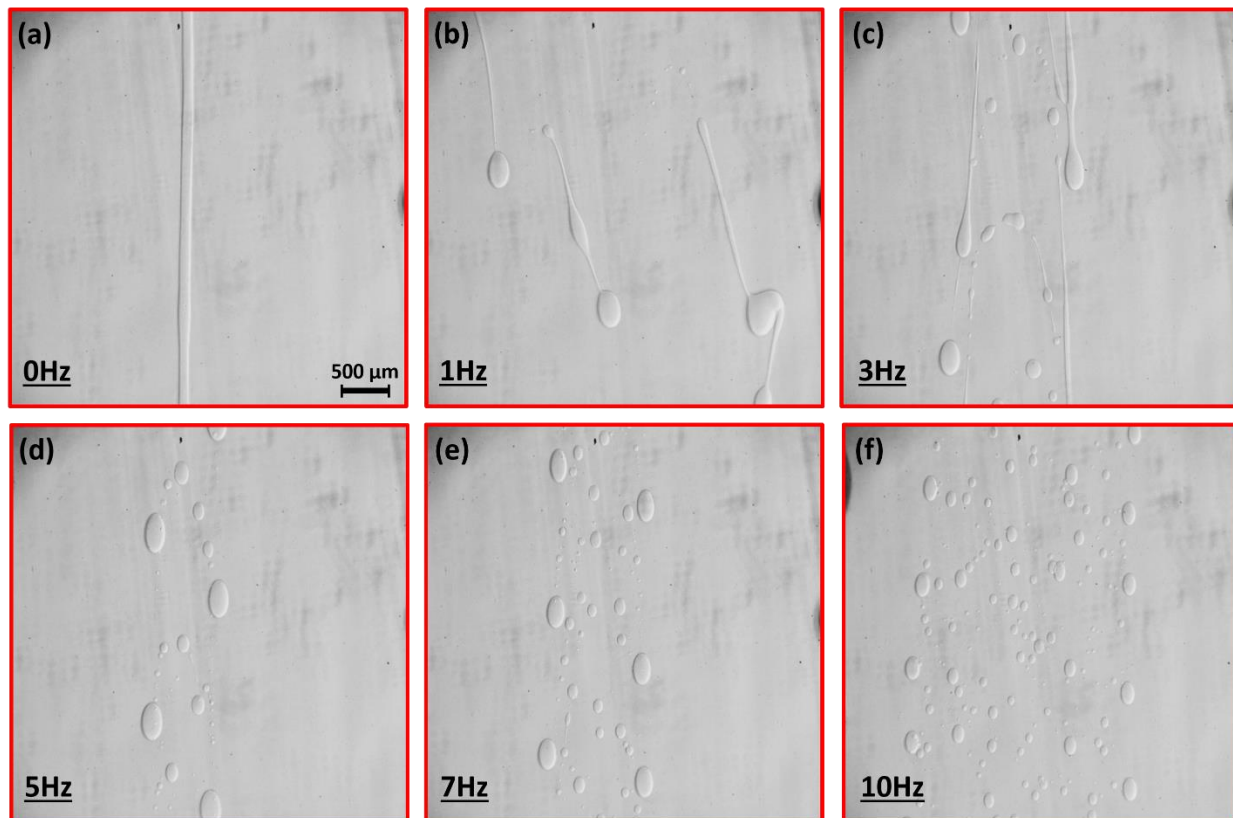
Figure 5-4. Effect of nozzle oscillation on jet disintegration and droplet generation in (PEG-DEX) ATPS system. Sequential images of jet behavior and generated droplets are shown at (a) 0Hz e.g, conventional co-flow, (b) 1Hz, (c) 3Hz, (d) 5Hz, (e) 7Hz and (f) 10 Hz oscillation frequency. Flow is from top to bottom with DEX as d-phase injected at $Q_d = 0.03$ml/hr into PEG as c-phase fluid flowing at $Q_c = 2$ml/min.

Due to inherently ultra-low interfacial tension of the system, as show in Figure 5-4a, a stable jet of DEX was formed inside PEG at the stationary mode condition. However, upon oscillation, the stable jet started to disintegrate into shorter floating threads of the d-phase liquid (as shown in Figure 5-4b and c). By increasing the oscillation frequency as illustrated in Figure 5-4 d-f, the floating jets diminished and droplets with a decreasing size trend with frequency started to be generated. This proof-of-concept study demonstrated the usefulness of our system in generating droplets in ATPS, where achieving droplets has been shown to be a very challenging task.

73

5.5 Conclusion

Triplet experiments were executed for jets at different flow rates (*We-Ca* numbers) and oscillation frequencies and the effect of transverse motion and viscosity on jet length reduction was studied. Jet breakup in the stationary mode resulted in generation of satellite droplets in various sizes alongside the main droplets. Our results revealed that increasing the d-phase flow rate (*We* number) will lead to elevation of jet length at constant c-phase flow rates (*Ca* number), while increasing the *Ca* number inversely affected the jet length. Oscillating the d-phase nozzle yielded repeatable patterns of multi-size droplets with smaller standard deviations at higher frequencies. Jet length reduction was the most common behavior observed in all pure water in oil studies upon oscillating the discharging nozzle. This effect was more dominant at initial stages of oscillation and decreased by increasing the oscillation frequency.

While the length of low viscous jets shortened by increasing the oscillation frequency, the high-viscous jet lengths increased slightly at initial frequencies, then remain unaffected at higher rates due to the dominant effect of viscous forces. Mid-viscous jet manifested a multi-stage behavior; at lower oscillation rates, where viscosity effects were dominant, the jet length slightly increased (as in high-viscous jet) and by increasing the frequency, the transverse motion became more effective and the jet length commenced to decrease (just as low-viscous jet).

The oscillating nozzle technique also showed promising results for ATPS in which the inherently low interfacial tension bottlenecks the jet breakup. Upon oscillation, the jet length decreased and repeatable patterns of multi-size droplets with smaller sizes were observed as oscillation frequency was increased.

ase nozzle oscillation technique in order to generate multi-size, monodisperse droplets in conventional co-flow geometries. The growing droplet at the tip of the nozzle experiences an axial drag force imposed by the c-phase stream with a parabolic velocity distribution. As the needle oscillates, the nozzle repositions across the width of the channel with different streamlines experiencing different drag rates at each lateral position. In addition to this axial drag gradient, nozzle oscillation in transverse direction to the c-phase flow, creates a transverse drag induced by the relative velocity of flow and needle-tip. The variation in drag forces counter-reacting the constant interfacial forces lead to generation of multi-sized droplets with wide range of sizes especially smaller than the nozzle diameter.

 The effects of c- and d-phase fluid flow rates and needle oscillation frequency on the size and number of generated droplets were investigated in this study. Unlike other conventional passive methods, the oscillating d-phase nozzle technique was able to simultaneously produce a wide range of monodispersed droplets (4 nL up to 4 µL) at constant c- and d-phase flow rates with no modification in the physical properties of liquids. Droplet sizes were directly proportional to the *We* number and inversely proportional to the *Ca* number and oscillation frequency. By increasing the *Ca* number, the effect of axial drag became dominant over transverse drag. Thus, droplets were generated in smaller sizes but not very distinct from the stationery mode (pure axial drag), therefore an increase in dimensionless size of droplets was observed upon increasing the *Ca* number. For increased *Ca* numbers, axial drag variation was significant and at lower oscillation frequencies where transverse drag was not sufficiently large to compensate for axial drag reduction and the generated droplets became even larger than the stationary droplets. However, upon increasing the oscillation frequency, the transvers drag intensified and the size of generated droplets dropped

75

below the reference stationary sizes. This yielded a decrease in the size of generated droplets, however they were not very distinct from each other.

We also demonstrated the applications of oscillatory nozzle technique in suppressing the jetting effect via oscillation induced transverse drag. Effect of d-phase viscosity and oscillation frequency on jet length reduction was studied at different d- and c-phase flow rates. The transverse motion of dispersion nozzle can effectively decrease the jet length followed by increasing the throughput of droplet generation. Furthermore, increasing the d-phase flow rate (*We* number) lead to elevation of jet length at constant c-phase flow rates (*Ca* number), while increasing the *Ca* number inversely affected the jet length. Jet length reduction was the most common behavior observed in all pure water in oil studies upon oscillating the nozzle. This effect was more dominant at initial stages of oscillation and decreased by increasing the oscillation frequency. While the length of low viscous jets shortened by increasing the oscillation frequency, the high-viscous jet lengths increased slightly at initial frequencies, then remain unaffected at higher rates due to the dominant effect of viscous forces. Mid-viscous jet manifested a multi-stage behavior; at lower oscillation rates, where viscosity effects were dominant, the jet length slightly increased (as in high-viscous jet) and by increasing the frequency, the transverse motion became more effective and the jet length commenced to decrease (just as low-viscous jet). We also did preliminary experiments of jet disintegration via oscillation in ATPS in which due to ultra-low interfacial tension conditions, stable jets form and droplet generation is not feasible. Upon increasing the frequency, the oscillating jet disintegrated into repeatable patterns of multi-size small droplets.

In conclusion, by introducing a variant axial drag and an additional transverse drag to the co-flow system in the dripping regime, multi-size monodisperse droplets were simultaneously generated at

constant flow rates. Moreover, oscillating-nozzle technique can effectively reduce the jet length in conventional co-flow devices operating in the jetting regimes.

6.2 Thesis Prospects

In our research, we studied droplet generation in a conventional co-flow device with an oscillating nozzle operating in both dripping and jetting regimes. There are several complementary studies that can be conducted in the future which are discussed below.

- Effect of nozzle oscillation on the number and size of generated droplets can be studied in a wide range of flow rates at different frequencies to accomplish a comprehensive guide map for droplet generation at desired range of sizes.

- Effect of smaller nozzle dimensions on the number, size and throughput of generated droplets can be studied. Smaller nozzle dimensions can effectively increase the throughput and reduce the overall size of the generated droplets.

- Experiments can be conducted to explore the effect of various physical properties such as different viscosity ratio of operating fluids and interfacial tension of immiscible fluids on the number and size of generated droplets. Visco-elastic liquids can also be selected as working liquids to mimic the biological fluids and study the effect of nozzle oscillation on droplet generation for non-Newtonian fluids.

- Downstream sorting of multi-size monodisperse droplets using established techniques such as pinch flow fractionation or expansion-contraction channels can be applied to separate the droplet clusters from each other and into different outlet streams in our device.

- The oscillating-nozzle co-flow technique can be employed for target encapsulation applications in low-concentration samples to perform size optimization that is required in some biological applications such as droplet based PCR.

- Last but not least, we believe nozzle oscillation can enhance droplet breakup by providing extra drag force where shear rates are not sufficient for d-phase disintegration. Preliminary experiments proved that this technique can be used in ATPS that inherently hold low interfacial tensions and droplet generation is a challenging task. A comprehensive study can be done to investigate the effect of oscillation on droplet generation in these systems.

APPENDICES

Appendix A: ACCURACY OF NEEDLE OSCILLATION MECHANISM

The accuracy of needle oscillation was examined before each experiment by comparing the input oscillation frequency with the needle tip transverse motion rate, obtained by video analysis, to make sure the needle oscillated at the desired frequency as shown in Figure A-1.

Equation	y = a + b*x
Plot	Output (Image An
Weight	No Weighting
Intercept	-0.00367
Slope	0.99997
Residual Sum of S	4.50577E-4
Pearson's r	1
R-Square(COD)	1
Adj. R-Square	1
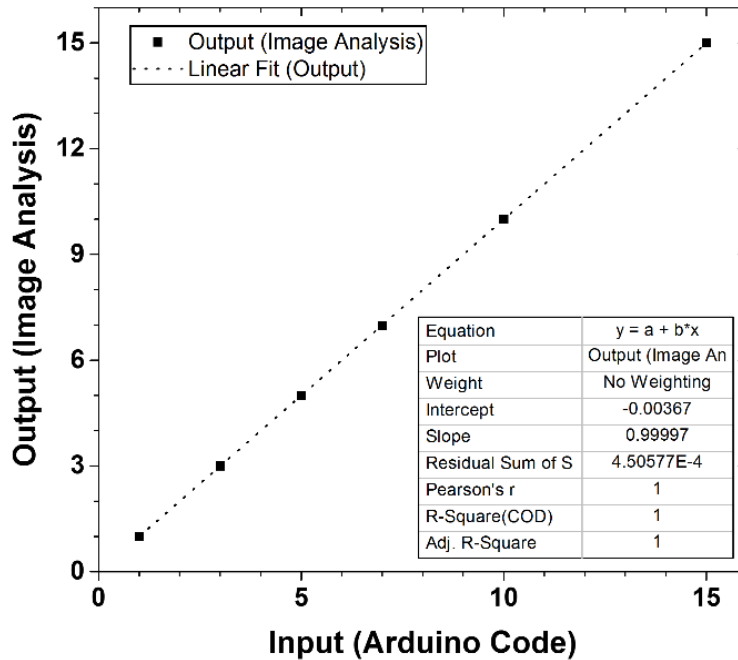
Figure A-1. Needle oscillation accuracy curve

The linear motion of the needle was also verified by video analysis at frequencies of f=1, 5 and 10 Hz by determining the lateral location of the needle tip inside the channel as shown in Figure 0-2 to Figure 0-4.

79
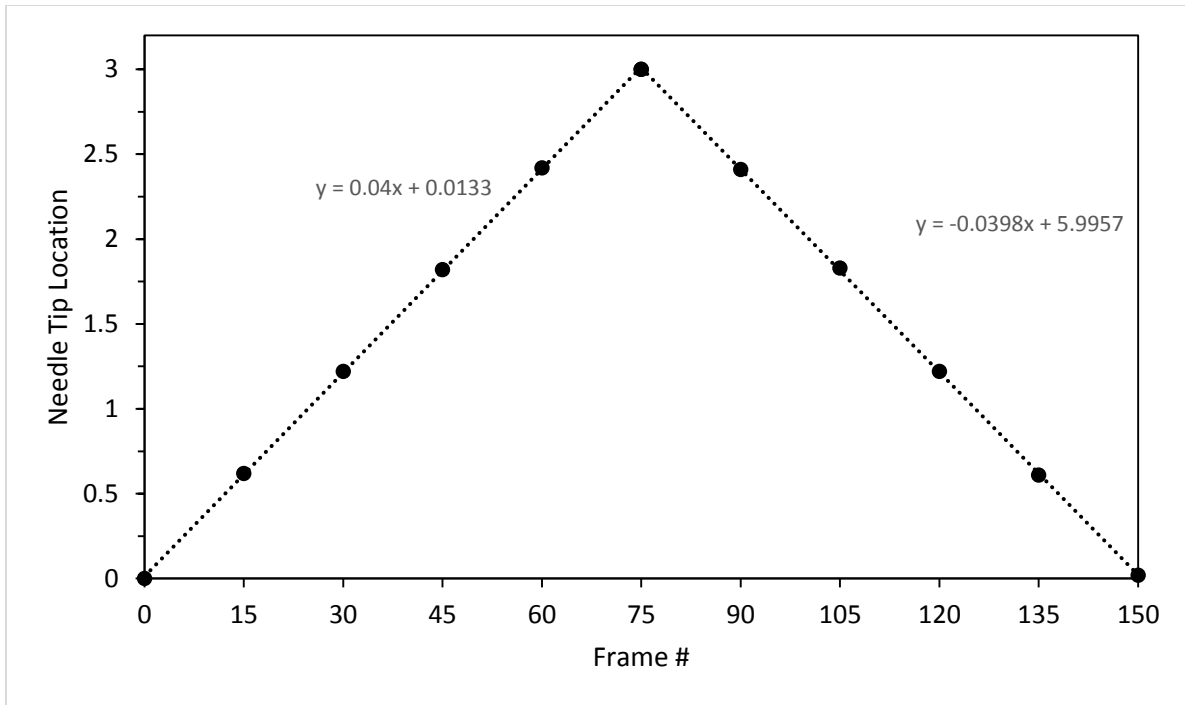
Figure 0-2. Lateral locations of nozzle in a full cycle of oscillation at 1Hz.
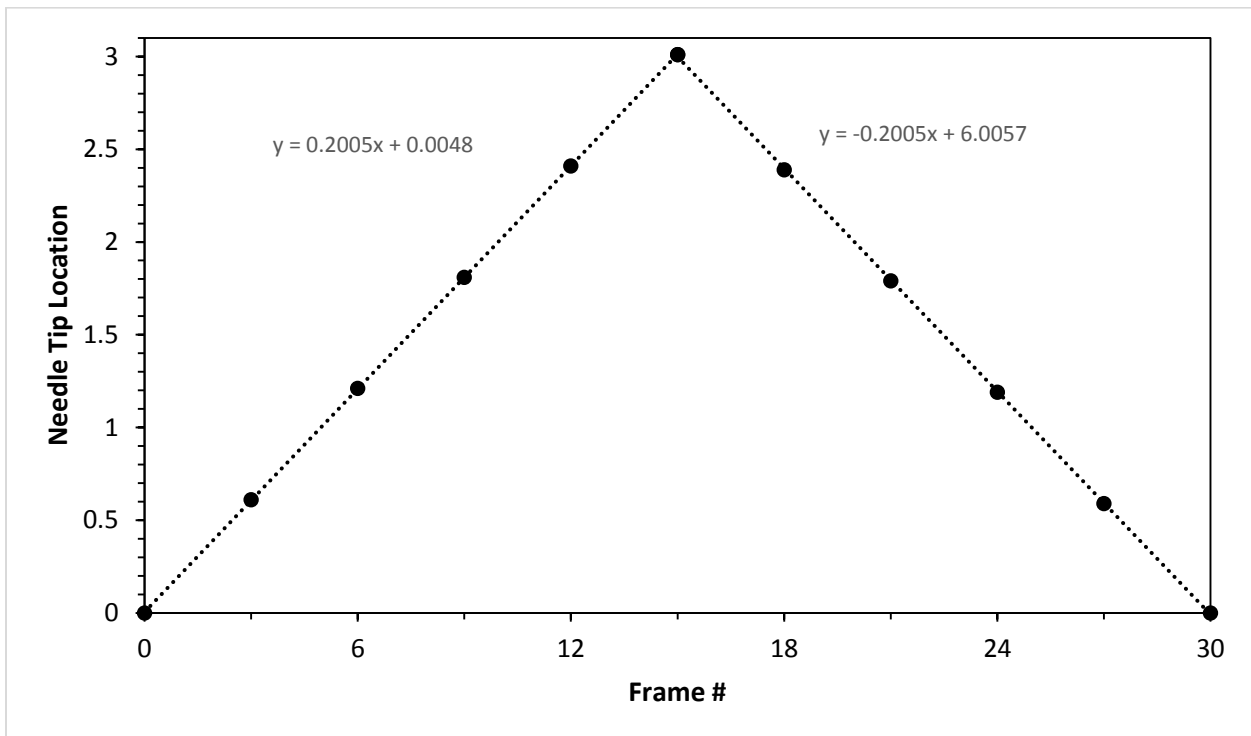
Figure A-3. Lateral locations of nozzle in a full cycle of oscillation at 5Hz.
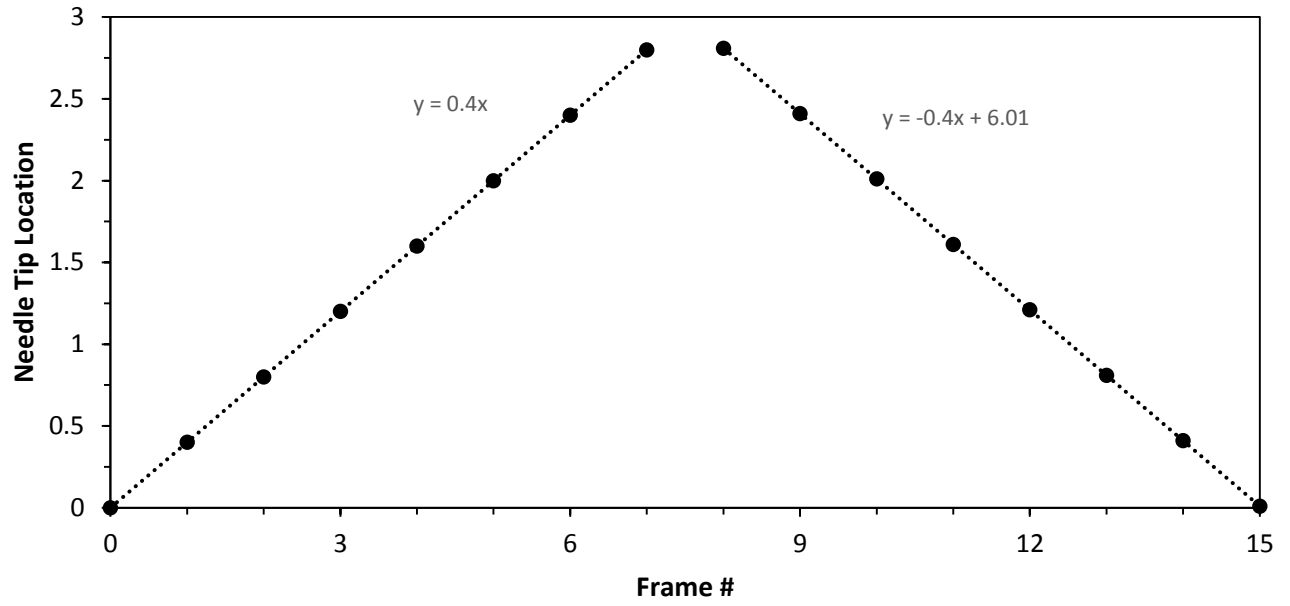
Figure 0-4. Lateral locations of nozzle in a full cycle of oscillation at 10Hz

Appendix B: CLUSTERING

Clusters are homogenous groups of objects that are classified according to their common characteristics. Cluster members can be identified by either internal cohesion or external isolation. Internal cohesion is defined as if the individual data point meets the minimum criteria to be accepted as a cluster member or not. On the other hand, external isolation focuses on existence of a discontinuity between classes[153]. A better classification is possible if both criteria are applied; while the similarities are maximized, dissimilarities are minimized yielding into more distinct clusters.

Clustering algorithms can be divided into two main categories: hierarchical and square-error partitional algorithms[154]. Hierarchical algorithms benefits predefined nested clusters for categorizing objects while square-error partitional methods simultaneously recognize all clusters as partitions of data points and attempt to obtain the partition that minimizes the within-cluster dispersity or maximizes the between-cluster scatter. For instance, in a group of data with n number of population, k number of clusters can be identified starting from one large cluster ($k=1$) up to the point that each data point is considered as an individual cluster ($k=n$). There are two schemes for hierarchical clustering: agglomerative and divisive schemes. The hierarchy construction is totally opposite in these two methods. Agglomerative methods start when all members are individual clusters (at *step=0*, *k=n*) and gradually merge the closest two clusters at each step until only one cluster is left (at *step=n-1*, *k=1*). On the contrary, divisive methods start with one large cluster (at *step=0*, *k=1*) and in each step splits off the most isolated data point (or clusters in some conditions) until every data point becomes a cluster (at *step=n-1*, *k=n*). Figure 0-1, represent the comparative schematic of agglomerative (left to right) and divisive (right to left) methods.
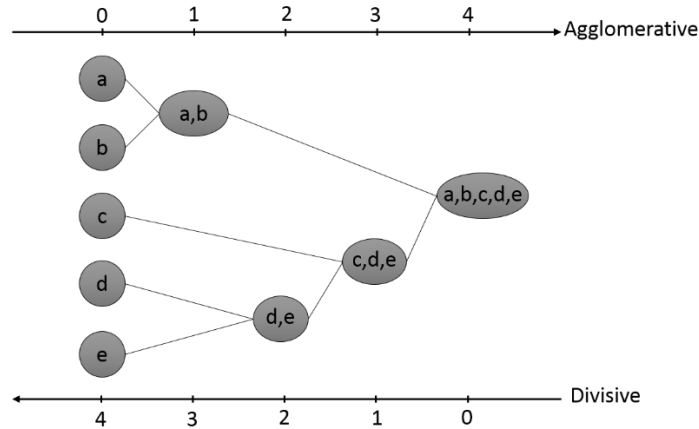
Figure 0-1. Comparative schematic of hierarchical methods; Agglomerative (left to right) and divisive (right to left)

The basic steps of an agglomerative hierarchical cluster analysis are summarized [155] as following:

---

a) Calculate a distance matrix which includes the distance between all the clusters.

b) Merge the two closest clusters.

c) Update the distance matrix to include the distance between the new cluster and the original ones, considering a clustering procedure.

d) Repeat the procedures (b) & (c) until only one cluster is left.

The divisive hierarchical algorithms are less common than agglomerative algorithms. However, when a relatively small number of clusters are desired, a divisive algorithm may be the desired choice. Further details about the hierarchical methods can be found in literature[156].

Hierarchical methods cover all possible number of clusters *(k=1~n)* along the way in smaller computation time, but the obtained clusters are not necessarily the best. They suffer from the defect that they cannot repair what was done in previous step. In fact, once two clusters merged by agglomerative algorithm, they cannot split or rearrange any more. Also if two clusters split up in a divisive algorithm, they cannot be reunited in further steps. A partitioning method rather than

nesting method is required in order to execute a dynamic clustering method which is not rigid and correction is possible after each step.

k-means clustering

k-means clustering[157] is a method commonly used to automatically partition a data set $X_i = \{X_1, X_2, ..., X_n\}$ with population of n members into k clusters, $C_j = \{C_1, C_2, ..., C_k\}$. k-means algorithm finds a partition such that the distance between data point X_i and centroid μ_j (average of cluster C_j) is minimized in Euclidean space[158]. In this method, at each step cluster can be re-defined and data points can be transferred to other clusters if they don't meet the minimum distance criteria.

Figure B-2 represents the flow chart of k-means clustering algorithm, which proceeds as follow:

a) Input: k (number of clusters), X_1, X_2, … , X_n (data set);

b) Place centroids μ_1, μ_2, … , μ_k at random data points;

c) For each data point X_i:

Find nearest centroid μ_j and assign data point X_i to cluster μ_j

d) For each cluster j=1, 2, … , k:

Calculate average of updated cluster members and assign it to new centroid μ_j.

e) Compare calculated μ_j with previous value; if they are not equal repeat steps (c) to (d) until it converges.

f) Return clusters.

g) End.
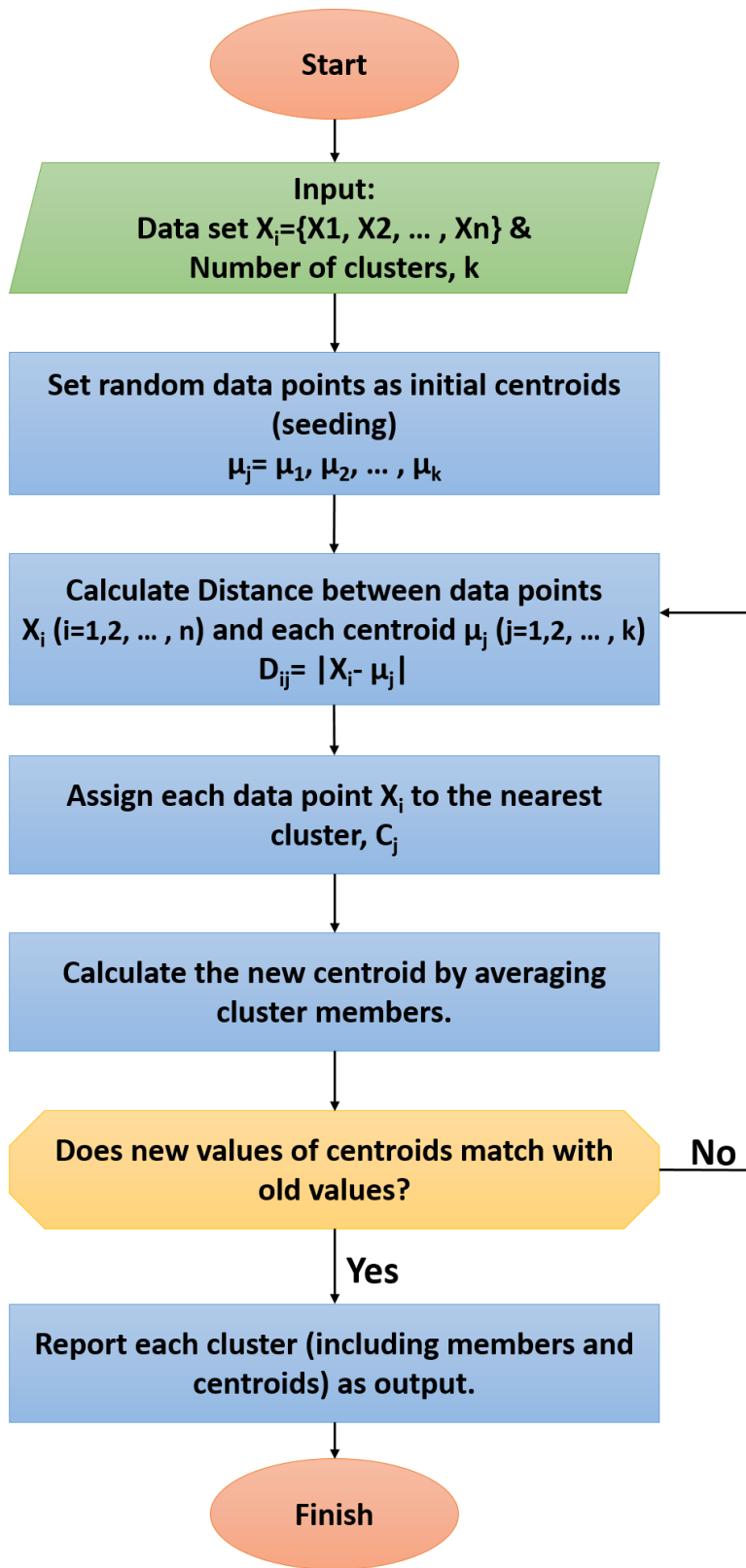
Figure B-2. Flow chart of k-means algorithm

A major problem with this algorithm is that it is sensitive to the selection of the initial centroids (seeds) and may converge to a local minimum if the seeds are not properly chosen. In order to tackle this problem, one can run the algorithm multiple times with different seeds, and the best configuration obtained from all of the runs can be used as the output clustering. Another technique is to begin with an initial guess of the group centroids often obtained via hierarchical method to iteratively find the solution.

As stated above, alongside the data points, the number of clusters should also be assigned to the algorithm to complete the clustering process. In some cases, number of the clusters is also unknown and further investigations are needed to define the optimum number of clusters (ONC). In cases as such, a clustering index must be defined and k-means algorithm should be applied for a range of k-values starting from the minimum, $k_{min}=2$, up to the maximum possible value, $k_{max}=$ population of data points. ONC can be detected by interpretation of clustering index behavior as a function of number of clusters.

Clusters should be internally cohesive which requires low-scattered data points in each group. It is obvious that increasing the number of clusters to the maximum possible k-value will continuously reduce the internal dispersion (variance) of data points but $k=n$ number of clusters for a data set with n members is not desirable. Therefore, another parameter should be considered alongside the variance to ensure the external isolation as well. In other words, the number of clusters should also be minimized while external isolation ensures the fact that existing clusters are far enough not to merge into a bigger cluster.

By increasing the number of clusters each partition becomes more focused and variance calculated within cluster decreases. Unlikely, sum of these variances does not continuously decrease and changes diminish after a specific point. The reason behind this behavior is that beyond this specific

point, clusters will start to subdivide into daughter clusters and the variance of mother cluster is almost equal to the sum of the variances of daughter clusters. Thus, assuming "sum of variances" as a measure for clustering quality can ensure cluster subdivision effectiveness. That specific point which can also be observed as a knee point in a graph of "sum of variances" vs. "number of clusters" indicates the optimum number of clusters in data set[159]. In most of the cases that population is high there's no need to explore the whole possible range for k and a rough estimation about maximum number of clusters can be done based on the number of peaks observed in graph of data distribution density. Setting k_{max} reasonably above the estimated value can conservatively save a huge portion of computation time.

For clustering generated droplets in both jet length reduction and multiple size droplet generation assays, sum of variances is taken as clustering index and maximum number of clusters were manually selected as k=10 and k=9 respectively to reduce the process time for all cases. The data point distribution and clustering index graph in jet length reduction assays for We=8.75×10^{-3} and Ca=235×10^{-3} at 15 Hz is show in Figure 0-3. Results for multiple droplet generation assay at We=40.8×10^{-3} and Ca=20.4×10^{-3} in oscillation frequency of 15 Hz is show in Figure 0-4.
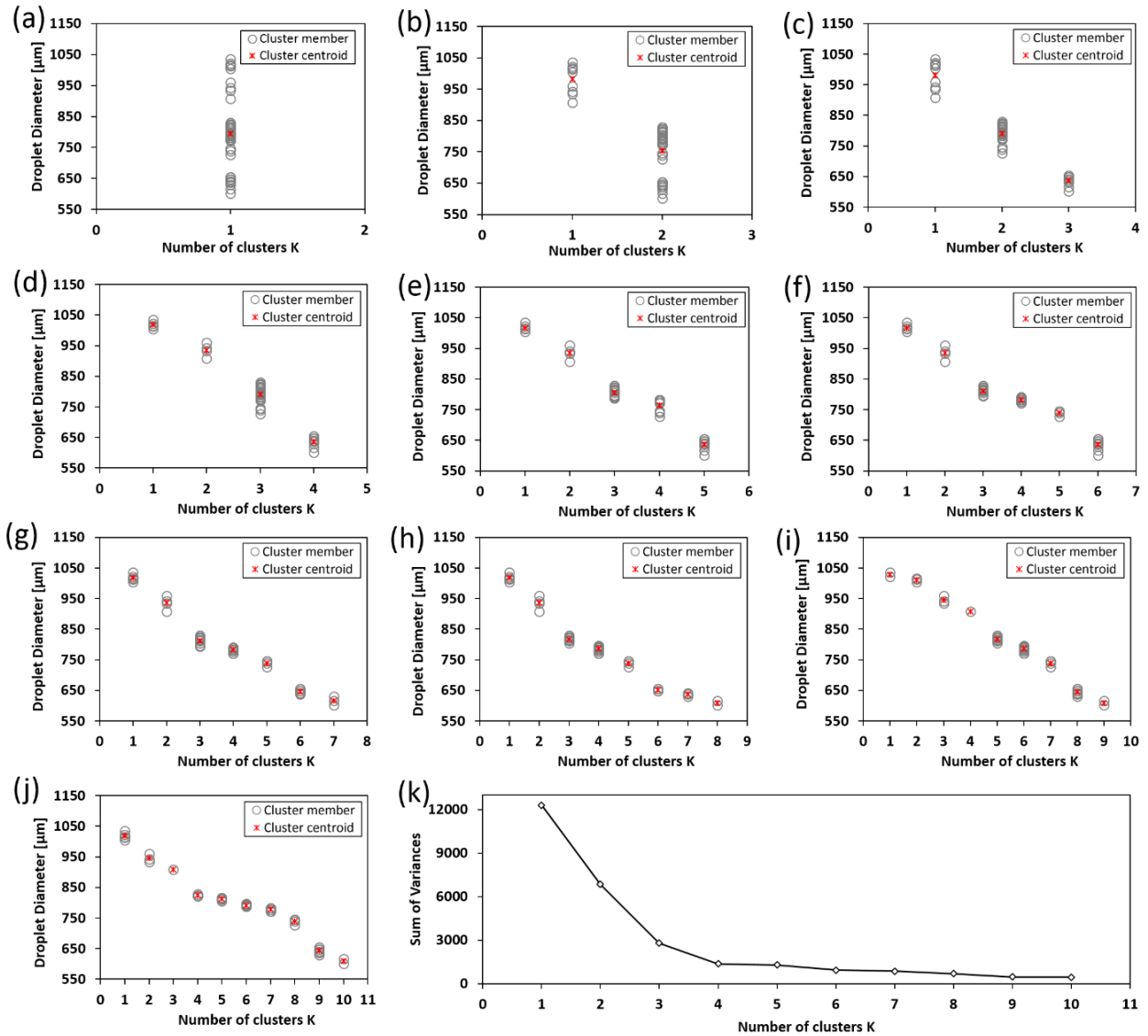
Figure 0-3. Data distribution for different cluster numbers: (a)-(d): Effective subdivision by increasing cluster numbers up to k=4 (e)-(j) Ineffective cluster subdivision beyond k=4; total variance of daughter clusters is approximately equal to variance of mother cluster, (k) Clustering index vs number of clusters which shows ineffective subdivisions beyond k=4 known as knee point.

As shown in Figure 0-3(k), after k=4 clustering index does not reduce effectively and beyond this point clusters are ineffectively subdivided into daughter clusters in a way that total variance of daughter droplets are approximately equal as mother cluster. To get consistent results, clustering process repeated at least 10 times for each set of data to avoid improper seeding and consequently local minimum convergence problem.

88
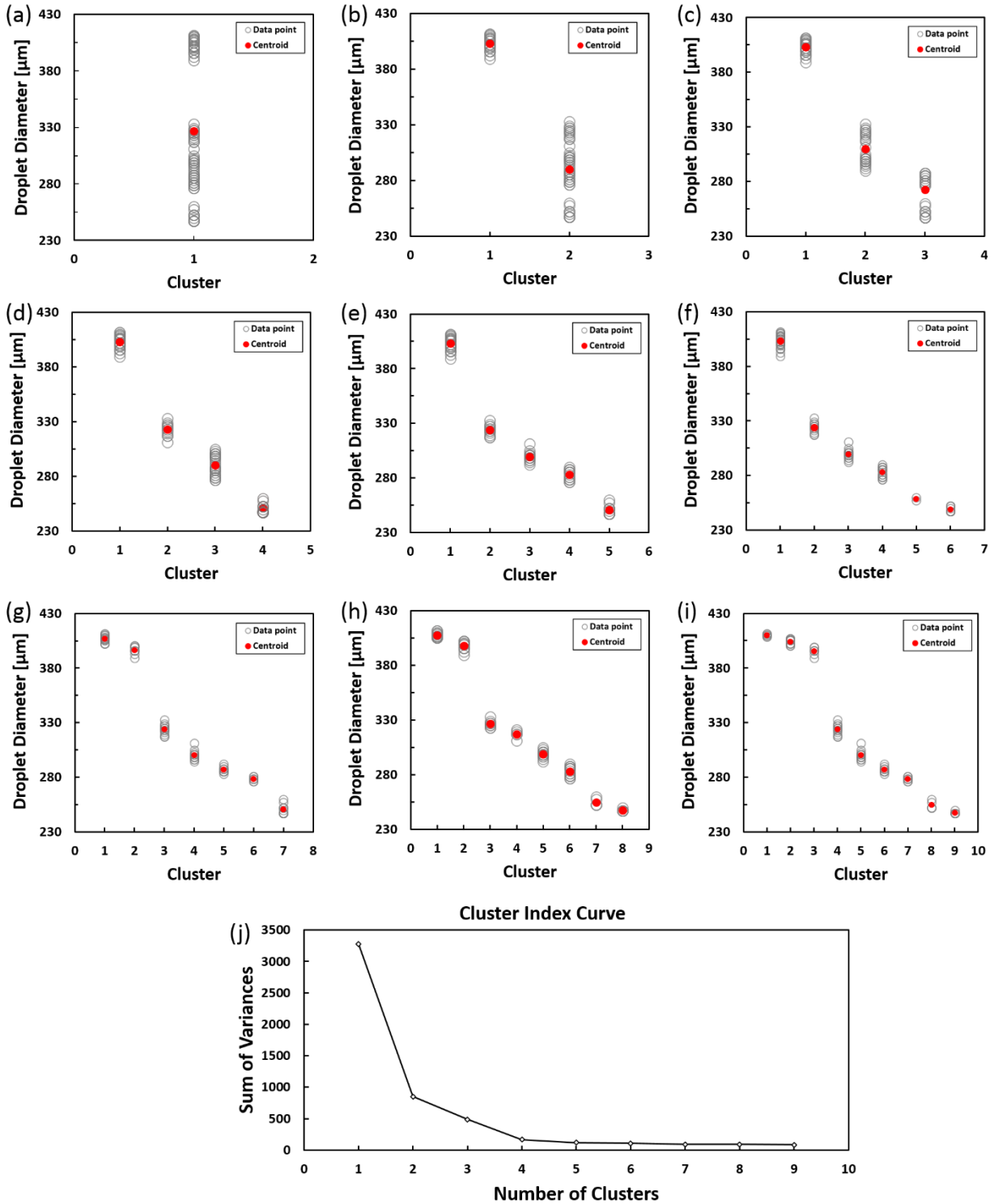
Figure 0-4. Data distribution for different cluster numbers: (a-d): Effective subdivision by increasing cluster numbers up to k=4 (e-i) Ineffective cluster subdivision beyond k=4; total variance of daughter clusters is approximately equal to variance of mother cluster, (j) Clustering index vs number of clusters which shows ineffective subdivisions beyond k=4 known as knee point.

As shown in Figure 0-4 j, after $k=4$ clustering index does not reduce effectively and beyond this point clusters are ineffectively subdivided into daughter clusters in a way that total variance of daughter droplets are approximately equal as mother cluster. To get consistent results, clustering process repeated at least 10 times for each set of data to avoid improper seeding and consequently local minimum convergence problem.

Appendix C: SUPPLEMENTARY GRAPHS FOR MULTI-SIZE MONODISPERSE DROPLET GENERATION

C.1 Effect of Frequency on number and size of generated droplets

Increasing oscillation frequency resulted in increase in number of generated droplets with a general decrease in their sizes. Figure 0-1, represents the images of generated droplets at We=10.2×10^{-3} and Ca=20.4×10^{-3} as oscillation frequency increases from 0Hz to 15Hz.
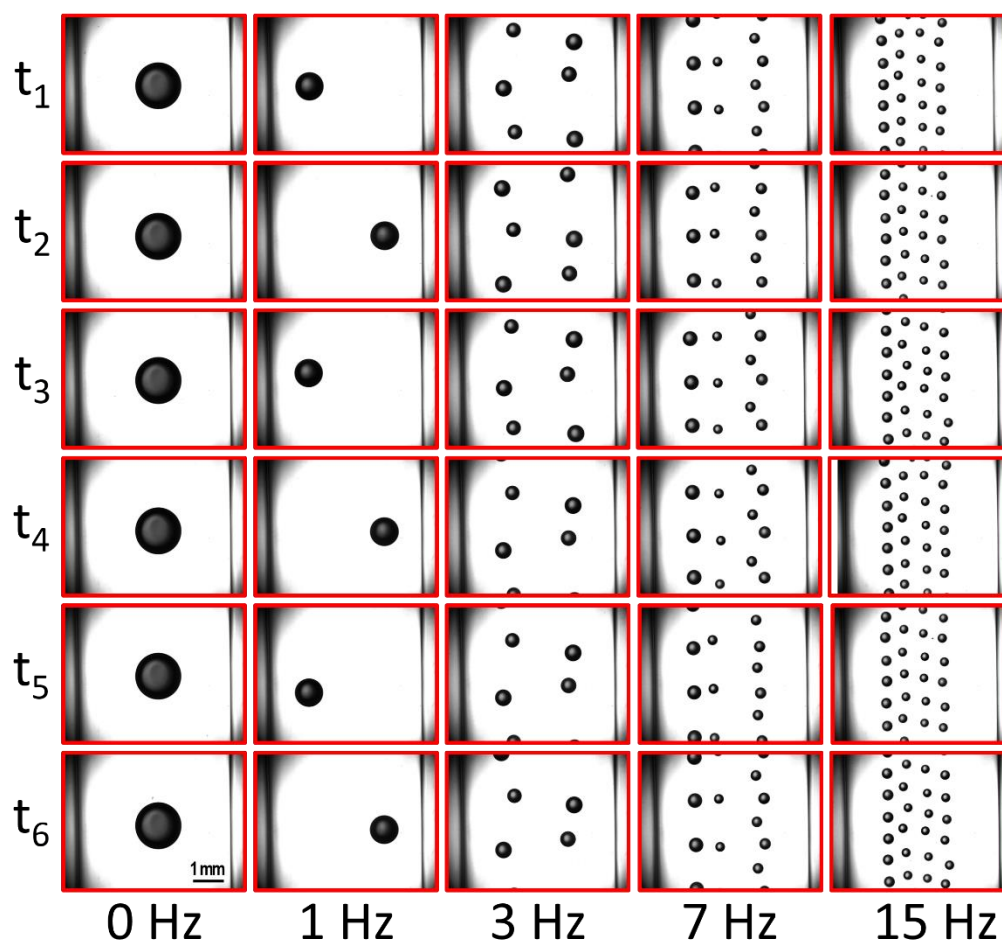
Figure 0-1. Effect of Oscillation on Droplet size and throughput at We=10.2×10^{-3} and Ca=20.4×10^{-3}

Droplet size distribution and throughput for various oscillation frequencies at We=40.8×10^{-3} and Ca=20.4×10^{-3} are shown in Figure 0-2.
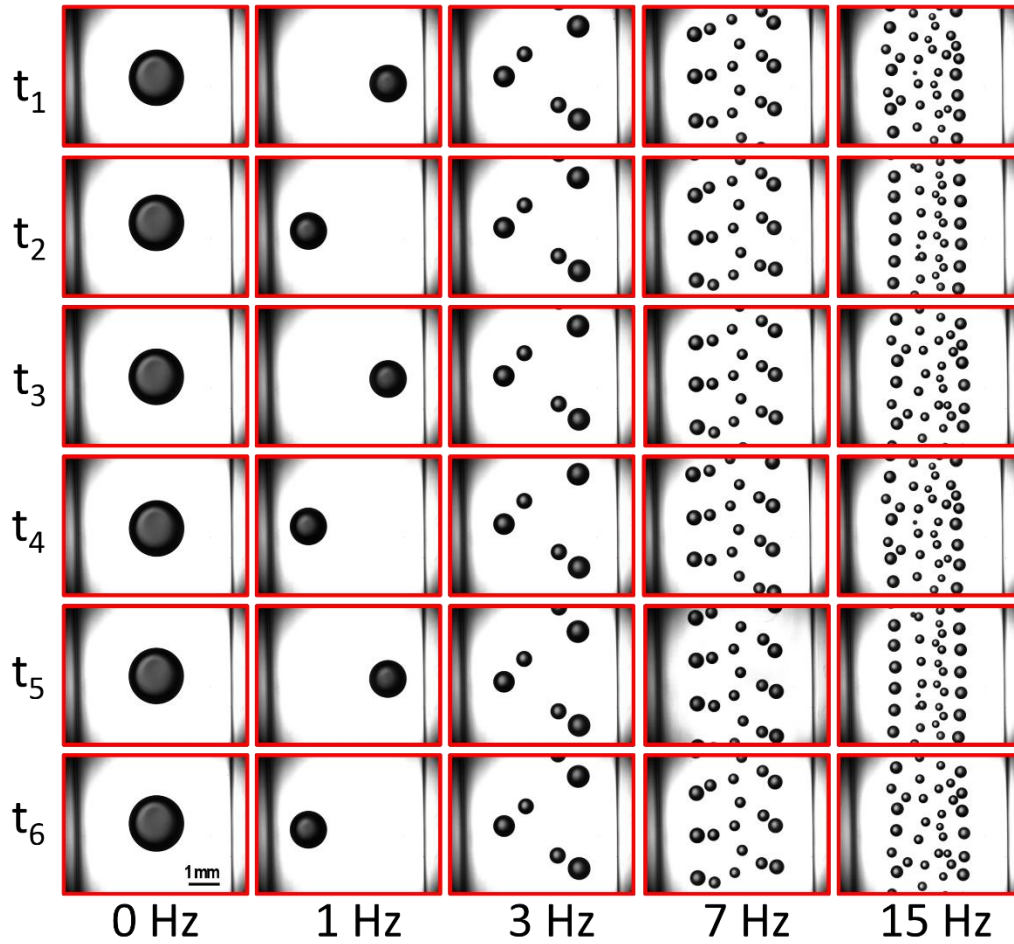
Figure 0-2. Effect of oscillation on droplet size and throughput at We=40.8×10^{-3} and Ca=20.4×10^{-3}

Figure 0-3, also illustrates the droplet size and throughput for different oscillation frequencies at We=1021×10^{-3} and Ca=20.4×10^{-3}. For this flow conditions, at highest oscillation frequency due

to high droplet generation rate and low c-phase velocities, droplets happen to overlap and the droplet size assessment was not feasible.
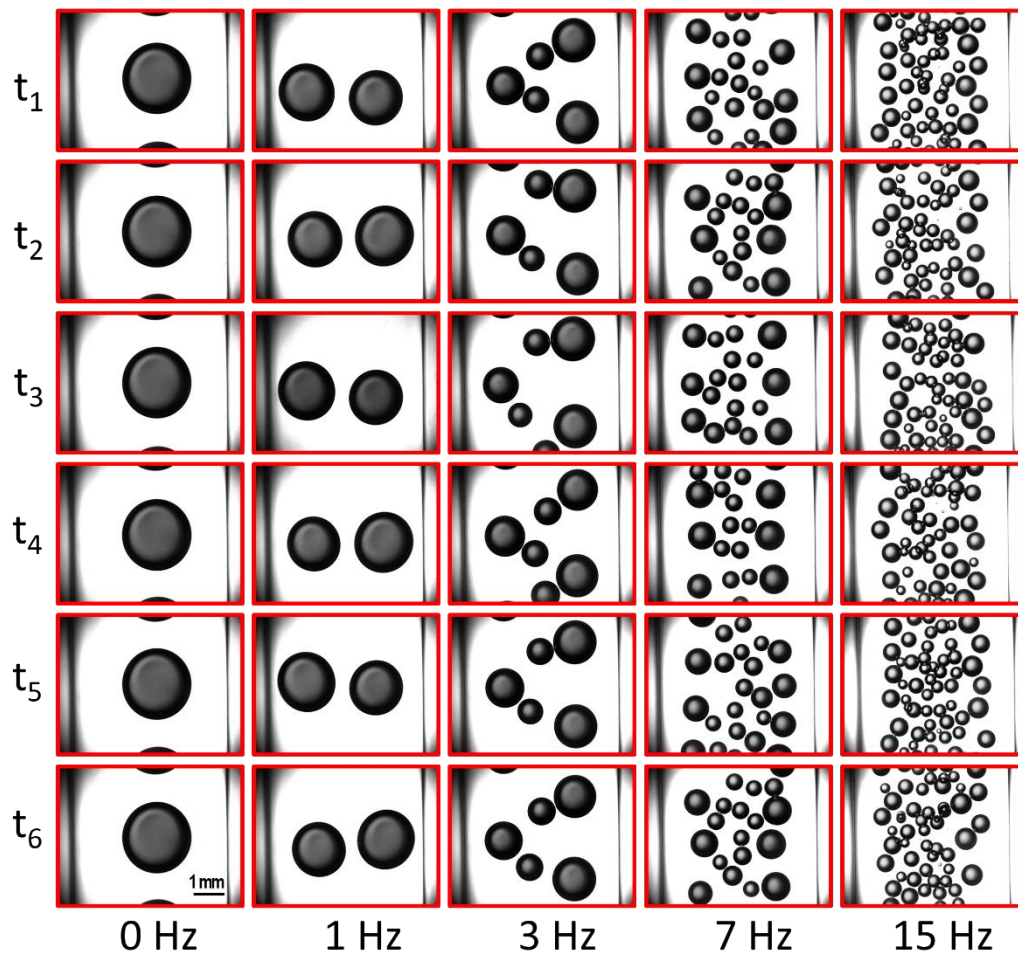
Figure 0-3. Effect of Oscillation on Droplet size and throughput at We=1021×10⁻³ and Ca=20.4×10⁻³. Due to overlap of droplets size assessment was not feasible at 15Hz for this flow conditions.

Figure C-4, Figure C-5 and Figure 0-6, represent the droplet size and throughput for different oscillation frequencies at Ca=51×10^{-3} for We=10.2×10^{-3}, We=40.8×10^{-3} and We=1021×10^{-3}, respectively.
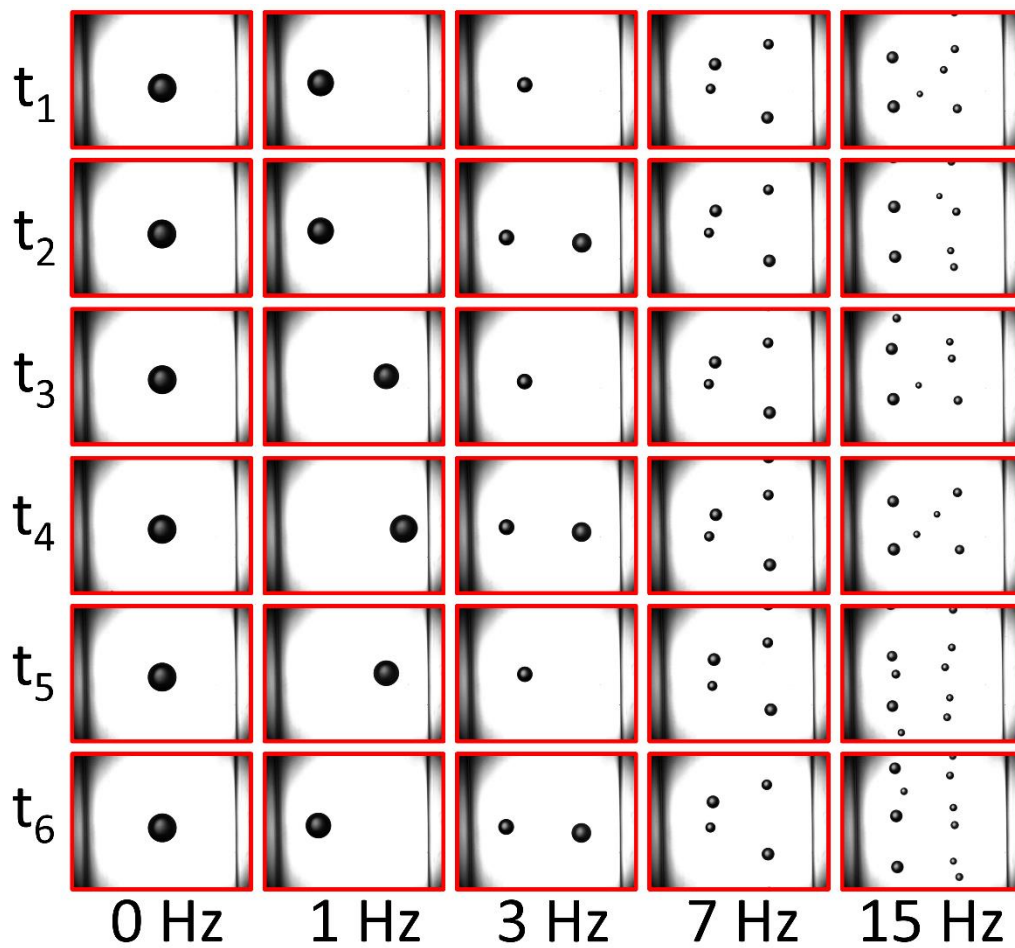
Figure C-4. Effect of Oscillation on Droplet size and throughput at We=10.2×10^{-3} and Ca=51×10^{-3}
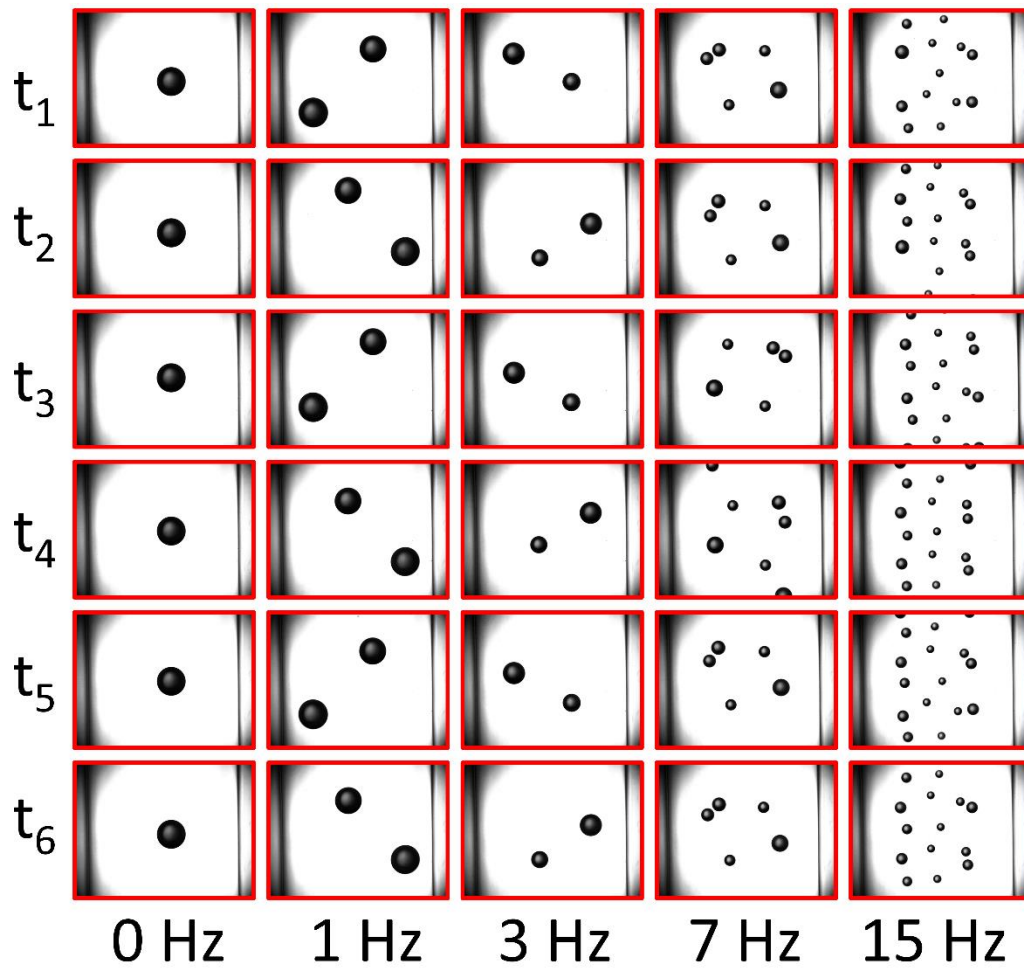
Figure C-5. Effect of Oscillation on Droplet size and throughput at We=40.8×10^{-3} and Ca=51×10^{-3}
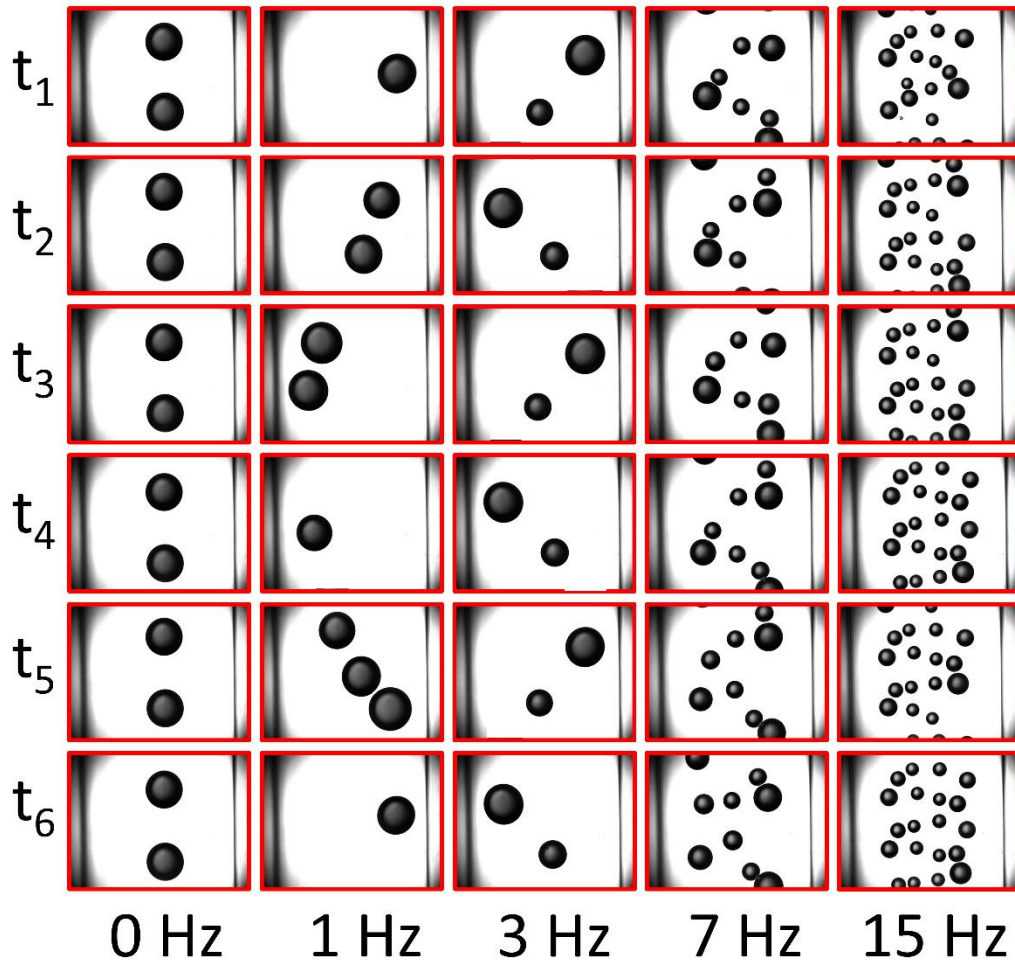
Figure 0-6. Effect of Oscillation on Droplet size and throughput at We=1021×10^{-3} and Ca=51×10^{-3}

And finally, Figure C-7, Figure 0-8 and Figure C-9, illustrate the droplet size and throughput for different oscillation frequencies at $Ca=102\times10^{-3}$ for $We=10.2\times10^{-3}$, $We=40.8\times10^{-3}$ and $We=1021\times10^{-3}$, respectively.
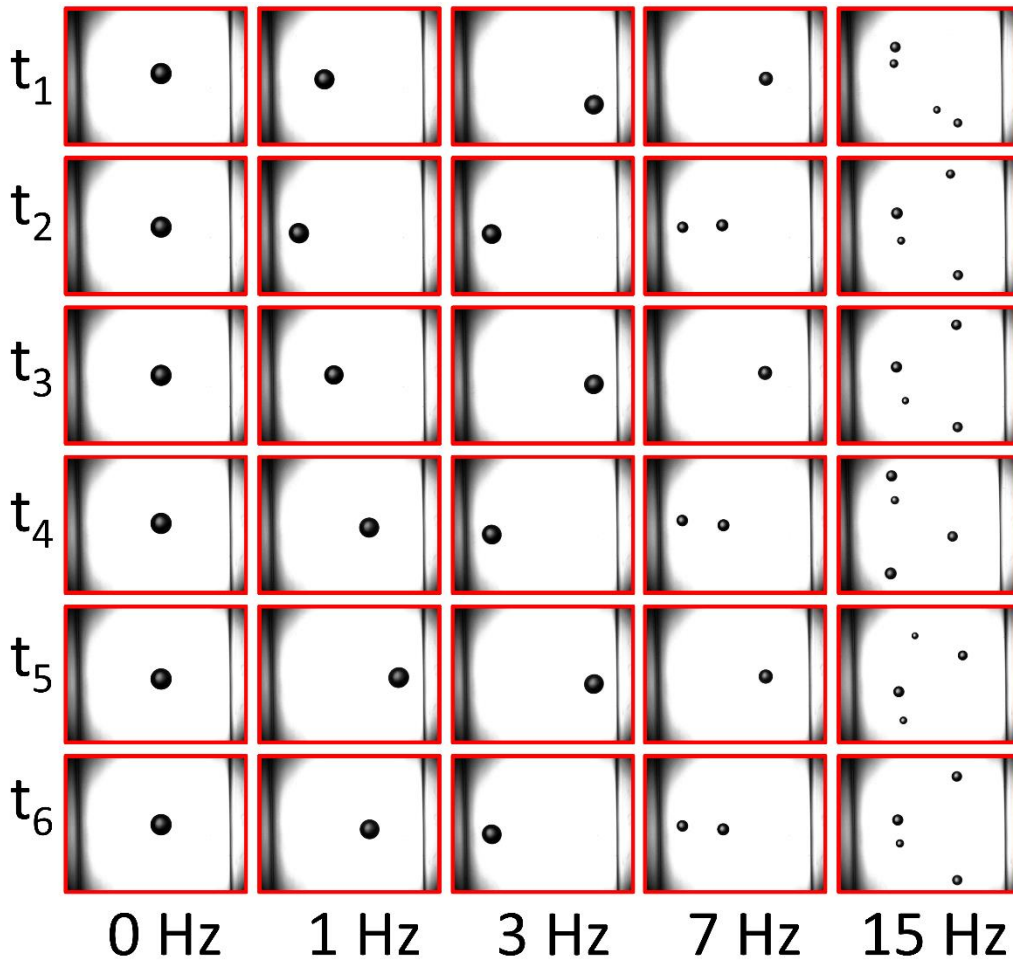
Figure C-7. Effect of Oscillation on Droplet size and throughput at $We=10.2\times10^{-3}$ and $Ca=102\times10^{-3}$
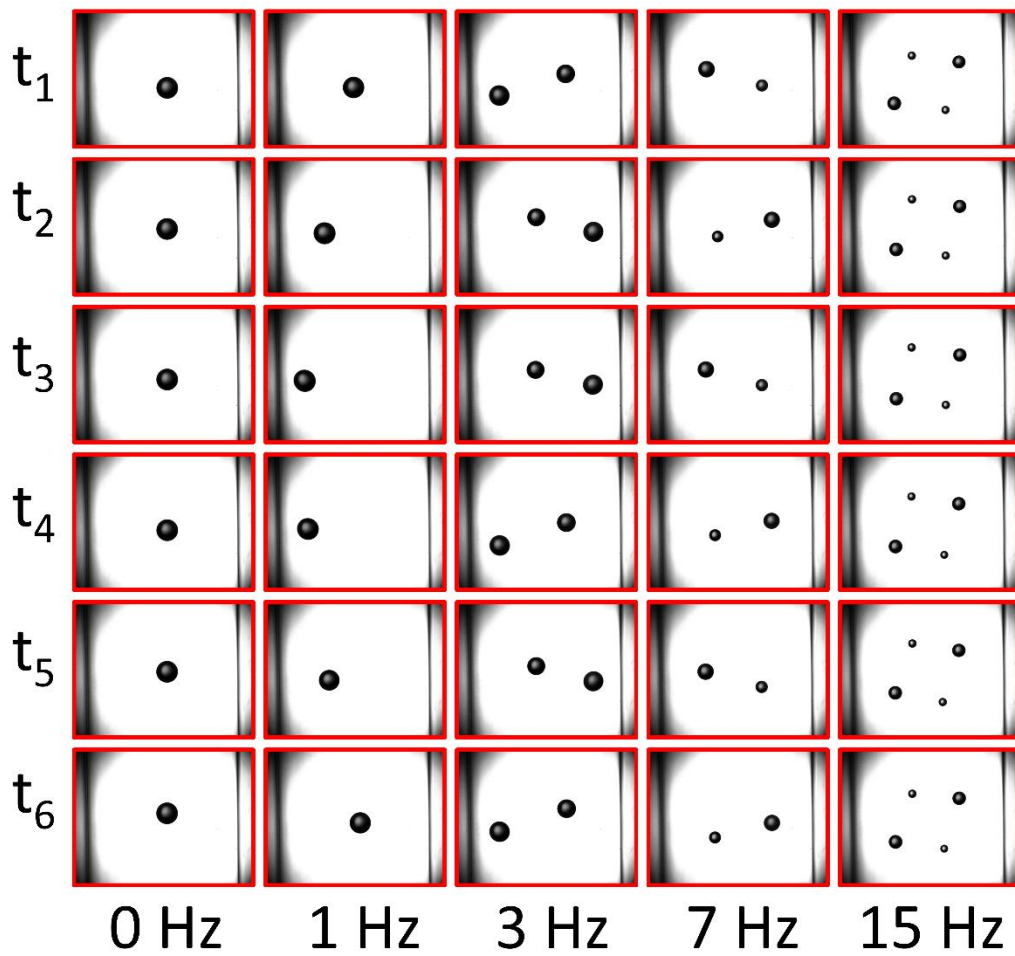
Figure 0-8. Effect of Oscillation on Droplet size and throughput at We=40.8×10⁻³ and Ca=102×10⁻³
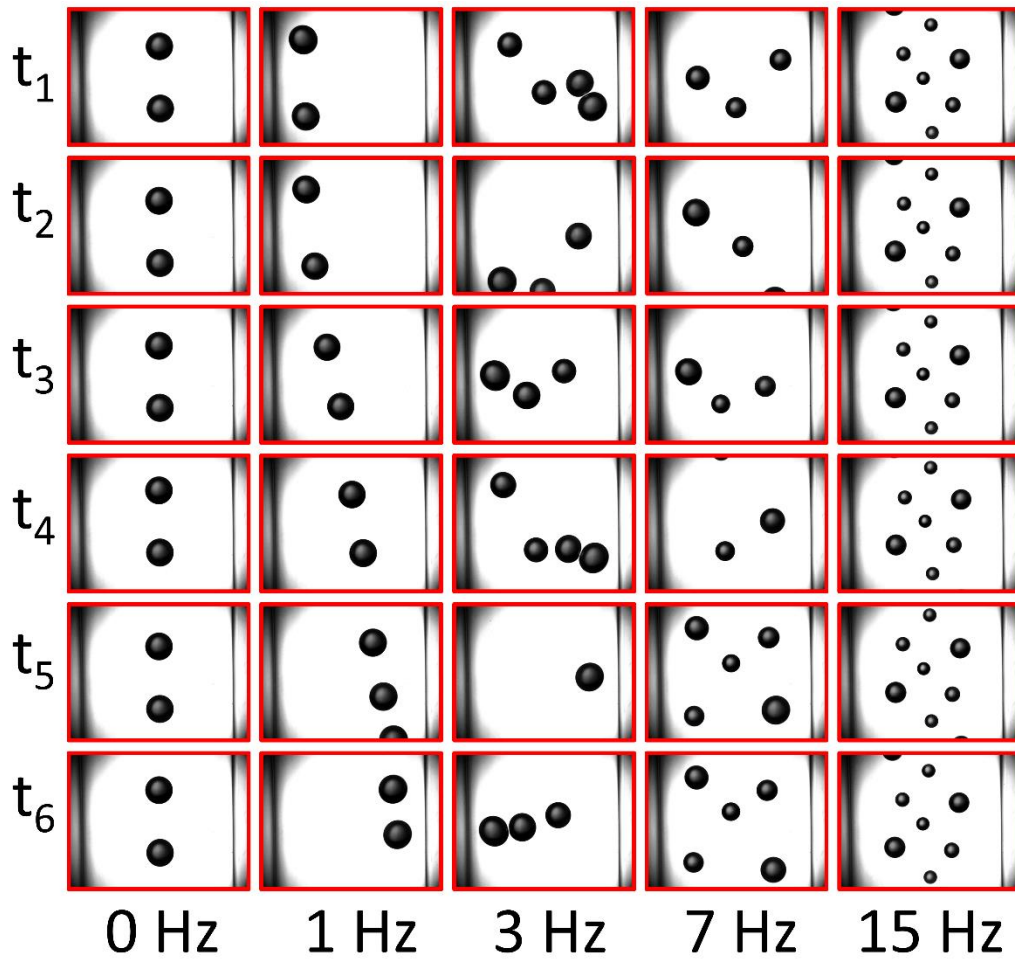
Figure C-9. Effect of Oscillation on Droplet size and throughput at We=1021×10⁻³ and Ca=20.4×10⁻³

Normalized dimeters, at different oscillation frequencies and various We-Ca conditions are illustrated in Figure 0-10.
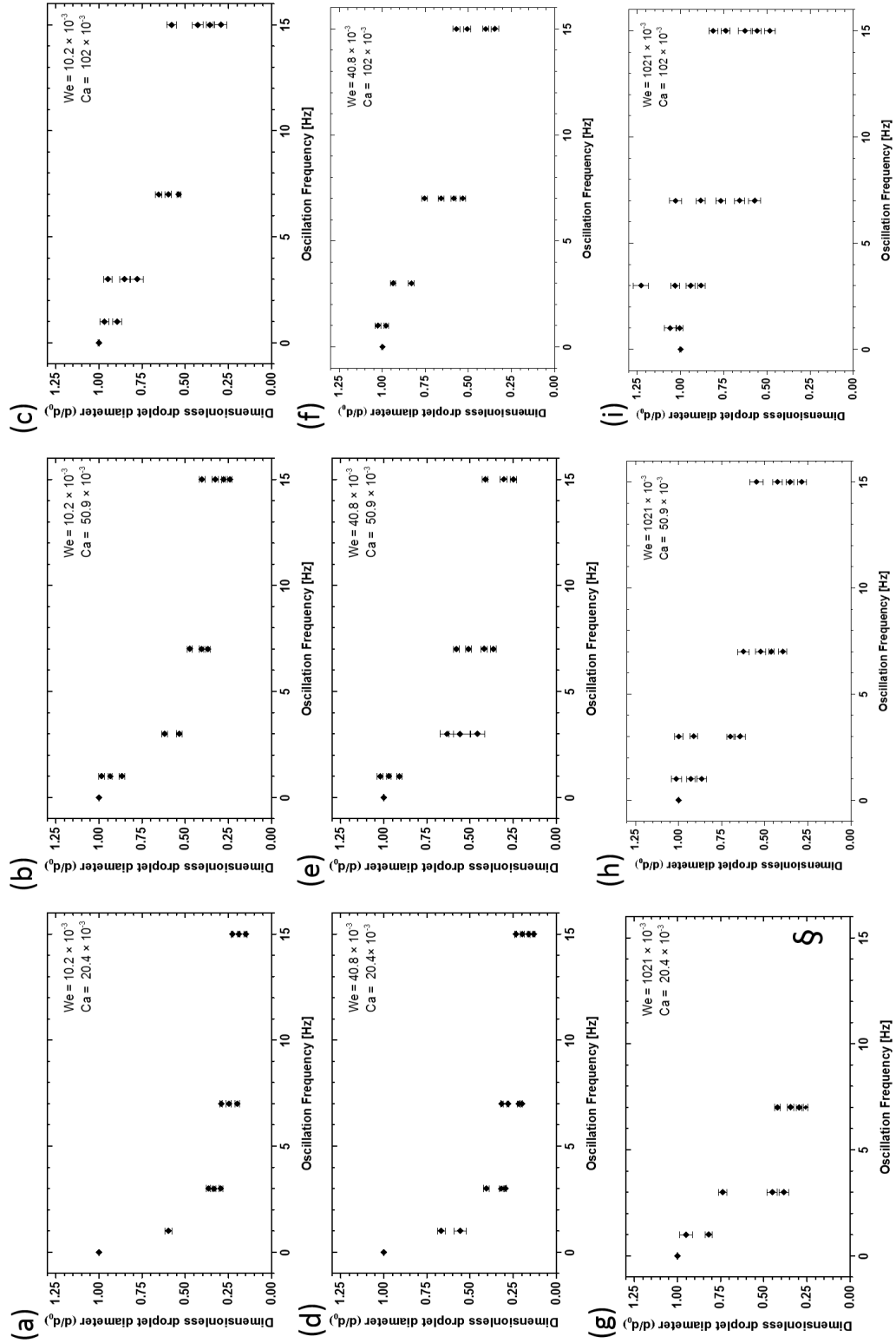
Figure 0-10. Effect of oscillation frequency on number and normalized diameter of droplets at different We-Ca numbers. The symbol § in (g) indicates a condition under which the generated droplets overlapped due to increased throughput and image processing-based edge detection and size assessment were not feasible.

C.2 Effect of Ca on number and actual size of generated droplets

Effect of c-phase flow rate (represented by *Ca* number) on the number and dimensionless diameter of generated droplets at different oscillation frequencies for $We = 40.8{\times}10^{-3}$ and $We = 1021{\times}10^{-3}$ are illustrated in Figure 0-11 and Figure 0-12, respectively.
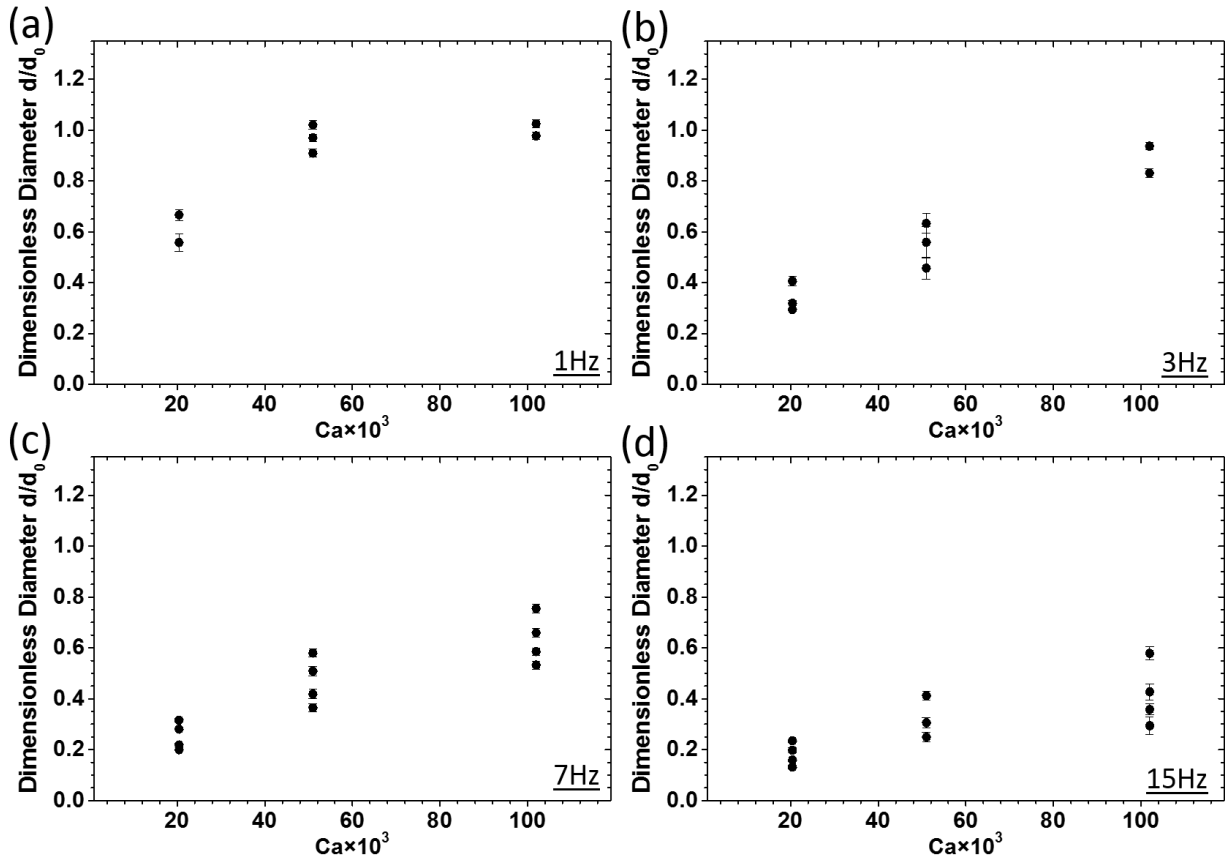
Figure 0-11 Effect of c-phase flow rate (Ca number) on dimensionless size and number of generated droplets at a constant d-phase flow rate (We=40.8×10⁻³) and at various oscillation frequencies of (a) 1 Hz, (b) 3 Hz, (c) 7 Hz, and (d) 15 Hz.

.
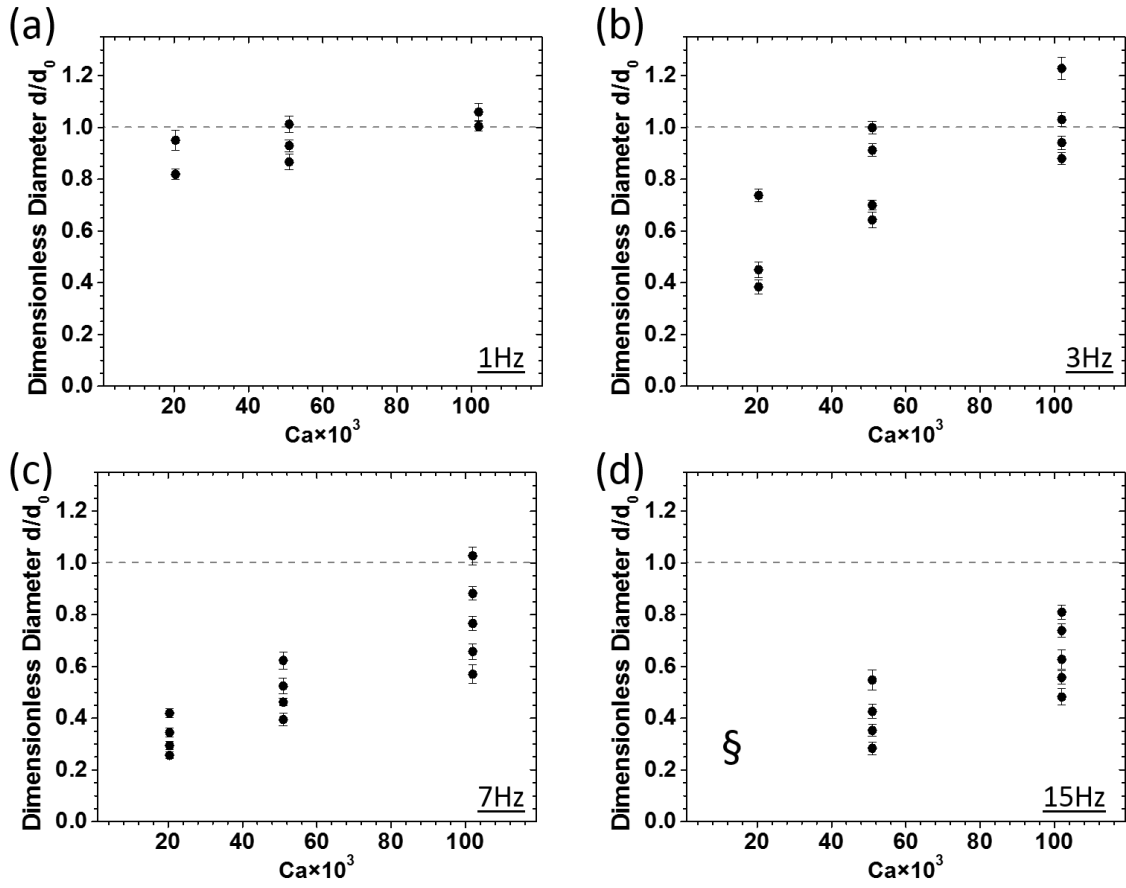
Figure 0-12. Effect of c-phase flow rate (Ca number) on dimensionless size and number of generated droplets at a constant d-phase flow rate (We=1021×10⁻³) and at various oscillation frequencies of (a) 1 Hz, (b) 3 Hz, (c) 7 Hz, and (d) 15 Hz. The symbol § in (d) indicates a condition under which the generated droplets overlapped due to increased throughput and image processing-based edge detection and size assessment were not feasible.

Appendix D: SUPPLEMENTARY GRAPHS FOR JET LENGTH REDUCTION

D.1 Effect of d- and c-phase Flow Rates on Stationary Jet Length

The data in the Chapter five were reproduced to show the effect of c-phase (*Ca* number) and d-phase (*We* number) flow rates on the stationary jet length as shown in Figure 0-1 and Figure 0-2, respectively.
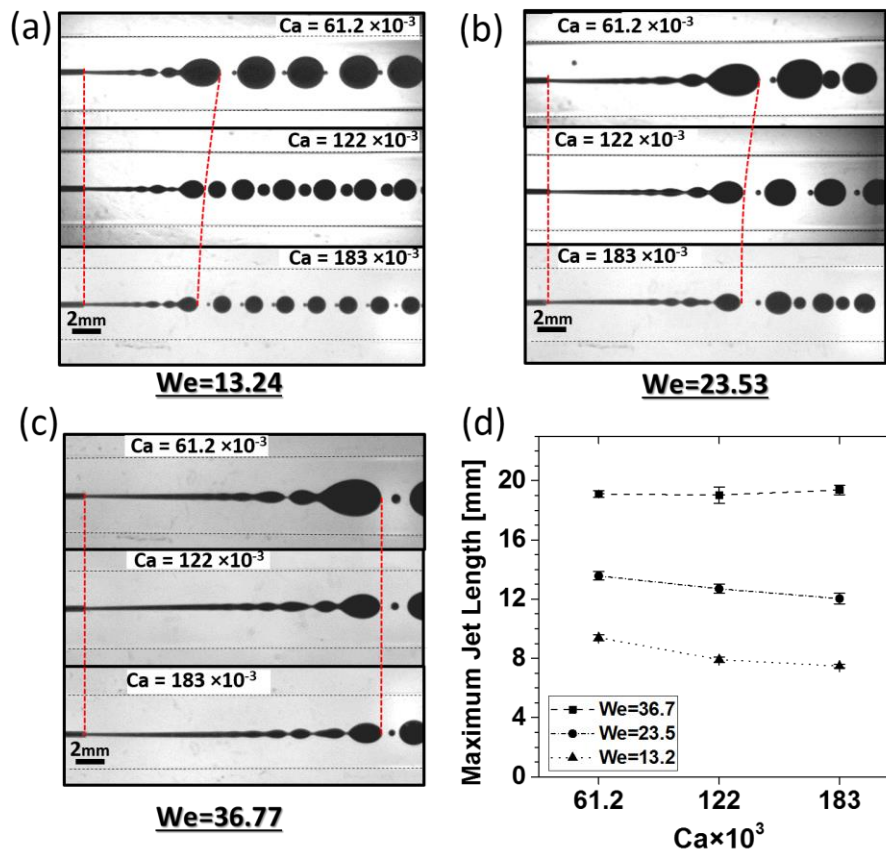
Figure 0-1. Effect of Q_c (Ca number) on the stationary jet length. Jet images at (a) We = 13.24, (b) We =23.53, and (c) We =36.77 are shown while (d) demonstrates the aggregated effect of Ca number on the jet length at various We numbers.
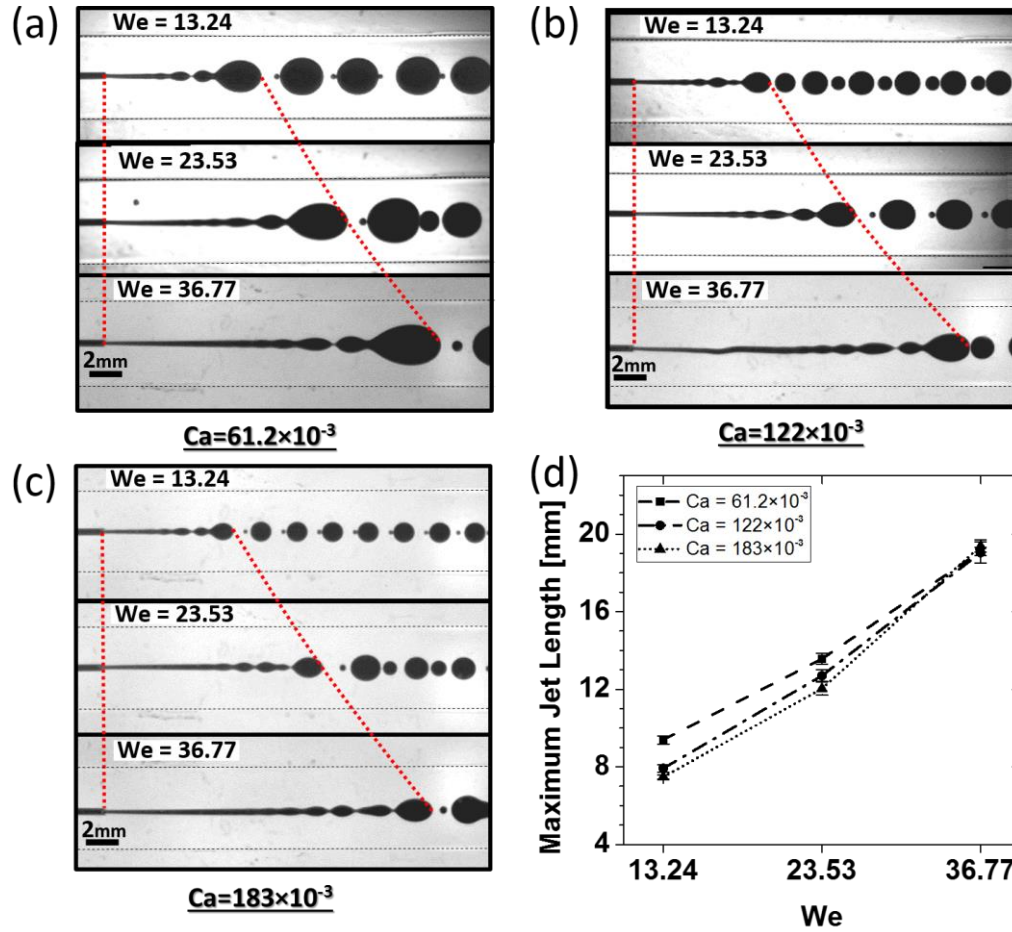
Figure 0-2. Effect of Q_d (We number) on the stationary jet length. Jet images are shown at (a) Ca = 61.2×10^{-3}, (b) Ca =122×10^{-3}, (c) Ca =183×10^{-3} while (d) demonstrates the aggregated effect of We number on the jet length at various Ca numbers.

D.2 Effect of d-phase Flow Rate on the Oscillating Jet Length

The data in the Chapter five was reproduced to show the effect of d-phase flow rate on the oscillating jet length as shown in Figure 0-3. At constant frequency and *Ca* levels, the jet length was observed to proportionally increase by increasing the d-phase flow rate. However, the effect of d-phase flow rate was more significant at slower oscillation rates. This observation is in accordance with the fact that jets were longer at increased d-phase flow rates and thus were inherently more unstable at initial oscillation frequency levels.
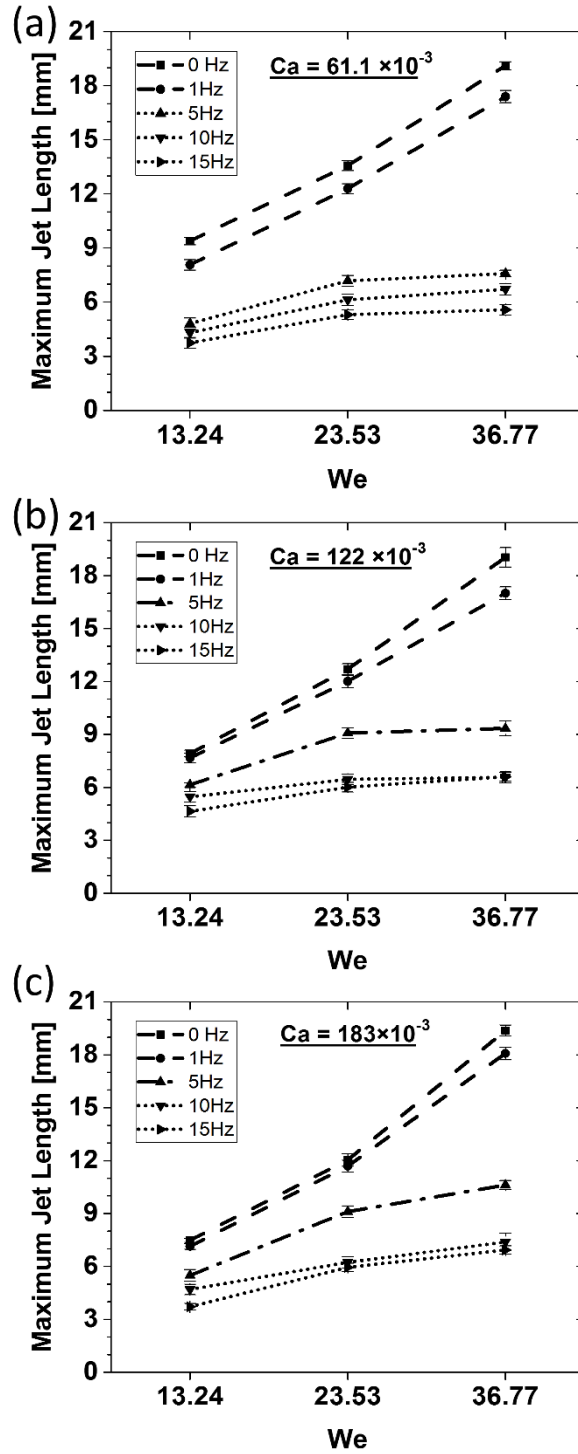
Figure 0-3. Effect of d-phase flow rate on jet length at different oscillation frequencies for (a) Ca = 61.1×10⁻³, (b) Ca =122×10⁻³ and (c) Ca =183×10⁻³

References:

1. Singh, D., Reist, P.: Evaluation of acoustical particle counter for the sizing of fog droplets. 35–44 (1991).

2. van Beeck, J.P., Riethmuller, M.L.: Rainbow phenomena applied to the measurement of droplet size and velocity and to the detection of nonsphericity. Appl. Opt. 35, 2259–2266 (1996).

3. Frohn, A., Norbert, R.: Dynamics of Droplets. Springer International Publishing (2000).

4. Ono, H., Kawatsuki, N.: Effects of saponification rate on electrooptical properties and morphology of poly (Vinyl alcohol)/liquid crystal composite films. Jpn. J. Appl. Phys. 34, 1601–1605 (1995).

5. Nazarenko, V.G., Sarala, S., Madhusudana, N. V.: Kinetics of Droplet Formation in UV-Cured Polymer-Dispersed Liquid Crystal Films. Jpn. J. Appl. Phys. 33, 2641 (1994).

6. Sumiyoshitani, S.: Effects of an applied electric field on collection efficiency by a charged droplet for dust particles in charged droplet scrubbers. Aerosol Sci. Technol. 20, 71–82 (1994).

7. Irissou, E., Legoux, J.G., Arsenault, B., Moreau, C.: Investigation of Al-Al 2O 3 cold spray coating formation and properties. J. Therm. Spray Technol. 16, 661–668 (2007).

8. Liang, G., Shen, S., Guo, Y., Zhang, J.: Boiling from liquid drops impact on a heated wall. Int. J. Heat Mass Transf. 100, 48–57 (2016).

9. Qiao, Y.M., Chandra, S.: Boiling of droplets on a hot surface in low gravity. Int. J. Heat

Mass Transf. 39, 1379–1393 (1996).

10.   Lin, L., Ponnappan, R.: Heat transfer characteristics of spray cooling in a closed loop. Int. J. Heat Mass Transf. 46, 3737–3746 (2003).

11.   Sirignano, W.A.: Fuel droplet vaporization and spray combustion theory. Prog. Energy Combust. Sci. 9, 291–322 (1983).

12.   Ohadi, M.M., Buckley, S.G.: High temperature heat exchangers and microscale combustion systems: Applications to thermal system miniaturization. Exp. Therm. Fluid Sci. 25, 207–217 (2001).

13.   Chigier, N.A.: The atomization and burning of liquid fuel sprays. Prog. Energy Combust. Sci. 2, 97–114 (1976).

14.   Kokjohn, S.L., Hanson, R.M., Splitter, D.A., Reitz, R.D.: Fuel reactivity controlled compression ignition (RCCI): A pathway to controlled high-efficiency clean combustion. Int. J. Engine Res. 12, 209–226 (2011).

15.   Yule, A.J., Bolado, R.: Fuel spray burning regime and initial conditions. Combust. Flame. 55, 1–12 (1984).

16.   Hou, Y., Liu, X., Liu, J., Li, M., Pu, L.: Experimental study on phase change spray cooling. Exp. Therm. Fluid Sci. 46, 84–88 (2013).

17.   Takenaka, N., Kadowaki, T., Kawabata, Y., Lim, I.C., Sim, C.M.: Visualization of cavitation phenomena in a Diesel engine fuel injection nozzle by neutron radiography. Nucl. Instruments Methods Phys. Res. Sect. A Accel. Spectrometers, Detect. Assoc. Equip. 542, 129–133 (2005).

18.   Chang, T.M.S.: Semipermeable Microcapsules. Science (80-.). 146, 524 LP-525 (1964).

19.   Swi Chang, T.M.: Artificial Cells. In: Biomaterials Science. pp. 811–827. Elsevier (2013).

20.   Prakash, S., Chang, T.M.S.: Microencapsulated genetically engineered live E. coli DH5
        cells administered orally to maintain normal plasma urea level in uremic rats. Nat. Med. 2,
        883 (1996).

21.   Huebner, A., Sharma, S., Srisa-Art, M., Hollfelder, F., Edel, J.B., deMello, A.J.:
        Microdroplets: A sea of applications? Lab Chip. 8, 1244 (2008).

22.   Jivani, R.R., Lakhtaria, G.J., Patadiya, D.D., Patel, L.D., Jivani, N.P., Jhala, B.P.:
        Biomedical microelectromechanical systems (BioMEMS): Revolution in drug delivery
        and analytical techniques. Saudi Pharm. J. 24, 1–20 (2016).

23.   Tüdős, A.J., Besselink, G.A.J., Schasfoort, R.B.M.: Trends in miniaturized total analysis
        systems for point-of-care testing in clinical chemistry. Lab Chip. 1, 83–95 (2001).

24.   Lindström, S., Andersson-Svahn, H.: Miniaturization of biological assays - Overview on
        microwell devices for single-cell analyses. Biochim. Biophys. Acta - Gen. Subj. 1810,
        308–316 (2011).

25.   Sant, S., Tao, S.L., Fisher, O.Z., Xu, Q., Peppas, N.A., Khademhosseini, A.:
        Microfabrication technologies for oral drug delivery. Adv. Drug Deliv. Rev. 64, 496–507
        (2012).

26.   Brandish, P.E., Chiu, C.S., Schneeweis, J., Brandon, N.J., Leech, C.L., Kornienko, O.,
        Scolnick, E.M., Strulovici, B., Zheng, W.: A cell-based ultra-high-throughput screening
        assay for identifying inhibitors of D-amino acid oxidase. J. Biomol. Screen. 11, 481–487

(2006).

27. Ward, K.B., Perozzo, M.A., Zuk, W.M.: Automatic preparation of protein crystals using laboratory robotics and automated visual inspection. J. Cryst. Growth. 90, 325–339 (1988).

28. Stevens, R.C.: High-throughput protein crystallization. Curr. Opin. Struct. Biol. 10, 558–563 (2000).

29. Whitesides, G.M.: The origins and the future of microfluidics. Nature. 442, 368–373 (2006).

30. Fontana, F., Ferreira, M.P.A., Correia, A., Hirvonen, J., Santos, H.A.: Microfluidics as a cutting-edge technique for drug delivery applications. J. Drug Deliv. Sci. Technol. 34, 76–87 (2016).

31. Herranz-Blanco, B., Arriaga, L.R., Mäkilä, E., Correia, A., Shrestha, N., Mirza, S., Weitz, D.A., Salonen, J., Hirvonen, J., Santos, H.A.: Microfluidic assembly of multistage porous silicon–lipid vesicles for controlled drug release. Lab Chip. 14, 1083–1086 (2014).

32. Prileszky, T.A., Furst, E.M.: Crystallization Kinetics of Partially Crystalline Emulsion Droplets in a Microfluidic Device. Langmuir. 32, 5141–5146 (2016).

33. Sun, Y., Zhou, X., Yu, Y.: A novel picoliter droplet array for parallel real-time polymerase chain reaction based on double-inkjet printing. Lab Chip. 14, 3603 (2014).

34. Zhu, Y., Zhu, L.N., Guo, R., Cui, H.J., Ye, S., Fang, Q.: Nanoliter-scale protein crystallization and screening with a microfluidic droplet robot. Sci. Rep. 4, 1–9 (2014).

35. Lazarus, L.L., Riche, C.T., Marin, B.C., Gupta, M., Malmstadt, N., Brutchey, R.L.: Two-

109

phase microfluidic droplet flows of ionic liquids for the synthesis of gold and silver nanoparticles. ACS Appl. Mater. Interfaces. 4, 3077–3083 (2012).

36.   Zhang, L., Niu, G., Lu, N., Wang, J., Tong, L., Wang, L., Kim, M.J., Xia, Y.: Continuous and scalable production of well-controlled noble-metal nanocrystals in milliliter-sized droplet reactors. Nano Lett. 14, 6626–6631 (2014).

37.   Keays, M.C., O'Brien, M., Hussain, A., Kiely, P.A., Dalton, T.: Rapid Identification of Antibiotic Resistance Using Droplet Microfluidics. Bioengineered. 7, 79–87 (2016).

38.   Jakiela, S., Kaminski, T.S., Cybulski, O., Weibel, D.B., Garstecki, P.: Bacterial growth and adaptation in microdroplet chemostats. Angew. Chemie - Int. Ed. 52, 8908–8911 (2013).

39.   Boedicker, J.Q., Vincent, M.E., Ismagilov, R.F.: Microfluidic confinement of single cells of bacteria in small volumes initiates high-density behavior of quorum sensing and growth and reveals its variability. Angew. Chemie - Int. Ed. 48, 5908–5911 (2009).

40.   Chen, Q., Utech, S., Chen, D., Prodanovic, R.M., Lin, J.-M., Weitz, D.A.: Controlled Assembly of Heterotypic cells in a Core-Shell Scaffold: Organ in a Droplet. Lab Chip. 16, 1346–1349 (2016).

41.   Wang, B.L., Ghaderi, A., Zhou, H., Agresti, J., Weitz, D.A., Fink, G.R., Stephanopoulos, G.: Microfluidic high-throughput culturing of single cells for selection based on extracellular metabolite production or consumption. Nat Biotech. 32, 473–478 (2014).

42.   Shi, W., Wen, H., Lu, Y., Shi, Y., Lin, B., Qin, J.: Droplet microfluidics for characterizing the neurotoxin-induced responses in individual Caenorhabditis elegans. Lab Chip. 10,

2855 (2010).

43.   Aubry, G., Zhan, M., Lu, H.: Hydrogel-droplet microfluidic platform for high-resolution imaging and sorting of early larval Caenorhabditis elegans. Lab Chip. 15, 1424–1431 (2015).

44.   Ozen, O., Aubry, N., Papageorgiou, D.T., Petropoulos, P.G.: Monodisperse drop formation in square microchannels. Phys. Rev. Lett. 96, 1–4 (2006).

45.   Feng, L., Kawahara, T., Yamanishi, Y., Hagiwara, M., Kosuge, K., Arai, F.: On-demand and size-controlled production of droplets by magnetically driven microtool. J. Robot. Mechatronics. 24, 133–140 (2012).

46.   Zhu, P., Tang, X., Wang, L.: Droplet generation in co-flow microfluidic channels with vibration. Microfluid. Nanofluidics. 20, 1–10 (2016).

47.   Schmid, L., Franke, T.: SAW-controlled drop size for flow focusing. Lab Chip. 13, 1691 (2013).

48.   Maeda, K., Onoe, H., Takinoue, M., Takeuchi, S.: Controlled synthesis of 3D multi-compartmental particles with centrifuge-based microdroplet formation from a multi-barrelled capillary. Adv. Mater. 24, 1340–1346 (2012).

49.   Mark, D., Haeberle, S., Zengerle, R., Ducree, J., Vladisavljević, G.T.: Manufacture of chitosan microbeads using centrifugally driven flow of gel-forming solutions through a polymeric micronozzle. J. Colloid Interface Sci. 336, 634–641 (2009).

50.   Park, S.-Y., Wu, T.-H., Chen, Y., Teitell, M.A., Chiou, P.-Y.: High-speed droplet generation on demand driven by pulse laser-induced cavitation. Lab Chip. 11, 1010

(2011).

51. Murshed, S.M.S., Tan, S.H., Nguyen, N.T., Wong, T.N., Yobas, L.: Microdroplet formation of water and nanofluids in heat-induced microfluidic T-junction. Microfluid. Nanofluidics. 6, 253–259 (2009).

52. Ziemecka, I., van Steijn, V., Koper, G.J.M., Rosso, M., Brizard, A.M., van Esch, J.H., Kreutzer, M.T.: Monodisperse hydrogel microspheres by forced droplet formation in aqueous two-phase systems. Lab Chip. 11, 620–624 (2011).

53. Zhu, P., Wang, L.: Passive and active droplet generation with microfluidics: a review. Lab Chip. 17, 34–75 (2017).

54. Zhu, P., Wang, L.: Passive and active droplet generation with microfluidics: a review. Lab Chip. 17, 34–75 (2017).

55. Chong, Z.Z., Tan, S.H., Gañán-Calvo, A.M., Tor, S.B., Loh, N.H., Nguyen, N.-T.: Active droplet generation in microfluidics. Lab Chip. 16, 35–58 (2016).

56. Li, Y., Jain, M., Ma, Y., Nandakumar, K.: Control of the breakup process of viscous droplets by an external electric field inside a microfluidic device. Soft Matter. 11, 3884–3899 (2015).

57. Link, D.R., Grasland-Mongrain, E., Duri, A., Sarrazin, F., Cheng, Z., Cristobal, G., Marquez, M., Weitz, D.A.: Electric control of droplets in microfluidic devices. Angew. Chemie - Int. Ed. 45, 2556–2560 (2006).

58. Yeh, C.H., Lee, M.H., Lin, Y.C.: Using an electro-spraying microfluidic chip to produce uniform emulsions under a direct-current electric field. Microfluid. Nanofluidics. 12, 475–

484 (2012).

59.   He, P., Kim, H., Luo, D., Marquez, M., Cheng, Z.: Low-frequency ac electro-flow-focusing microfluidic emulsification. Appl. Phys. Lett. 96, (2010).

60.   Tan, S.H., Semin, B., Baret, J.-C.: Microfluidic flow-focusing in ac electric fields. Lab Chip. 14, 1099 (2014).

61.   Zhang, M., Wu, J., Niu, X., Wen, W., Sheng, P.: Manipulations of microfluidic droplets using electrorheological carrier fluid. Phys. Rev. E - Stat. Nonlinear, Soft Matter Phys. 78, 1–5 (2008).

62.   Gu, H., Murade, C.U., Duits, M.H.G., Mugele, F.: A microfluidic platform for on-demand formation and merging of microdroplets using electric control. Biomicrofluidics. 5, (2011).

63.   Yan, Q., Xuan, S., Ruan, X., Wu, J., Gong, X.: Magnetically controllable generation of ferrofluid droplets. Microfluid. Nanofluidics. 19, 1377–1384 (2015).

64.   Wu, Y., Fu, T., Ma, Y., Li, H.Z.: Ferrofluid droplet formation and breakup dynamics in a microfluidic flow-focusing device. Soft Matter. 9, 9792 (2013).

65.   Tan, S.H., Nguyen, N.T.: Generation and manipulation of monodispersed ferrofluid emulsions: The effect of a uniform magnetic field in flow-focusing and T-junction configurations. Phys. Rev. E - Stat. Nonlinear, Soft Matter Phys. 84, 1–7 (2011).

66.   Tan, S.H., Nguyen, N.T., Yobas, L., Kang, T.G.: Formation and manipulation of ferrofluid droplets at a microfluidic T-junction. J. Micromechanics Microengineering. 20, (2010).

67.   Kahkeshani, S., Di Carlo, D., Macosko, E.Z., Srinivasan, V., Pamula, V.K., Fair, R.B.,

Guo, M.T., Rotem, A., Heyman, J.A., Weitz, D.A., Teh, S.Y., Lin, R., Hung, L.H., Lee, A.P., Barbulovic-Nad, I., Yang, H., Park, P.S., Wheeler, A.R., Fix, S.M., Borden, M.A., Dayton, P.A., Griffin, D.R., Weaver, W.M., Scumpia, P.O., Carlo, D. Di, Segura, T., Edd, J.F., Kahkeshani, S., Haddadi, H., Carlo, D. Di, Anna, S.L., Bontoux, N., Stone, H.A., Utada, A.S., Thorsen, T., Roberts, R.W., Arnold, F.H., Quake, S.R., Garstecki, P., Fuerstman, M.J., Stone, H.A., Whitesides, G.M., Steijn, V. Van, Kleijn, C.R., Kreutzer, M.T., Sugiura, S., Nakajima, M., Seki, M., Li, Z., Leshansky, A.M., Pismen, L.M., Tabeling, P., Hein, M., Fleury, J.B., Seemann, R., Mittal, N., Cohen, C., Bibette, J., Bremond, N., Dangla, R., Kayi, S.C., Baroud, C.N., Schuler, F., Schwemmer, F., Trotter, M., Wadle, S., Zengerle, R., Stetten, F. von, Paust, N., Schuler, F., Pamme, N., Liu, J., Tan, S.H., YAP, Y.F., Ng, M.Y., Nguyen, N.T., Chong, Z.Z., Tan, S.H., Gañán-Calvo, A.M., Tor, S.B., Loh, N.H., Nguyen, N.T., Wu, Y., Fu, T., Ma, Y., Li, H. \nZ., Liu, J., Yap, Y.F., Nguyen, N.T., Tan, S.H., Nguyen, N.T., Yobas, L., Kang, T.G., Duffy, D.C., McDonald, J.C., Schueller, O.J., Whitesides, G.M., Inglis, D.W., Riehn, R., Sturm, J.C., Austin, R.H., Stone, H.A., Leal, L.G., Hattori, K., Sugiura, S., Kanamori, T., Jovanovic, J., Bretherton, F.P., Dababneh, M.S., Ayoub, N.Y., Odeh, I., Laham, N.M., Baker, M., Baroud, C.N., Gallaire, F., Dangla, R., Katsikis, G., Cybulski, J.S., Prakash, M.: Drop formation using ferrofluids driven magnetically in a step emulsification device. Lab Chip. 16, 2474–2480 (2016).

68.   Kar, S., Joshi, S., Chaudhary, K., Maiti, T.K., Chakraborty, S.: Generation of droplets to serpentine threads on a rotating compact-disk platform. Appl. Phys. Lett. 107, (2015).

69.   Baroud, C.N., Robert de Saint Vincent, M., Delville, J.-P.: An optical toolbox for total control of droplet microfluidics. Lab Chip. 7, 1029 (2007).

70.   Cordero, M.L., Gallaire, F., Baroud, C.N.: Quantitative analysis of the dripping and jetting regimes in co-flowing capillary jets. Phys. Fluids. 23, 94111 (2011).

71.   Diguet, A., Li, H., Queyriaux, N., Chen, Y., Baigl, D.: Photoreversible fragmentation of a liquid interface for micro-droplet generation by light actuation. Lab Chip. 11, 2666 (2011).

72.   Yeh, C.H., Chen, K.R., Lin, Y.C.: Developing heatable microfluidic chip to generate gelatin emulsions and microcapsules. Microfluid. Nanofluidics. 15, 775–784 (2013).

73.   Miralles, V., Huerre, A., Williams, H., Fournié, B., Jullien, M.-C.: A versatile technology for droplet-based microfluidics: thermomechanical actuation. Lab Chip. 15, 2133–2139 (2015).

74.   Sauret, A., Spandagos, C., Shum, H.C.: Fluctuation-induced dynamics of multiphase liquid jets with ultra-low interfacial tension. Lab Chip. 12, 3380 (2012).

75.   Li, J., Mittal, N., Mak, S.Y., Song, Y., Shum, H.C.: Perturbation-induced droplets for manipulating droplet structure and configuration in microfluidics. J. Micromechanics Microengineering. 25, (2015).

76.   Yu, M., Hou, Y., Zhou, H., Yao, S.: An on-demand nanofluidic concentrator. Lab Chip. 15, 1524–32 (2015).

77.   Shemesh, J., Nir, A., Bransky, A., Levenberg, S.: Coalescence-assisted generation of single nanoliter droplets with predefined composition. Lab Chip. 11, 3225 (2011).

78.   Schmid, L., Franke, T.: Acoustic modulation of droplet size in a T-junction. Appl. Phys. Lett. 104, (2014).

115

79. Cheung, Y.N., Qiu, H.: Droplet pinch-off in acoustically actuated flow-focusing devices. J. Micromechanics Microengineering. 22, (2012).

80. Umbanhowar, P.B., Prasad, V., Weitz, D.A.: Monodisperse emulsion generation via drop break off in a coflowing stream. Langmuir. 16, 347–351 (2000).

81. Marín, A.G., Campo-Cortés, F., Gordillo, J.M.: Generation of micron-sized drops and bubbles through viscous coflows. Colloids Surfaces A Physicochem. Eng. Asp. 344, 2–7 (2009).

82. Anna, S.L., Bontoux, N., Stone, H. a.: Formation of dispersions using "flow focusing" in microchannels. Appl. Phys. Lett. 82, 364–366 (2003).

83. Takeuchi, S., Garstecki, P., Weibel, D.B., Whitesides, G.M.: An axisymmetric flow-focusing microfluidic device. Adv. Mater. 17, 1067–1072 (2005).

84. Yobas, L., Martens, S., Ong, W.-L., Ranganathan, N.: High-performance flow-focusing geometry for spontaneous generation of monodispersed droplets. Lab Chip. 6, 1073–1079 (2006).

85. Thorsen, T., Roberts, R.W., Arnold, F.H., Quake, S.R.: Dynamic pattern formation in a vesicle-generating microfluidic device. Phys. Rev. Lett. 86, 4163–4166 (2001).

86. Xu, J.H., Luo, G.S., Li, S.W., Chen, G.G.: Shear force induced monodisperse droplet formation in a microfluidic device by controlling wetting properties. Lab Chip. 6, 131–136 (2006).

87. Malloggi, F., Pannacci, N., Attia, R., Monti, F., Mary, P., Willaime, H., Tabeling, P., Cabane, B., Poncet, P.: Monodisperse colloids synthesized with nanofluidic technology.

116

Langmuir. 26, 2369–2373 (2010).

88. Dragosavac, M.M., Vladisavljević, G.T., Holdich, R.G., Stillwell, M.T.: Production of porous silica microparticles by membrane emulsification. Langmuir. 28, 134–143 (2012).

89. Vladisavljević, G.T., Kobayashi, I., Nakajima, M.: Production of uniform droplets using membrane, microchannel and microfluidic emulsification devices. Microfluid. Nanofluidics. 13, 151–178 (2012).

90. Utada, A.S., Fernandez-Nieves, A., Stone, H.A., Weitz, D.A.: Dripping to jetting transitions in coflowing liquid streams. Phys. Rev. Lett. 99, 1–4 (2007).

91. Gordillo, J.M., Sevilla, A., Campo-Cortés, F.: Global stability of stretched jets: conditions for the generation of monodisperse micro-emulsions using coflows. J. Fluid Mech. 738, 335–357 (2014).

92. Castro-Hernández, E., Gundabala, V., Fernández-Nieves, A., Gordillo, J.M.: Scaling the drop size in coflow experiments. New J. Phys. 11, (2009).

93. Anna, S.L., Bontoux, N., Stone, H.A.: Formation of dispersions using "flow focusing" in microchannels. Appl. Phys. Lett. 82, 364–366 (2003).

94. Xia, Y., Whitesides, G.M.: SOFT LITHOGRAPHY. Annu. Rev. Mater. Sci. 28, 153–184 (1998).

95. Anna, S.L.: Droplets and Bubbles in Microfluidic Devices. Annu. Rev. Fluid Mech. 48, 285–309 (2016).

96. Xu, J.H., Li, S.W., Tan, J., Wang, Y.J., Luo, G.S.: Preparation of Highly Monodisperse Droplet in a T-Junction Microfluidic Device. AIChE J. 52, 3005–3010 (2006).

97.   Mazutis, L., Araghi, A.F., Miller, O.J., Baret, J., Frenz, L., Janoshazi, A., Miller, B.J., Hutchison, J.B., Link, D., Griffiths, A.D., Ryckelynck, M.: Droplet-Based Microfluidic Systems for High-Throughput Single DNA Molecule Isothermal Amplification and Analysis. 81, 4813–4821 (2009).

98.   Wang, F., Burns, M.A.: Performance of nanoliter-sized droplet-based microfluidic PCR. Biomed. Microdevices. 11, 1071–1080 (2009).

99.   Lorenz, R.M., Fiorini, G.S., Jeffries, G.D.M., Lim, D.S.W., He, M., Chiu, D.T.: Simultaneous generation of multiple aqueous droplets in a microfluidic device. Anal. Chim. Acta. 630, 124–130 (2008).

100.   Wang, J.T., Wang, J., Han, J.J.: Fabrication of advanced particles and particle-based materials assisted by droplet-based microfluidics. Small. 7, 1728–1754 (2011).

101.   Sun, C., Zhao, X.W., Zhao, Y.J., Zhu, R., Gu, Z.Z.: Fabrication of colloidal crystal beads by a drop-breaking technique and their application as bioassays. Small. 4, 592–596 (2008).

102.   Vyawahare, S., Griffiths, A.D., Merten, C.A.: Miniaturization and parallelization of biological and chemical assays in microfluidic devices. Chem. Biol. 17, 1052–1065 (2010).

103.   Vladisavljević, G.T., Khalid, N., Neves, M.A., Kuroiwa, T., Nakajima, M., Uemura, K., Ichikawa, S., Kobayashi, I.: Industrial lab-on-a-chip: Design, applications and scale-up for drug discovery and delivery. Adv. Drug Deliv. Rev. 65, 1626–1663 (2013).

104.   Li, W., Young, E.W.K., Seo, M., Nie, Z., Garstecki, P., Simmons, C.A., Kumacheva, E.:

Simultaneous generation of droplets with different dimensions in parallel integrated microfluidic droplet generators. Soft Matter. 4, 258–262 (2008).

105. Li, W., Young, E.W.K., Seo, M., Nie, Z., Garstecki, P., Simmons, C. a., Kumacheva, E.: Simultaneous generation of droplets with different dimensions in parallel integrated microfluidic droplet generators. Soft Matter. 4, 258 (2008).

106. Hashimoto, M., Shevkoplyas, S.S., Zasońska, B., Szymborski, T., Garstecki, P., Whitesides, G.M.: Formation of bubbles and droplets in parallel, coupled flow-focusing geometries. Small. 4, 1795–1805 (2008).

107. Zhou, P., Tarlet, D., Wei, M., Fan, Y., Luo, L.: Novel multi-scale parallel mini-channel contactor for monodisperse water-in-oil emulsification. Chem. Eng. Res. Des. 121, 233–244 (2017).

108. Baroud, C.N., Gallaire, F., Dangla, R.: Dynamics of microfluidic droplets. Lab Chip. 10, 2032 (2010).

109. Christopher, G.F., Anna, S.L.: Microfluidic methods for generating continuous droplet streams. J. Phys. D. Appl. Phys. 40, R319–R336 (2007).

110. Eggers, J., Villermaux, E.: Physics of liquid jets. Reports Prog. Phys. 71, 36601 (2008).

111. Garstecki, P., Stone, H.A., Whitesides, G.M.: Mechanism for flow-rate controlled breakup in confined geometries: A route to monodisperse emulsions. Phys. Rev. Lett. 94, 1–4 (2005).

112. Chen, A.U., Notz, P.K., Basaran, O. a: Computational and experimental analysis of pinch-off and scaling. Phys. Rev. Lett. 88, 174501 (2002).

113. Huerre, P., Monkewitz, P.A.: Local and Global Instabilities in Spatially Developing Flows. Annu. Rev. Fluid Mech. 22, 473–537 (1990).

114. Utada, A.S., Fernandez-Nieves, A., Gordillo, J.M., Weitz, D.A.: Absolute instability of a liquid jet in a coflowing stream. Phys. Rev. Lett. 100, 1–4 (2008).

115. Joseph Plateau-Statique experimentale et theorique des liquides soumis aux seules forces moleculaires ~ French and English versions.

116. Rayleigh, Lord: On The Instability Of Jets. Proc. London Math. Soc. s1-10, 4–13 (1878).

117. Rayleigh, L.: On the Capillary Phenomena of Jets. Proc. R. Soc. London. 29, 71–97 (1879).

118. Tomotika, S.: On the Instability of a Cylindrical Thread of a Viscous Liquid Surrounded by Another Viscous Fluid. Proc. R. Soc. Lond. A. Math. Phys. Sci. 150, 322–337 (1935).

119. Kitamura, Y.: Stability Systems. 60, (1982).

120. Meister, B.J., Scheele, G.F.: Drop formation from cylindrical jets in immiscible liquid systems. AIChE J. 15, 700–706 (1969).

121. Meister, B.J., Scheele, G.F.: Prediction of jet length in immiscible liquid systems. AIChE J. 15, 689–699 (1969).

122. Hilbing, J.H., Heister, S.D.: Droplet size control in liquid jet breakup. Phys. Fluids. 8, 1574 (1996).

123. Homma, S., Koga, J., Matsumoto, S., Song, M., Tryggvason, G.: Breakup mode of an axisymmetric liquid jet injected into another immiscible liquid. Chem. Eng. Sci. 61, 3986–3996 (2006).

124. Shinjo, J., Umemura, A.: Simulation of liquid jet primary breakup: Dynamics of ligament and droplet formation. Int. J. Multiph. Flow. 36, 513–532 (2010).

125. Eggers, J., Villermaux, E.: Physics of liquid jets. Reports Prog. Phys. 71, 36601 (2008).

126. Garstecki, P., Fuerstman, M.J., Whitesides, G.M.: Nonlinear dynamics of a flow-focusing bubble generator: An inverted dripping faucet. Phys. Rev. Lett. 94, 38–41 (2005).

127. Zhu, P., Kong, T., Kang, Z., Tian, X., Wang, L.: Tip-multi-breaking in capillary microfluidic devices. Sci. Rep. 5, 1–8 (2015).

128. Shui, L., Mugele, F., van den Berg, A., Eijkel, J.C.T.: Geometry-controlled droplet generation in head-on microfluidic devices. Appl. Phys. Lett. 93, 153113 (2008).

129. Stone, H. a: DYNAMICS OF DROP DEFORMATION AND BREAKUP IN VISCOUS FLUIDS. Annu. Rev. Fluid Mech. 26, 65–102 (1994).

130. Tseng, Y.H., Prosperetti, A.: Local interfacial stability near a zero vorticity point. J. Fluid Mech. 776, 5–36 (2015).

131. Martz, T.D., Bardin, D., Sheeran, P.S., Lee, A.P., Dayton, P.A.: Microfluidic generation of acoustically active nanodroplets. Small. 8, 1876–1879 (2012).

132. Jeong, W.-C., Lim, J.-M., Choi, J.-H., Kim, J.-H., Lee, Y.-J., Kim, S.-H., Lee, G., Kim, J.-D., Yi, G.-R., Yang, S.-M.: Controlled generation of submicron emulsion droplets via highly stable tip-streaming mode in microfluidic devices. Lab Chip. 12, 1446 (2012).

133. Zhu, P., Kong, T., Lei, L., Tian, X., Kang, Z., Wang, L.: Droplet Breakup in Expansion-contraction Microchannels. Sci. Rep. 6, 1–11 (2016).

134. Segur, J.: Physical properties of glycerine and its solutions. Aciscience.Org. 1–27 (1953).

135. Gaonkar, A.G.: Interracial Tensions of Vegetable Oil / Water Systems : Effect of Oil Purification. J. Am. Oil Chem. Soc. 66, 1090–1092 (1989).

136. Fowkes, F.M.: Attractive Forces At Interfaces. Ind. Eng. Chem. 56, 40–52 (1964).

137. Fasina, O.O., Colley, Z.: Viscosity and Specific Heat of Vegetable Oils as a Function of Temperature: 35°C to 180°C. Int. J. Food Prop. 11, 738–746 (2008).

138. Esteban, B., Riba, J.-R., Baquero, G., Puig, R., Rius, A.: Characterization of the surface tension of vegetable oils to be used as fuel in diesel engines. Fuel. 102, 231–238 (2012).

139. Khattab, I.S., Bandarkar, F., Amin, M., Fakhree, A., Jouyban, A.: Density , viscosity , and surface tension of water + ethanol mixtures from 293 to 323 K. 29, 812–817 (2012).

140. Ate, E., Mann, J.A., Tavana, H.: Ultralow Interfacial Tensions of Aqueous Two-Phase Systems Measured Using Drop Shape. (2014).

141. Schneider, C. a, Rasband, W.S., Eliceiri, K.W.: NIH Image to ImageJ: 25 years of image analysis. Nat. Methods. 9, 671–675 (2012).

142. Zhao, Q., Xu, M., Fränti, P.: Knee point detection on bayesian information criterion. Proc. - Int. Conf. Tools with Artif. Intell. ICTAI. 2, 431–438 (2008).

143. Omocea, I.L., Patrascu, C., Turcanu, M., Balan, C.: Breakup of Liquid Jets. Energy Procedia. 85, 383–389 (2016).

144. Esquena, J.: Water-in-water (W/W) emulsions. Curr. Opin. Colloid Interface Sci. 25, 109–119 (2016).

145. Sivars, U., Tjerneld, F.: Mechanisms of phase behaviour and protein partitioning in detergent / polymer aqueous two-phase systems for puri ¢ cation of integral membrane

proteins 1. 1474, 133–146 (2000).

146. Merchuk, J.C., Andrews, B.A., Asenjo, J.A.: Aqueous two-phase systems for protein separation Studies on phase inversion. 711, 285–293 (1998).

147. Kumar, A., Kamihira, M., Galaev, I.Y., Mattiasson, B., Iijima, S.: Type-Speci ® c Separation of Animal Cells in Aqueous Two-Phase Systems Using Antibody Conjugates with Temperature-Sensitive Polymers. (2001).

148. Frampton, J.P., Lai, D., Sriram, H.: Precisely targeted delivery of cells and biomolecules within microchannels using aqueous two-phase systems. 1043–1051 (2011).

149. Tavana, H., Jovic, A., Mosadegh, B., Lee, Q.Y., Liu, X., Luker, K.E., Luker, G.D., Weiss, S.J., Takayama, S.: Nanolitre liquid patterning in aqueous environments for spatially defined reagent delivery to mammalian cells. Nat. Mater. 8, 736–741 (2009).

150. Yaguchi, T., Lee, S., Choi, S., Kim, D., Kim, T., Mitchell, J.: Micropatterning bacterial suspensions using aqueous two phase systems †. 2848–2852 (2010).

151. Kepka, C., Rhodin, J., Lemmens, R., Tjerneld, F., Gustavsson, P.: Extraction of plasmid DNA from Escherichia coli cell lysate in a thermoseparating aqueous two-phase system ʚ. 1024, 95–104 (2004).

152. Azevedo, A.M., Rosa, P.A.J., Ferreira, I.F., Pisco, A.M.M.O., Vries, J. De, Korporaal, R., Visser, T.J., Aires-barros, M.R.: Affinity-enhanced purification of human antibodies by aqueous two-phase extraction. 65, 31–39 (2009).

153. R. M. Cormack: A Review of Classification. J. R. Stat. Soc. Ser. A. 134, 321–367 (1971).

154. Mehmed Kantardzic: Data mining Concepts, Models, Methods, and Algorithms. (2011).

155. Tan, P.-N., Steinbach, M., Kumar, V.: Chap 8 : Cluster Analysis: Basic Concepts and Algorithms. Introd. to Data Min. Chapter 8 (2005).

156. Kaufman, L., Rousseeuw, P.J.: Finding Groups in Data: An Introduction to Cluster Analysis. (2005).

157. Macqueen, J.: Some methods for classification and analysis of multivariate observations. Proc. Fifth Berkeley Symp. Math. Stat. Probab. 1, 281–297 (1967).

158. Jain, A.K.: Data clustering: 50 years beyond K-means. Pattern Recognit. Lett. 31, 651–666 (2010).

159. Thorndike, R.L.: Who belongs in the family? Psychometrika. 18, 267–276 (1953).

160. Zagnoni, M., Anderson, J., Cooper, J.M.: Hysteresis in multiphase microfluidics at a T-junction. Langmuir. 26, 9416–9422 (2010).

161. Guillot, P., Colin, A., Ajdari, A.: Stability of a jet in confined pressure-driven biphasic flows at low Reynolds number in various geometries. Phys. Rev. E - Stat. Nonlinear, Soft Matter Phys. 78, 1–4 (2007).